DOWN-SHIFTING OF LIGHT BY ION IMPLANTED SAMPLES FOR PHOTOVOLTAIC APPLICATIONS

DOWN-SHIFTING OF LIGHT BY ION IMPLANTED SAMPLES FOR PHOTOVOLTAIC APPLICATIONS

by

RACHEL MARIE SAVIDGE

B.Sc.ME, University of New Brunswick 2009

A Thesis

Submitted to the School of Graduate Studies

in Partial Fulfilment of the Requirements

for the Degree

Master of Applied Science

McMaster University

© Copyright by Rachel Marie Savidge, September 2012

MASTER OF APPLIED SCIENCE (2012) McMASTER UNIVERSITY

(Department of Engineering Physics) Hamilton, Ontario

TITLE: Down-shifting of Light by Ion Implanted Samples for Photovoltaic Applications

AUTHOR: Rachel Marie Savidge, B.Sc.ME, University of New Brunswick

THESIS SUPERVISORS: Dr. Rafael N. Kleiman and Dr. Andrew P. Knights

NUMBER OF PAGES: xvii, 111

Abstract

Single junction silicon photovoltaic cells (SJSPVCs) are unable to transform all the energy in the solar spectrum into electricity, due to the broad nature of the solar spectrum and the limits imposed by a single bandgap. Furthermore, high surface recombination velocity reduces the SJSPVC external quantum efficiency response, particularly to ultraviolet photons. It is the goal of spectral engineering to optimize the light that is incident on the cell, by down-shifting high energy photons to lower energies, for example, to improve the performance of photovoltaic cells.

This thesis represents a study into the luminescence of ion implanted films, involving silicon nanocrystals (Si-NCs) and rare-earth ions in fused silica or silicon nitride. Quantum efficiency measurements taken with an integrating sphere were used to characterize some of the samples. Other photoluminescence (PL) characterization work was carried out with a single-wavelength laser and a collection lens normal to the sample. Variable angle spectroscopic ellipsometry (VASE) was used to estimate the optical constants of the implanted films. In secondary work, Rutherford backscattering spectrometry, time-dependent PL, infrared-PL measurements, and electrical conductivity measurements were used to characterize select samples.

It was found that the conversion efficiency of Si-NCs in fused silica was about 1% – too low to be useful according to modeled results. However, considerable variation in the peak wavelength of the Si-NC PL was obtained, depending on the peak concentration of implanted silicon. Si-NC-type PL was also produced by low-energy implantation of oxygen into a Czochralski silicon wafer.

Oxygen was also implanted into films of cerium-doped high-purity silicon nitride, and it was shown that the photoluminescence from these films is largely dependent on the level of oxygen doping. The internal conversion efficiency of a cerium-doped fused

silica sample was found to approach 20%, which indicates that this is a promising avenue for future research.

Finally, energy transfer was demonstrated between Si-NCs and erbium ions. The lifetime of the erbium PL appears to increase with increasing implanted silicon fluence.

Acknowledgements

I would like to thank my supervisors, Professor Rafael Kleiman and Professor Andrew Knights, for giving me the opportunity to work on this project, and for their guidance and enthusiasm throughout. I have learnt about photovoltaics and photonics, sample processing and characterization, equipment set-up and operation, safety awareness and safe operating procedures, setting up characterization units, working with the laboratory equipment, and most of all, I have gained an appreciation for scientific research and the challenges that are involved.

Especial thanks must be given to Doris Stevanovic who provided many training sessions, invited me to participate in the departmental health and safety committee, and spent many hours with me at the ion implanter. Thanks are also due to Professor Andrew Knights and Dave Chivers (Ion Beam Services Ltd.) for their expert assistance in operating the ion-implanter.

Sincere thanks are given to Jacek Wojcik for organizing and providing VASE training, and for offering counsel and support on many laboratory-related tasks, such as changing gas cylinders or general help around the lab. Thanks are also due to Doris Stevanovic for her prompt response whenever laboratory supplies were running short.

Zhilin Peng provided training on the dicing saw, and then continued to oversee my use of the equipment when political issues made it impossible for me to operate the dicing saw on my own. Particular thanks are due to him for this additional demand on his time. Thanks also to Zhilin Peng for providing training on the aluminum sputtering system.

Lyudmila Goncharova provided an excellent introduction to Rutherford backscattering at the University of Western Ontario, and assisted in the processing and analyzing of three critical samples. Thanks to her for that assistance.

Thanks to Dr. Iain Crowe and Professor Matthew Halsall at the University of Manchester for performing the IR measurements of the erbium-doped Si-NC samples. Thanks to Miraj Shah at the University College London for the time-resolved erbium lifetime measurements.

The NSERC CREATE program in Photovoltaics (administered by Professor John Preston and Janet Delsey) provided funding to visit the Canadian Light Source. Patrick Wilson and Zahra Khatami explained to me how the system operated, and although no synchrotron data is presented in this thesis, the experience was appreciated. Thanks are also due to Patrick Wilson for providing helpful discussions on silicon nanocrystals, rare-earths, and photoluminescence measurements.

Professor Rafael Kleiman and Jennifer Briand administered the NSERC Photovoltaic Innovation Network (PVIN), which provided constant support for photovoltaic outreach opportunities. Thanks to the NSERC PVIN for providing a significant portion of the funding for this project.

Particular thanks are due to Linda Wilson, who processed numerous payment claims for me, and also to Marilyn Marlow and all the Engineering Physics administrative staff for providing clear and swift answers to questions on bureaucratic processes.

To my collaborators at the University of Ottawa, who performed the theoretical modelling for this project, reinforcing the belief that sample creation was worthwhile: thank you for the hours spent in teleconference and e-mail communication. I appreciate the new perspective that you brought to the project and your vision for submitting an abstract to the Photovoltaic Specialists Conference held in Austin in June, 2012.

I am grateful for two other students in Engineering Physics who shared the experience of being Master's students with me: Justin Sacks and Erik Janssen. Your friendship and support, and your shared enthusiasm and belief in photovoltaics as the

energy source of the future, has resulted in many happy memories from these past two years.

Finally, thank you to my two supervisors and to Professor Peter Mascher, the third member of my defense committee, who all read my thesis thoroughly and made many insightful and helpful suggestions: any remaining omissions or mistakes are my own.

Rachel Savidge, September 2012

Table of Contents

Chapter 1 1

1.1 Spectral engineering motivation 1

1.1.1 Modeling 5

1.2 Motivation for photoluminescence quantum efficiency measurements 7

1.3 Assumptions 8

1.4 Thesis outline 8

Chapter 2 10

2.1 General rules for down-shifters 10

2.2 Introduction to photoluminescence 10

2.3 Silicon nanocrystals 11

2.4 Lanthanide rare-earths 15

2.5 Energy transfer from silicon nanocrystals to lanthanide rare-earths 17

2.6 Cerium as a down-shifter 19

2.7 Chapter summary 20

Chapter 3 21

3.1 Starting materials 21

3.2 Sample dicing 22

3.3 Sample cleaning 22

3.4 Ion implantation 23

3.4.1 Selecting an ion for implantation 26

3.4.2 Practical considerations 27

3.4.3 Implanted ions, energies, and fluences 27

3.5 Rapid thermal annealing 29

3.6 Implanting and annealing recipes for the fabrication of doped and undoped Si-NC and/or rare-earth-containing samples 30

3.7 Photoluminescence characterization 31

3.7.1 Calibration of the charge-coupled device 32

3.7.2 Quantum efficiency measurement 33

3.7.3 Step-by-step directions for a quantum efficiency measurement 36

3.7.4 Data smoothing 38

3.7.5 Representative data collected for quantum efficiency measurements 39

3.8 Ellipsometry 41

3.9 Chapter summary 43

Chapter 4 44

4.1 Silicon nanocrystals in fused silica 44

4.2 Silicon fluence-dependent Si-NC creation 47

4.3 Photoluminescence from oxygen-implantated silicon 49

4.3.1 Electrical contacting of oxygen-implanted samples 53

4.4 Quantum efficiency measurement for photoluminescence from silicon nanocrystals 54

4.5 Erbium-doped silicon nanocrystals in fused silica 55

4.6 Cerium-oxygen co-doped dielectric films 59

4.6.1 Rutherford backscattering 62

4.6.2 Electrical conduction of the cerium-doped silicon nitride 63

4.6.3 Cerium in fused silica 64

4.6.4 Quantum efficiency measurement of photoluminescence from cerium-doped fused silica 65

4.7 Chapter summary 69

Chapter 5 71

5.1 Summary of the thesis 71

5.2 Review of results and conclusions 72

5.3 Suggestions for future work 73

5.3.1 Material fabrication and characterization 73

5.3.2 Improvements to experimental design 77

5.4 Final remarks 78

Appendix A: Dicing Saw Standard Operating Procedure 79

Appendix B: SRIM simulations 83

Appendix C: Calibration of the rapid thermal annealer 88

Appendix D: Photoluminescence set-up standard operating procedure 91

Appendix E: Quantum efficiency error calculations 93

Works Cited 102

Table of Illustrations

Figure 1.1: Absorption coefficient of silicon. Adapted from [4]. 2

Figure 1.2: The external quantum efficiency for a representative SJSPVC peaks for photons with wavelength of approximately 700 nm (red). The solar spectrum (blue) is the Air-Mass 1.5 spectrum, which is the average solar irradiance received by the 48 contiguous U.S. states. Adapted from [6]. 3

Figure 1.3: Schematic of an optically-coupled down-converting material placed on the front surface of a photovoltaic cell. Taken from [9]. 4

Figure 1.4: Modeled luminescent down-shifting (LDS) efficiency required to maintain the SJSPVC performance. The QE of the SJSPVC used in the converter model is shown as a dashed line. Note that in regions where the cell efficiency is low, the LDS efficiency does not need to be high in order to meet the minimum efficiency requirement. [10].............................. 6

Figure 2.1: The photoluminescence from multilayered Si-rich SiO_2 and SiO_2 indicates that the peak photoluminescence location is related to Si-NC size [25]. 13

Figure 2.2: Absorption and PL emission from two ion implanted samples of Si-NCs in SiO_2 (adapted from [18]). Sample B was implanted with a higher fluence of silicon than sample A, resulting in red-shifted PL from sample B compared with the PL from sample A. Note that the absorption takes place predominantly below 400 nm. 15

Figure 2.3: Periodic table of the elements showing the lanthanide rare-earths highlighted in yellow. Adapted from [35]. 16

Figure 2.4: Energy transfer between Si-NC in SiO_2 and Er^{3+} ions. As the implanted erbium fluence increases, the PL from erbium (at 1.54 μm) also

increases, and the PL from the Si-NCs (at 0.8 μm) decreases. Taken from [44]. ... 18

Figure 3.1: Simple schematic of the ion implanter. Ions created in the plasma are accelerated toward an analyzing magnet, which limits the combination of mass and charge which reach the sample mounted in the target chamber. ... 24

Figure 3.2: Example of output from SRIM software, showing the implantation depth on the x-axis. ... 25

Figure 3.3: Typical RTA recipe for Si-NC formation after silicon or oxygen implantation. Nitrogen gas flowed through the RTA from the beginning of the recipe until the temperature dropped to 500 °C for 10 minutes; 5% H_2 : N_2 was flowing during the remainder of the run. ... 29

Figure 3.4: Typical RTA recipe for cerium-doped samples. T_{max} was typically 1000° C. ... 30

Figure 3.5: Comparison of PL obtained from two samples, measured with a calibrated (ABS, right vertical axis) and an uncalibrated CCD, and excited with a 405 nm laser line. There is some red-shifting of the peak wavelength, particularly at wavelengths that are close to the silicon bandgap of the detector. ... 32

Figure 3.6: Schematic of the integrating sphere quantum efficiency photoluminescence set-up. (Figure credit: Justin Sacks). ... 34

Figure 3.7: Photoluminescence shown as $\varphi_{emitted}$, and incident laser light shown as $\varphi_{incident}$. Taken from [59]. ... 35

Figure 3.8: Data manipulation of the Si-NC PL obtained from the integrating sphere. The response (in green) was first averaged (blue), and then corrected by hand (red) to resemble the PL curve obtained from the normal PL measurement set-up. ... 39

Figure 3.9: The 325 nm HeCd laser line measured through the sphere, with a piece of fused silica in the laser path, and then a piece of cerium-implanted fused

silica in the laser path. The subtraction of the latter from the former gives the absorption of cerium. 40

Figure 3.10: Comparison of the PL profile obtained from the sphere (blue) and corrected for the sphere response (green). Note that the magnitude of the response increases by three orders when the sphere response is taken into account. 40

Figure 3.11: Screen-shot of fused silica modelled as SiO_2 to obtain the modelling parameters for the fused silica. 42

Figure 3.12: Si-NC sample modelled as a transparent layer on SiO_2. The mean squared error (MSE) value is 2.606, which is considered low, indicating good agreement between the data and the model. 42

Figure 4.1: PL from two silicon-implanted Si-NC samples. The peak wavelength of the sample implanted with the higher-fluence ($3.04x10^{16}$ Si^+/cm^2) is red-shifted compared with the peak wavelength of the sample implanted with the higher silicon fluence. 44

Figure 4.2: Real (*n*) and imaginary (*k*) components of the refractive index from Si-NC samples plotted versus photon wavelength, measured using VASE. The sample with higher silicon content ($3.04x10^{16}$ Si/cm^2) has a higher real index of refraction, and a greater extinction coefficient (k) than the sample with lower silicon content ($2.10x10^{16}$ Si^+/cm^2). 45

Figure 4.3: SRIM output from Si^+ (15 keV) implantated into SiO_2 at 7 degrees, showing the resulting distribution of silicon ions and vacancies. 46

Figure 4.4: Light transmission through fused silica samples containing Si-NCs (implanted with $2.10x10^{16}$ Si^+/cm^2 and with $3.04x10^{16}$ Si^+/cm^2). The sample with the higher implanted silicon fluence yields less light transmission. 47

Figure 4.5: PL from a range of silicon fluences implanted into fused silica at 15 keV, annealed at approximately the same temperature, and excited with a 405

nm laser beam. Note the trend from no PL, to blue-shifted PL, to peak intensity PL, to red-shifted PL. ... 48
Figure 4.6: PL from oxygen-implanted into silicon (blue, primary axis), compared with typical silicon-implanted Si-NC PL in fused silica quartz (orange, secondary axis). Both samples were annealed at 1100 °C and both were excited by a 405 nm 16 mW laser. ... 50
Figure 4.7: Refractive indices for two oxygen-implanted silicon samples. The samples were modeled as a three-layer with a thin (10 Å) silicon top-layer, followed by a larger (513 Å), transparent region (Cauchy layer) which could contain Si-NCs or amorphous SiO_2 particles, and a silicon substrate. ... 51
Figure 4.8: PL from oxygen implantation (405 nm excitation). Note that the slightly oxygen-rich sample has slightly blue-shifted PL. ... 52
Figure 4.9. The electrical curve from Al-Al contacted O-implanted (5.50×10^{16} O_2^+/cm^2) silicon. It is clear that the device does pass current. ... 54
Figure 4.10: Erbium-implanted fused silica samples showed characteristic erbium PL, provided that Si-NCs were present in the sample. This indicated that energy transfer is occurring between the Si-NCs and the erbium ions. ... 56
Figure 4.11: PL (405 nm excitation) obtained from Si-NC samples before they were implanted with erbium. Note that the intensities of the PL from the Si-NC appear to have no correlation to the intensity of the erbium emission shown in Figure 4.10. ... 57
Figure 4.12: Transient PL measured for erbium-doped Si-NC samples. There appears to be a relationship between the implanted Si-fluence (i.e. Si-NC size) and the radiative lifetime of these ensembles. ... 58
Figure 4.13: Representative PL from a series of thin films of LPCVD Si_3N_4 that were implanted with cerium (5×10^{15} Ce^+/cm^2 at 25 keV) and oxygen (varying fluence). ... 59

Figure 4.14: Exponential-type dependence of cerium peak PL intensity with varying oxygen content. The line is provided as a guide for the eye. 60
Figure 4.15: Constant oxygen fluence of $2x10^{16}$ O_2^+/cm^2. The PL varies minimally with cerium fluence at this oxygen fluence. Note that more cerium yields more PL. 61
Figure 4.16: Constant oxygen fluence of $3.5x10^{16}$ O_2^+/cm^2. The PL varies significantly with cerium fluence at this oxygen fluence. Note that more cerium yields more PL. 61
Figure 4.17: Constant oxygen fluence of $5.0x10^{16}$ O_2^+/cm^2. The PL varies minimally once again with cerium fluence. Note that less cerium yields more PL, contrary to the results obtained with lower oxygen fluence. 62
Figure 4.18: Rutherford backscattering results from three samples containing $3x10^{15}$ Ce^+ implanted into LPCVD Si_3N_4. The variation in the peak magnitude is within experimental error, indicating that the implanted cerium was not sputtered out of the material during the subsequent oxygen implantation. 63
Figure 4.19: Conduction of electrical current through films that contain cerium and oxygen. 64
Figure 4.20: Comparison of the PL intensity from $3x10^{15}$ Ce^+/cm^2 implanted in Si_3N_4 with an optimal amount of oxygen also implanted, and cerium implanted in SiO_2. Note that the cerium-doped SiO_2 does not show strong PL, likely due to the high concentration of oxygen in SiO_2. 64
Figure 4.21: Number of photons in the PL from $3x10^{15}$ Ce^+/cm^2 (25 keV) in SiO_2. Measured using the integrating sphere set-up, and corrected for the integrating sphere response and the cyan filter. 66
Figure 4.22: Comparison of the PL shape obtained from the cerium-implanted $3x10^{15}$ Ce^+/cm^2 (25 keV) fused silica sample in the sphere set-up, and in the normal set-up. 67

Figure 4.23: Transmission response of cyan filter. 67
Figure 4.24: The AM1.5 G spectrum super-imposed on a plot showing the down-shifting performance of an organic dye, and the EQE of a CdTe cell. Note that the down-shifting of cerium-doped fused silica could have a similar application. Taken from [76]. 69

Figure B-1: Si^{+} (15 keV) implanted into SiO_2 at a seven-degree angle for creating Si-NCs. 83
Figure B-2: Er^{3+} (35 keV) implanted into SiO_2 at a seven-degree angle in addition to Si-NCs in fused silica. 84
Figure B-3: O^{+} (9.5 keV) == O_2^{+} (19 keV) implanted into silicon at a seven-degree angle. 84
Figure B-4: Ce^{+} (25 keV) implanted into Si_3N_4 at a seven-degree angle. 85
Figure B-5: O^{+} (9.5 keV) == O_2^{+} (19 keV) implanted into Si_3N_4 at a seven-degree angle. The implantation energy was chosen to match the peak of the cerium implantation shown in Appendix Figure B-4. 85
Figure B-6: Ce^{+} (32.5 keV) implanted into SiO_2 at a seven-degree angle. 86
Figure B-7: Ce^{+} (25 keV) implanted into SiO_2 at a seven-degree angle. 86
Figure B-8: O^{+} (9.5 keV) == O_2^{+} (19 keV) implanted into SiO_2 at a seven-degree angle. 87
Figure C-1: Calibration charts for thermal oxidation constants. Taken from [79]. 89

Listing of Tables

Table 3.1: Sample substrates, ion implanted, implantation energies, and fluences used in this thesis 28
Table 4.1: External and internal quantum efficiencies of the Si-NC samples [66]. 54

Table C.1: Rapid thermal annealer raw data for calibration…………………………... 88
Table C.2: Rapid thermal annealer calibration constants from charts………………… 89
Table C.3: Calculated rapid thermal annealer temperature based on the measured oxide thickness……………………………………………………… 90

Chapter 1
Introduction

1.1 Spectral engineering motivation

Photovoltaic (PV) technology is gaining a foothold in global electricity production, due to generous government-initiated incentives in numerous countries [1], and due to decreasing overall system installation costs due to falling wholesale prices for photovoltaic cells and components [2]. Despite advances in higher-efficiency cells, such as multijunction cells or even intricate single-junction cells, the market is dominated by the robust, and relatively simple, single-junction silicon photovoltaic cell (SJSPVC) technology [3]. However, single-junction photovoltaic (PV) devices do not efficiently extract all of the energy in the solar spectrum due to the fundamental properties of semiconductors, and the broad nature of the solar spectrum. Photons with less energy than the semiconductor bandgap are not absorbed by the device. In addition, many of the absorbed photons are utilized inefficiently, since the promoted electron-hole pairs lose energy to thermalization and/or surface recombination.

The solar spectrum is comprised of electromagnetic radiation that originates in the sun's core. The core is approximately 5700 degrees Celsius and the bulk of the resulting "black-body" radiation stretches from about 300 nm to 5000 nm, as seen from the earth. The black-body spectrum is attenuated at some wavelengths because the electromagnetic radiation interacts with the atmosphere surrounding the earth, but the solar spectrum remains broad, which presents a challenge for photovoltaic transformation.

A single-junction solar cell typically absorbs photons containing more energy than the bandgap of the material. The bandgap is the energy separation between the

valence and the conduction band, and it defines the minimum energy required to promote an electron from the valence band to the conduction band. Photons with less energy than the bandgap are essentially not absorbed by the cell, unless impurities generating mid-bandgap states are present in the cell material. The photons with energy greater than the bandgap energy are not uniformly absorbed. The absorption coefficient of intrinsic silicon, shown in Figure 1.1, indicates that higher-energy photons are absorbed closer to the surface of the cell, and lower energy photons are absorbed deeper in the cell material.

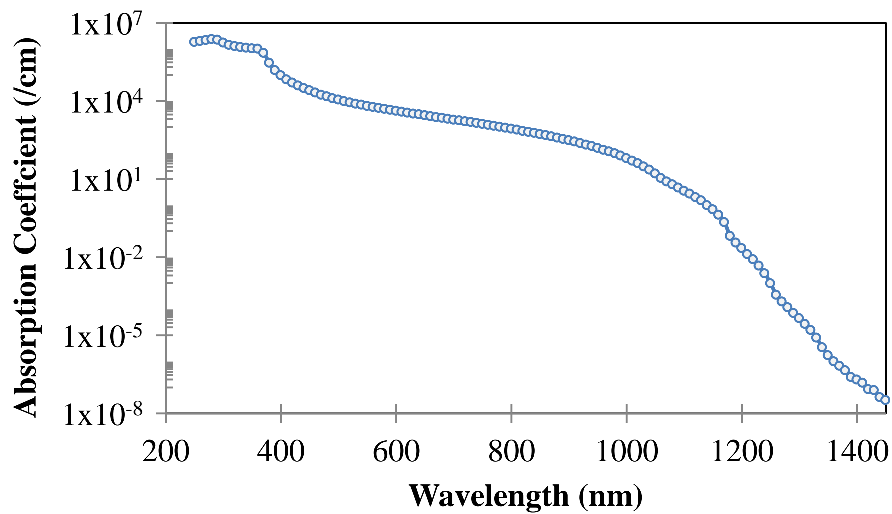

Figure 1.1: Absorption coefficient of silicon. Adapted from [4].

This energy-dependent absorption, in conjunction with surface defects, results in a unique external quantum efficiency (EQE) curve for each photovoltaic cell. The EQE curve for a typical SJSPVC is superimposed on the AM 1.5 G spectrum shown in Figure 1.2.

One approach to improve the SJSPVC's performance is to recognize that the cell efficiency is photon-energy-dependent. This dependency goes well beyond the below-bandgap cut-off. High energy photons, which are absorbed relatively near the surface on entering the cell, generate electron-hole pairs that suffer from high rates of

recombination. Charge carriers created near the surface have less chance of being collected due to their proximity to surface defects, which create non-radiative recombination centers. This causes a pronounced decrease in the EQE of a poor-quality cell at ultraviolet wavelengths (see Figure 1.2). Similarly, as the photon energy approaches the semiconductor band-edge, photons are not as likely to generate electron-hole pairs due to the low absorption of silicon as an indirect bandgap semiconductor, again resulting in a decreased EQE. The maximum EQE for a single-junction single-crystal silicon cell can be greater than 90% with a proper anti-reflection coating (ARC), in the range of 600 nm to 800 nm [5].

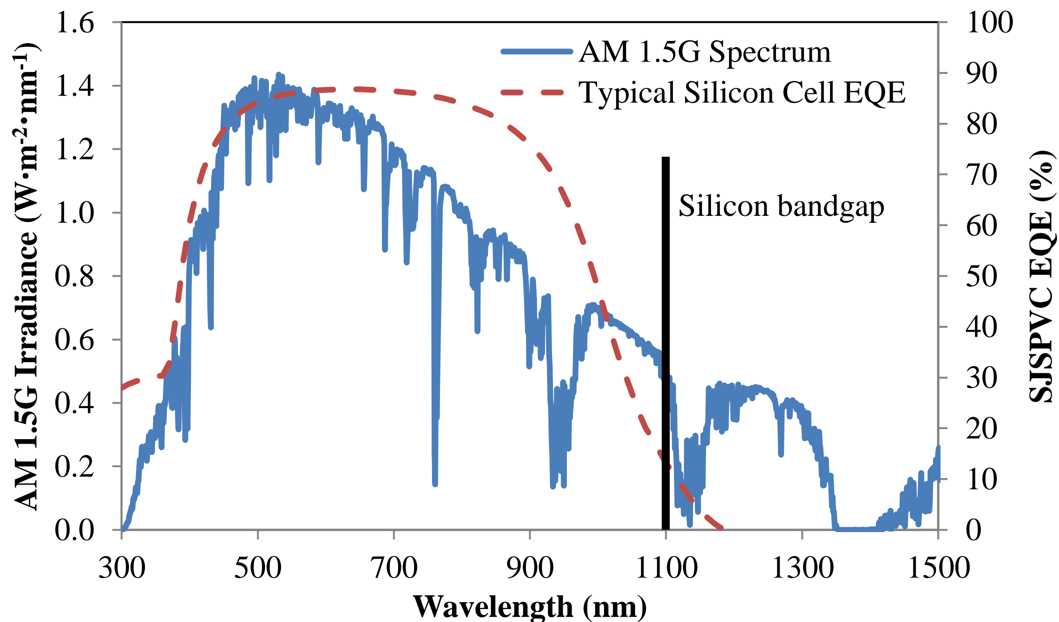

Figure 1.2: The external quantum efficiency for a representative SJSPVC peaks for photons with wavelength of approximately 700 nm (red). The solar spectrum (blue) is the Air-Mass 1.5 spectrum, which is the average solar irradiance received by the 48 contiguous U.S. states. Adapted from [6].

Several spectral engineering methods have been proposed in order to mitigate thermalization and/or surface recombination losses [7]. *Down-shifting* is a process whereby one high energy photon is absorbed, creating an excited electron which then

thermalizes to the band edge, and emits a photon at a lower energy, a phenomenon generally known as the Stokes' shift [8]. The down-shifter would be optically coupled to the cell, but it would be electronically isolated from the cell (see Figure 1.3). Down-shifting does not address thermalization losses; however it transforms a portion of the incident photons to wavelengths where the cell has more efficient energy conversion. Shifting the incident photon wavelength to a more efficient wavelength without changing the photon flux could improve cell performance, provided that photons are shifted from a region of lower EQE to a region of higher EQE, and provided that the conversion efficiency is "high enough".

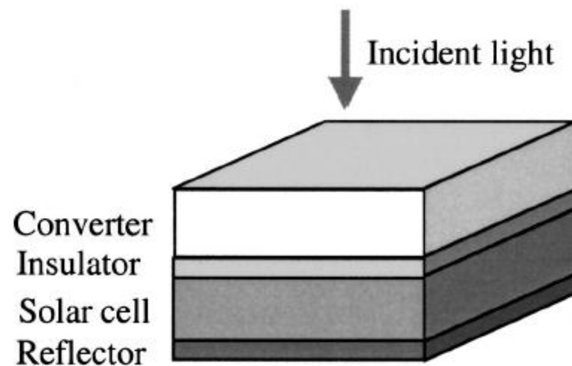

Figure 1.3: Schematic of an optically-coupled down-converting material placed on the front surface of a photovoltaic cell. Taken from [9].

It is important to recognize that the converter's effect on the cell performance is directly related to the converter's efficiency. Even if a converter material absorbed all of the high energy photons, it might not release as many lower energy photons. The converter's efficiency is calculated by counting the number of photons emitted at the desired wavelength, and dividing that number by the number of photons that were absorbed at the incident wavelength. A down-shifter placed on a silicon cell would ideally absorb no photons between the wavelengths of 550 nm – 1100 nm, since down-shifting those photons would not improve the cell's collection efficiency of those

photons. The starting material therefore should be optically transparent to most photons. However, a real converter applied to the front surface of a photovoltaic cell would likely also absorb a percentage of photons from all wavelengths in the solar spectrum. This becomes clear by considering that simply placing a piece of highly-transparent quartz on top of a solar cell would reduce the cell's performance. The converter needs to perform well enough that it also overcomes those intrinsic losses.

The modelling of the converter efficiency required to overcome intrinsic losses was performed by a collaborative group at the University of Ottawa. The modelling indicated that the required conversion efficiency to maintain the cell performance itself depends on the wavelength-dependent EQE of the PV cell. If the cell EQE is low in regions of high photon energies, a "luminescent down-shifting" material does not require a high conversion efficiency in order to improve the cell performance. However, the converter efficiency must approach 100% for regions where the cell EQE is high.

1.1.1 Modeling

Modeling was conducted using TCAD Sentaurus by Synopsys to determine optimal properties for a luminescence conversion material used with a SJSPVC. The modeled spectrum was applied to a cell with the parameters listed in [10]. As shown in Figure 1.4, it was found that a down-shifting efficiency of less than 100% could still result in an increase in cell performance, indicating that a down-shifter emitting at about 800 nm is indeed viable for spectral engineering for PV applications. The model parameters assumed 100% absorption above the bandgap (absorption) energy, and no absorption below the bandgap energy. Luminescence at 800 nm was modeled based on Gaussian emission centered at half the absorption energy.

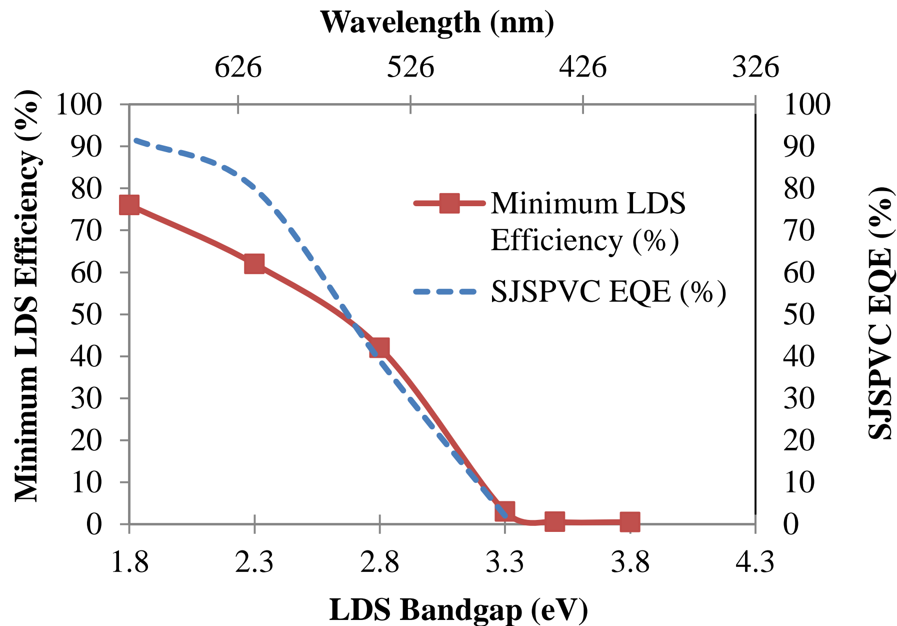

Figure 1.4: Modeled luminescent down-shifting (LDS) efficiency required to maintain the SJSPVC performance. The QE of the SJSPVC used in the converter model is shown as a dashed line. Note that in regions where the cell efficiency is low, the LDS efficiency does not need to be high in order to meet the minimum efficiency requirement. [10]

A second approach to spectral engineering is to recognize that the highest energy photons in the AM1.5 solar spectrum contain more than twice the energy of the silicon bandgap. This is true for all photons below ~550 nm. *Down-conversion* is the process of cutting one high energy photon into two lower energy photons, and it would also improve the cell performance. It has been estimated that down-conversion could improve the SJSPVC external quantum efficiency from 30.9% to 38.6% under 1 sun irradiance by placing an optical down-converter in front of a SJSPVC [9].

A third approach to spectral engineering is to convert sub-bandgap photons to usable (shorter) wavelengths through a process known as up-conversion. Up-conversion is a non-linear optical process, and the efficiency increase under 100 suns has been estimated to also increase the silicon cell performance from about 31% to 39% [11].

This thesis focuses on the first kind of spectral engineering materials: the down-shifters.

1.2 Motivation for photoluminescence quantum efficiency measurements

The materials used to create spectral engineering devices are photoluminescent materials. When photoluminescent materials are irradiated with single-wavelength light, they emit light of a significantly different wavelength. The research community has largely been interested in quantifying the excitation and peak wavelengths of these materials, and the intensity of the emission has been presented in arbitrary units of measurement. However, there is a growing interest to quantify the intensity of the photoluminescent emission [12-14], which would enable the comparison of the emission intensity from spectral engineering materials.

Photovoltaic technology is gradually reaching a consensus on how quantum efficiency should be measured, which is important in order to compare the performance of different photovoltaic cells [15]. However, photoluminescent materials have typically been presented by showing the peak photoluminescent wavelength, and the relative intensity if more than one sample is shown. It is impossible to use that data to compare the emission intensity with that of samples measured in another laboratory, or indeed, even to compare the emission intensity of samples measured in the same laboratory on a different day. In order for competitive progress to proceed on spectral engineering materials for photovoltaic applications, it is imperative that a consistent method of absolute quantum efficiency photoluminescent measurement be adopted by the research community.

1.3 Assumptions

This thesis assumes that the reader has a general knowledge of the physics of photovoltaic cell operation and limitations. An excellent on-line resource is [16], and a textbook resource is [17].

1.4 Thesis outline

The context of this thesis is guided by the opportunity to create ion implanted materials to modify the solar spectrum, and to measure their performance using a custom-built quantum efficiency measurement system. Specifically, this work focuses on measuring the quantum efficiency of the down-shifting of photons by silicon nanocrystals (Si-NCs) in fused silica, and the quantum efficiency of cerium-doped fused silica. The creation of Si-NCs in fused silica by the implantation of low energy silicon, the creation of Si-NCs in silicon by the implantation of low energy oxygen, the oxygen dependent nature of cerium photoluminescence, and energy transfer from Si-NCs to erbium are also presented.

This first chapter outlines the motivation for this work; the intrinsic limitation of SJSPVCs, the opportunity for a highly efficient conversion material to help overcome the resulting losses, and the additional requirement of characterizing the conversion performance of the conversion materials.

Down-shifting candidates are examined in Chapter 2. A brief discussion of the luminescent theory for Si-NCs and rare-earth elements is presented.

Chapter 3 introduces the ion implanter and the underlying physics of its operation, along with other experimental details, such as the photoluminescence quantum efficiency set-up, sample processing techniques, and sample characterization techniques, such as photoluminescence and ellipsometry. The equations used in quantum efficiency measurements are discussed.

Results are presented in Chapter 4. This includes the formation of a range of Si-NCs in quartz, photoluminescence from oxygen implanted into silicon, erbium-doped fused silica samples containing Si-NCs, and a study of the oxygen dependence of cerium photoluminescence.

Chapter 5 concludes the thesis by reviewing the results, and suggesting future work, in terms of the fabrication techniques, the materials characterization techniques, and the fabrication of functioning spectral engineering devices.

Chapter 2
Down-shifting Materials

2.1 General rules for down-shifters

There are a number of specifications that must be met in order to produce a useful spectral engineering material. Down-shifters must absorb high energy photons, and emit low energy photons, without also absorbing a significant number of above-bandgap low energy photons. The starting material must also be compatible with the available fabrication and/or processing techniques.

The designated fabrication technique for this project was ion implantation, which required a solid material capable of withstanding the requisite sample handling processes and high-temperature annealing. High purity fused silica (~ SiO_2) was predominantly used due to its excellent transmission of light, its robustness, its relatively low cost, its high glass transition temperature, and its compatibility with silicon enrichment to produce silicon nanocrystals (Si-NCs). Existing research indicated that silicon-rich fused silica would produce Si-NCs when processed correctly [18].

Down-shifting properties of rare-earths, particularly erbium and cerium, in Si-O environments were also investigated. This chapter is a primer to the current state of understanding regarding the photoluminescence of these materials.

2.2 Introduction to photoluminescence

Photoluminescence (PL) is used to probe the electronic transitions within the surface layer(s) of a material. Electromagnetic radiation is directed at a sample at one angle, and the radiation emitted by the sample (typically at a significantly different

wavelength) is collected at a different angle. Specifically, *down-shifting* materials absorb high energy photons and release low energy photons. PL is a non-destructive technique involving a light source, a collection lens, and a spectrometer in its most simple form. Generally, only the surface layers can be probed with PL because the incident light must reach the entities that will be excited, and the light emitted by those entities must also reach the collector. Thicker materials are likely to absorb either the excitation light or the emitted light; the exception is when the regions of interest are located deep within a highly-transparent material.

The excitation wavelength is important because a corresponding photon must contain enough energy to propel an electron out of its ground state into an excited state. Once the electron is in an excited state, it can return to the ground state by radiatively releasing energy (a photon), or by non-radiatively losing its energy to the surrounding environment, by creating phonons (lattice vibrations), or through Auger recombination (returning to the ground state by donating energy to an already-excited electron). A third de-excitation mechanism is for an excited state (donor) to transfer its energy to a nearby state (acceptor), which then either radiatively or non-radiatively relaxes to the ground state. "The PL intensity gives a measure of the relative rates of radiative and nonradiative recombination" [19].

2.3 Silicon nanocrystals

Silicon is the second most abundant element in the earth's crust, and established microelectronics processing techniques have driven down the price of silicon-based electronic products, which makes them economically attractive. However, efficient light emission from bulk silicon is inhibited by its indirect bandgap. The radiative recombination of electrons and holes is slow compared with other non-radiative recombination processes, such as Auger recombination, or defect-facilitated recombination.

However, volume-limited silicon, such as porous silicon or nanocrystalline silicon, emits strong, tunable, room-temperature photoluminescence (PL), and this discovery in 1990 [20] has led to a number of theories regarding the origin of the PL.

Silicon nanocrystals are three-dimensional groupings of silicon atoms within a non-silicon host. Often the conglomeration is less than 5 nm in diameter (although not necessarily spherical), and transmission electron microscopy images suggest that they are crystalline. The widely held belief is that Si-NC PL is the result of quantum confinement effects, where "the constraint of a phonon energy corresponding to a well-defined **k**-vector can disappear" [21] as movement of the electron-hole pair is volume limited. This results in discrete energy levels (electronic density of states) within the Si-NC when the Si-NC size is "comparable to or smaller than the exciton Bohr radius (~4.2 nm)" [22]. The Si-NC PL results from inter-band transitions between these energy levels. The energy level spacing is inversely related to the Si-NC size, which is evident in the solution to the zero-dimensional quantum structure form of the Schrödinger equation:

$$\Delta E = \frac{h^2}{8mr^2} i^2 , \qquad i = 1,2,3 \ldots \tag{1.1}$$

"where the electron state above the band gap is $\Delta E = h\upsilon - E_g$, with recombination energy $h\upsilon$, Si band gap E_g = 1.14 eV, effective mass m = 0.155 m_0, free electron mass m_0, nanoparticle size r, Planck constant h, and quantum number i" [23].

This quantum confinement theory has gained much support, including from the modelling community, where "theoretical calculations based on a quantum confinement model show good agreement with experimental measurements" [24]. Laboratory research exploring the relationship between photoluminescence peak wavelength (energy) and Si-NC size, like that shown in Figure 2.1, also supports the quantum confinement theory. Note that the PL peak blue-shifts with decreasing Si-NC size and smaller Si-NCs are expected to have larger spacing between their energy levels.

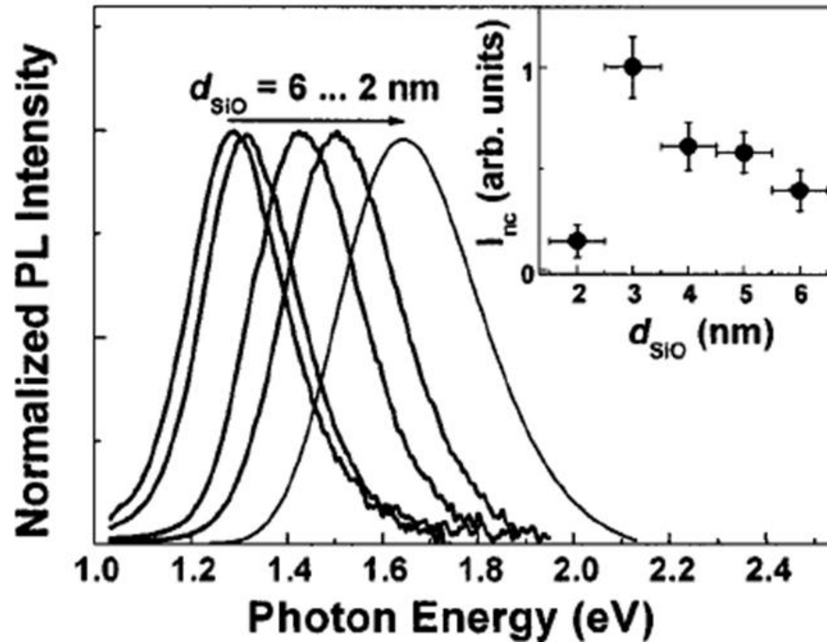

Figure 2.1: The photoluminescence from multilayered Si-rich SiO_2 and SiO_2 indicates that the peak photoluminescence location is related to Si-NC size [25].

There is some disagreement in the research community regarding the origin of Si-NC PL, however. Researchers have pointed to the large surface-to-volume ratio of Si-NCs to support the idea that surface states, such as Si-O, may be playing a dominant role in Si-NC light emission [26], and studies of PL from silicon dioxide nanoparticles, showing PL ranging from ~1.5 eV to ~2.2 eV, also lend support to this theory [27]. Indeed, a number of studies now suggest that surface oxidation of the Si-NCs is limiting the effects of quantum confinement [28], [24]. Another study indicates that Si-NCs are in fact still indirect bandgap materials [22].

Other studies show that terminating dangling bonds on the surface area of Si-NCs with hydrogen yields more intense PL. A study in 2006 claimed conversion efficiencies as high as 60% for Si-NC ensembles that have been coated with organic ligands and kept in a strictly oxygen-free environment [29].

Other work has shown that the PL peak wavelength is dependent on the excitation power [30]; the peak was red-shifted under high excitation power.

Whatever the origin of the PL, it is clear that the optical properties of Si-NC materials ought to be considered for down-shifting light applications to silicon photovoltaics, due to their absorption of high energy photons, and the emission of photons of wavelengths which overlap the maximum EQE range of a silicon cell (600 nm – 800 nm). In addition, the materials and processing techniques used to create Si-NCs are compatible with CMOS fabrication techniques. The challenge is to obtain high-enough conversion efficiencies for this down-shifting technology to yield photovoltaic performance improvement. "Quantum yields of ensembles of silicon quantum dots have generally been reported to be on the order of a few percents" [29]. Furthermore, the PL is released in random directions, irrespective of excitation direction, which is not ideal for a down-shifter located on top of a PV cell.

Si-NCs are commonly produced by sputtering [31], plasma-enhanced chemical vapour deposition [32], and ion implantation [18]. This thesis focuses on results obtained from silicon-nanocrystals fabricated using ion implantation, unless otherwise specified.

The behaviour of Si-NCs is illustrated by Figure 2.2. This figure shows the absorption and emission of Si-NCs formed through ion implantation, along with a TEM image of the same samples, and the following conclusions from the article were considered during the experimental planning phase:

1) Si-NCs have exponentially increasing absorption of light below about 500 nm.

2) These same samples emit a broad, Gaussian-type light spectrum which is typically centred around 800 nm, with a full-width half-maximum of almost 200 nm. The peak of this emission appears to shift with sample (the samples differ by

the implantation fluence of silicon in SiO_2), and the intensity of the emission also appears to be sample dependent.

3) The PL has been shown to red-shift with increasing nanoparticle size. Sample B contains larger Si-NCs than sample A, and the peak of the PL from sample B is at ~830 nm compared with the peak from sample A at about ~780 nm [30].

4) There is a range of Si-NC sizes in both samples.

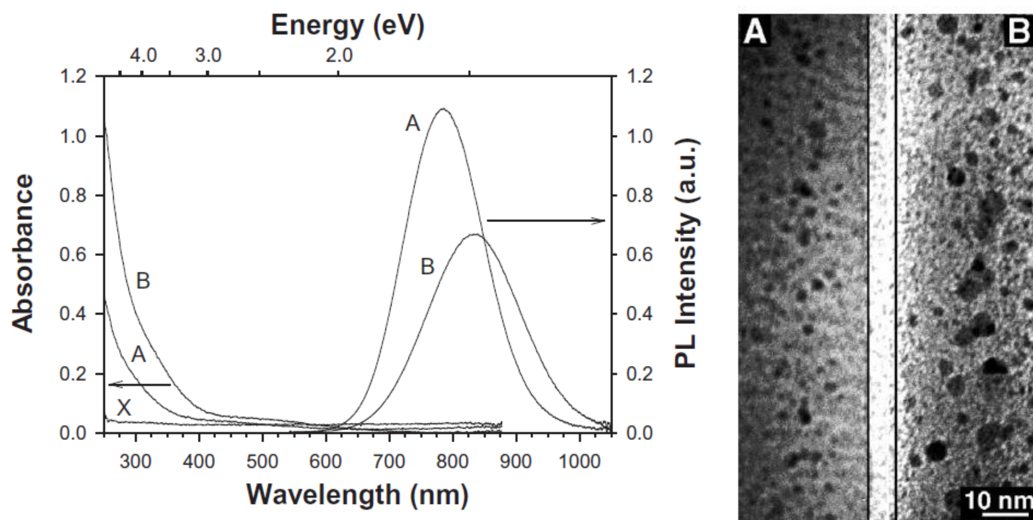

Figure 2.2: Absorption and PL emission from two ion implanted samples of Si-NCs in SiO_2 (adapted from [18]). Sample B was implanted with a higher fluence of silicon than sample A, resulting in red-shifted PL from sample B compared with the PL from sample A. Note that the absorption takes place predominantly below 400 nm.

2.4 Lanthanide rare-earths

Most of the lanthanide rare-earths, like erbium, are actually quite abundant, are isotopically stable, and generally have narrow absorption and emission bands which do not change significantly with changing host material [33]. This last characteristic is due to the fact that electron transitions occur from 4*f*-4*f* orbitals, and this orbital is partially shielded from the surrounding environment by the 5*s* and 5*p* orbitals. The intra-orbital

transition is parity-forbidden, however for the rare-earth orbitals it is believed that these transitions are weakly allowed due to asymmetry in the orbital induced by the host environment [34]. The improbability of the transition causes the excited states to have lifetimes often in the hundreds of microseconds, leading to the label "metastable". The existence of metastable states means that up-conversion, or the further excitation of excited states, is more likely. The lanthanide series in the periodic table is indicated in Figure 2.3.

H																															He
Li	Be																									B	C	N	O	F	Ne
Na	Mg																									Al	Si	P	S	Cl	Ar
K	Ca															Sc	Ti	V	Cr	Mn	Fe	Co	Ni	Cu	Zn	Ga	Ge	As	Se	Br	Kr
Rb	Sr															Y	Zr	Nb	Mo	Tc	Ru	Rh	Pd	Ag	Cd	In	Sn	Sb	Te	I	Xe
Cs	Ba	La	Ce	Pr	Nd	Pm	Sm	Eu	Gd	Tb	Dy	Ho	Er	Tm	Yb	Lu	Hf	Ta	W	Re	Os	Ir	Pt	Au	Hg	Ti	Pb	Bi	Po	At	Rn
Fr	Ra	Ac	Th	Pa	U	Np	Pu	Am	Cm	Bk	Cf	Es	Fm	Md	No	Lr	Rf	Ob	Sg	Bh	Hs	Mt	Os	Rg	Cn	Uut	Uuq	Uup	Uuh	Uus	Uuo

Figure 2.3: Periodic table of the elements showing the lanthanide rare-earths highlighted in yellow. Adapted from [35].

The electronic structure of the lanthanides is described as follows by [33]:

> From the perspective of optical and electronic properties, the most important feature of rare earths is the lanthanide contraction. This is a consequence of imperfect screening by the 4*f* electrons, which leads to an increase in effective nuclear charge as the atomic number increases in the lanthanide series. As a result, the 4*f* electrons become increasingly more tightly bound with increasing *Z*. While neutral lanthanum (La) has the xenon structure plus $5d6s^2$, the electrons that are added for the neutral elements that follow are found in the 4*f* shell and only Ce, gadolinium (Gd) and Lu have a 5*d* electron. In terms of their spatial extent, the 4*f* wave functions for La (Z = 57) lie outside the xenon shell, but by neodymium (Nd, Z = 60) they have contracted so much that the maximum lies within the $5s^25p^6$ closed shells of the xenon structure.

> In condensed matter the trivalent (3+) level of ionization is the most stable for lanthanide ions. (…) Ionization preferentially removes the 6*s* and 5*d* electrons, and the electronic configuration for these ions (…) is that of the xenon structure plus a certain number (1-14) of 4*f* electrons. (p.19)

The radiative performance of rare earths depends strongly on the host material in which they are embedded. Lanthanide rare-earths are more likely to radiatively relax if their excited state is not coupled to phonon energies of the host matrix. Hence the use of low-phonon energy material, such as the ZrF_4-BaF_2-LaF_3-AlF_3-NaF (ZBLAN) family of glasses, or fluorochloro-zirconate glass [36], or chalcogenated glasses [37-38].

Even when high emission intensity is obtained, most rare-earths have narrow absorption bands, which limit their usefulness in capturing the broad solar spectrum. For example, Meijer *et al.* report 140% conversion efficiency for Nd^{3+} transferred to Yb^{3+}, however Nd^{3+} has narrow absorption wavelengths, and more ingenious devices are needed to capture the broad solar spectrum [39]. (This greater-than-100% conversion efficiency is indicative of the down-conversion process introduced in Chapter 1.) In addition, the emission intensity from Yb^{3+} at 980 nm decreases significantly with increasing temperature (4 – 300 K).

2.5 Energy transfer from silicon nanocrystals to lanthanide rare-earths

One method of broadening the absorption spectrum of rare-earths is to create a heterogeneous system involving both Si-NCs and rare-earth ions. Si-NCs capture high energy photons using the broad absorption cross-section of silicon nanocrystals, and transfer the captured energy to a secondary emitter. This receiving species could be a rare-earth element, which would then emit at the emission band(s) permitted by the host-

matrix. An example of this type of energy transfer is shown in Figure 2.4, where Si-NCs transfer energy to erbium ions in a SiO_2 matrix.

Optimizing energy transfer presents many challenges, including optimizing the spacing between the Si-NCs and the rare-earth ions, and overcoming competing processes like energy transfer between the Si-NCs themselves [40], and cooperative up-conversion [41]. Optimization of the concentration of Si-NCs as well as erbium ions is also required [42]. Furthermore, the size of the Si-NCs is critical, since Si-NCs larger than about 4 nm have a reduced energy transfer towards rare earth ions "because of the weak confinement of carriers and the loss of resonant excitation of Er through the upper levels (second, third, . . .)" [43].

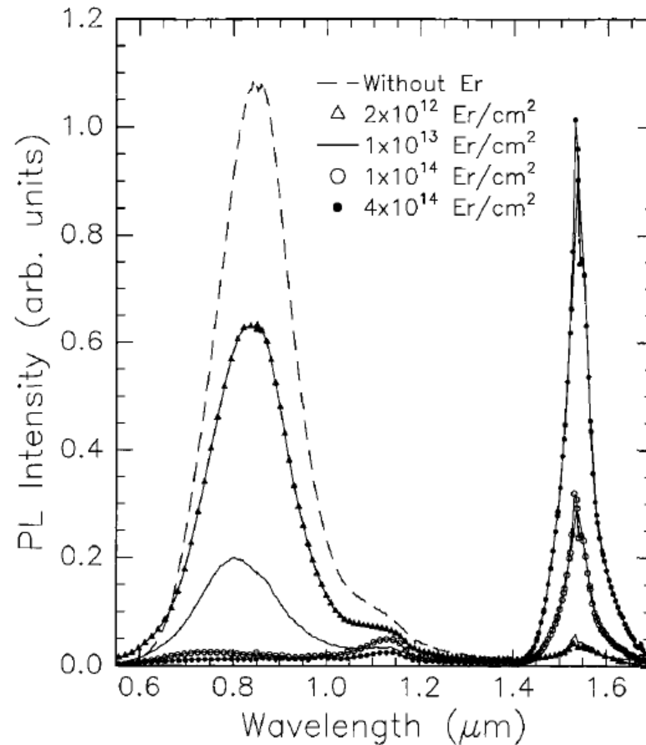

Figure 2.4: Energy transfer between Si-NC in SiO_2 and Er^{3+} ions. As the implanted erbium fluence increases, the PL from erbium (at 1.54 μm) also increases, and the PL from the Si-NCs (at 0.8 μm) decreases. Taken from [44].

A similar down-shifting experiment was also performed with Si-NCs and Neodymium (Nd^{3+}). It was found that adding too much Nd^{3+} (> 0.08 at. %) to silicon-rich silicon dioxide results in quenching of the Nd^{3+} PL [45]. This is likely due to precipitation (conglomeration) of the rare-earth ions, forming additional non-radiative pathways.

2.6 Cerium as a down-shifter

Cerium is the most abundant of the lanthanide rare earth elements, and one of the least well understood. Its 4f orbital does not benefit from the same 5s and 5p electron shielding that produces consistent energy levels in a variety of host materials for the succeeding lanthanides. Energy transitions in cerium are particularly susceptible to changes in the host environment. This host environment affects both the spacing of the energy transitions and their radiative probability. Despite the deficiency of knowledge on cerium's radiative behaviour, cerium is a contender in the creation of solid-state white light-emitting devices [46], and could be used as a down-shifting material for UV photons. Digonnet comments on cerium's absorption versus the other rare-earths [33]:

> The observed infrared (IR) and visible optical spectra of trivalent rare earth ions is a consequence of wavelengths less than 300 nm, although for a few, notably Ce^{3+} and trivalent praseodymium (Pr^{3+}), 5*d* levels lie low enough to produce strong, broad absorption bands in the ultraviolet." p.19

This sounded promising, so an investigation into the factors that affect cerium luminescence was conducted.

Cerium has broad UV light absorption between 250 nm and 400 nm, with two absorption bands peaking around 310 nm and 350 nm and emission generally between 400 nm and 550 nm, depending on the host matrix [46]. The emission and absorption levels are not as stable as they are for erbium, because the radiative emission occurs from

the 5d to the 4f orbital. "Unlike 4*f*-4*f* transitions, 4*f*-5*d* transitions are allowed, which results in strong and broad absorption cross-sections[1]," [34] as well as strong and broad PL emission, even at room temperature [47].

2.7 Chapter summary

The mechanisms of PL emission were introduced. For Si-NCs, there is much research to support the theory that PL is the result of quantum confinement, although surface-state properties appear to also play a role in the intensity and the wavelength of the emission. Si-NCs have broad UV absorption, and they emit light at about 800 nm, which nearly corresponds with the peak EQE of a silicon PV cell. These latter characteristics are ideal for capturing and emitting photons in the solar spectrum for down-shifting,

The lanthanide rare-earths were also introduced. These elements tend to have narrow and weak absorption and emission bands, which raises the desire to couple emitting rare-earths to absorbing Si-NCs using energy transfer mechanisms, in order to capture the broad UV solar spectrum.

Cerium is exceptional among the lanthanide rare-earths, in that it does have broad UV absorption and strong room temperature emission around 450 nm, although the emission and absorption wavelengths depend on the host-material.

The fabrication of samples incorporating these different down-shifters is discussed in Chapter 3.

[1] "In 4*f*-5*d* transitions, one of the 4*f* electrons is excited to a 5*d* orbital of higher energy. This type of excitation absorption is usually denoted $4f^{\,n} \rightarrow 4f^{\,n-1}5d$ and is typically observed in Ce^{3+} ions ($4f^{\,1}$ configuration). Since empty, half filled or completely filled electron shell configurations are the most stable ones, the excess 4*f* electron of Ce^{3+} is easily transferred to the 5*d* orbital." [34]

Chapter 3

Experimental Methods

The following sections describe the steps for sample fabrication, including substrate choice, sample dicing and cleaning, ion implantation, and rapid thermal annealing. The parameters used to create each sample are presented. The characterization techniques, including photoluminescence, the step-by-step process of performing a quantum efficiency measurement, and variable angle spectroscopic ellipsometry (VASE), are discussed.

3.1 Starting materials

i) Silicon nanocrystals for quantum efficiency measurements

Fused silica (SiO_2) was chosen as the host material for silicon nanocrystal (Si-NC) creation for the quantum efficiency measurements, since a 0.5 mm-thick piece of fused silica transmits >90% of the photons between about 200 nm and 2000 nm [48]. High-purity fused silica can be purchased for a reasonable price, and it is a robust material, which could eventually be incorporated into the photovoltaic cell encapsulation. The fused silica used for this research came from UQG Optics, the 25.4 mm x 25.4 mm x 0.5 mm thick UV fused silica Spectrosil® 2000 UV coverslips (CFS-2525). This material was also used for the creation of a cerium-doped sample for quantum efficiency photoluminescence studies.

ii) Silicon nanocrystal-type photoluminescence via oxygen implantation

A low-doped p-type <1-0-0> Czochralski silicon wafer was used for the implantation of oxygen into silicon with the goal of forming Si-NCs.

iii) Cerium luminescence in oxygen-doped silicon nitride

Low-pressure chemical vapour deposited (LPCVD) silicon nitride (Si_3N_4) 50 nm thick on a silicon wafer was obtained from Carleton University. The LPCVD process does not require the use of oxygen-contaminated carrier gasses, and thus results in a higher-purity film than plasma-enhanced chemical vapour deposition (PECVD), for example [49]. This material was used to explore the contribution of oxygen to cerium photoluminescence.

3.2 Sample dicing

The quartz was diced into (approximately) 6.25 mm x 6.25 mm x 0.5 mm pieces using a 0.1 mm thick resin-bonded saw blade and a MicroAce Series 3 dicing saw from Loadpoint Limited. A standard operating procedure (SOP) was composed for the operation of this machine (Appendix A).

The LPCVD Si_3N_4 material was diced using a 50 μm thick Disco saw blade (ZH05-SD4800 N1-50).

The silicon wafer was diced by hand using a diamond-tipped scribe.

3.3 Sample cleaning

The diced materials were cleaned to remove dicing tape residue and particulates. The cleaning process followed was:

- a five-minute ultra-sonic bath in acetone,
- a second five-minute ultra-sonic bath in another glass of acetone,
- a five minute ultrasonic bath in methanol,
- a dip in 18 MΩ de-ionised water, and then
- the samples were dried using nitrogen gas.

3.4 Ion implantation

Ion implantation is the process of shooting selected ions into a target material. A plasma of ions is first created under vacuum conditions (10^{-6} Torr), and ions are drawn out of the plasma chamber through an aperture by a relatively small voltage potential, and are then accelerated by a larger voltage potential toward an analyzing magnet. The larger voltage potential is varied to control the travelling velocity of the ions. The strength of the magnet is dependent on the current fed through the coils which form the magnet poles, and the magnet's strength determines how much Lorentzian force each ion experiences. The degree of curvature which the ion undergoes due to normal acceleration depends on the mass of the ion, so that only ions of the same mass emerge after a 90° bend in the ion path. Heavier ions will not experience enough normal acceleration to pass around the bend, and will smash into the outer wall of the elbow, and lighter ions will be over-accelerated into the inner wall of the elbow. The successfully-transmitted isotope of the chosen element is directed down a line (with a slight deviation to remove de-ionized charges) and into the sample, which is housed in the target chamber. A simple schematic of the ion implanter is shown in Figure 3.1, however more detail on the ion implantation process can be found in [50].

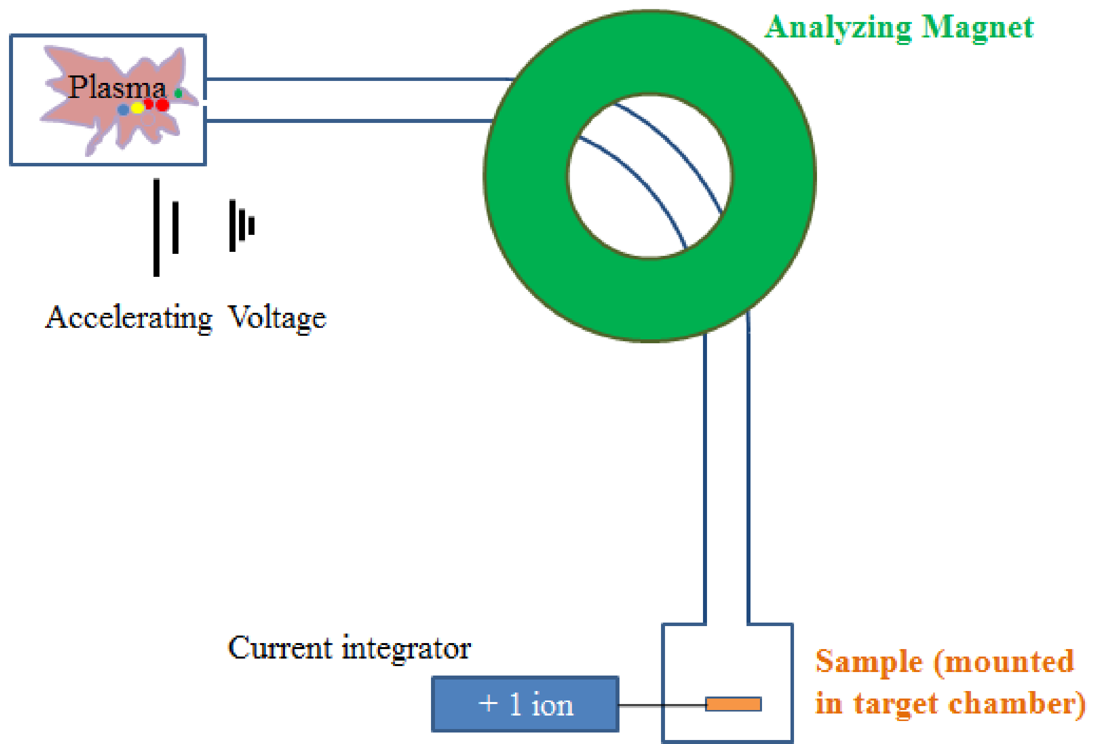

Figure 3.1: Simple schematic of the ion implanter. Ions created in the plasma are accelerated toward an analyzing magnet, which limits the combination of mass and charge which reach the sample mounted in the target chamber.

Ions that reach the target material are eventually slowed to a stop by the material, provided that it is thick enough. During stopping, the ion will break atomic bonds, and displace host atoms. The ions will penetrate into the host material to a depth which can be approximated using the Stopping and Range of Ions in Matter (SRIM) code [51], which is a freely-available software program based on Monte-Carlo statistics, which considers the accelerating voltage, the mass of the ion, and the target composition in order to determine the average penetration distance (peak range) and straggle of the implanted ions [52]. The ions end up in a Gaussian-type distribution, with straggle depending on the ion mass (see Figure 3.2). The simulation program outputs data in the

units of (atoms/cm^3) / (atoms/cm^2). The concentration of the implanted ions can be calculated by multiplying the SRIM output by the implanted fluence (atoms/cm^2).

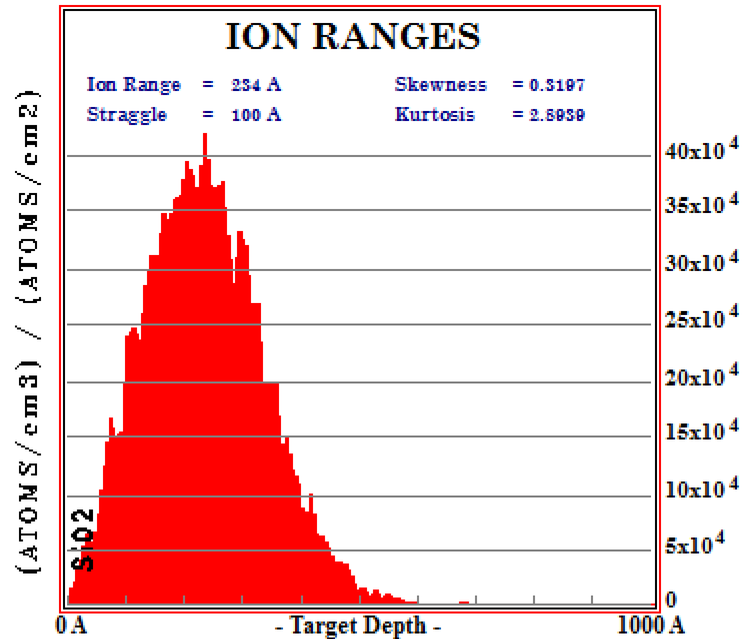

Figure 3.2: Example of output from SRIM software, showing the implantation depth on the x-axis.

Ion implantation is an elegant research tool since it is possible to precisely control the number and the type of ions that are added to a sample, within some experimental error. This means that is it possible to replicate samples throughout the course of a study. There are some operational challenges when attempting to accurately integrate the number of added ions, since when a positively charged ion impinges on a sample, it is possible that an electron (negative charge) will be ejected from the material, resulting in an apparent increase in positively-charged implanted ions. In the system used for this project, these ejected charges were "deviated" by a permanent magnet. The success of this magnetic electron suppression was evident when the current from the ion beam on the beam stop used for beam set-up (where there was no permanent magnet) was compared with the current from the ion-beam on the sample (permanent magnet). The

latter case resulted in a decrease in the apparent ion beam current (from 10 μA to 8 μA, for example).

Ion implantation is additionally valuable since only one isotope of one element enters the host material, which disambiguates the effect that certain elements/isotopes have on the properties of the resultant material, an effect that has been investigated for silicon nanocrystals [53]. Ion implantation has some random error and some systematic error. The systematic error is the variation expected from day-to-day operational changes, including the challenge of setting the implantation voltage at "exactly" the same level. This systematic error is approximately ± 5% of the number of implanted ions. However, the random error is lower; counting the number or ions is performed digitally, so that error is limited to ±0.5 of a "count". The number of ions in a count depends on the chosen scale for the current integrator, and was typically on the order of 1×10^{13} positive charges per centimeter squared per count. If a series of samples is created at constant implantation energy, starting with all the samples in the implantation chamber, and sequentially removing a sample each time a fixed number of counts (corresponding to a Δfluence) is reached (the procedure used for all the series of samples created for this thesis), then the relative error of the number of ions between each sample is quite small.

3.4.1 Selecting an ion for implantation

The ion chosen for implantation can be "seen" on an oscilloscope that measures the charge that hits the beam set-up flag. The current through the selector magnet sweeps ± a couple of amps to generate a view of the selected ion (centred on the oscilloscope – which pulls its current reading from the ions impinging on the flag). There are a couple of methods used to determine which ion is centred on the oscilloscope. The plasma carrier gas, often argon, can be switched off or on, and the argon peak can then be observed to decrease or increase, respectively. Once the argon peak has been identified, the corresponding analyzer magnet current is noted. The mass of an ion producing any other peak can then be determined by considering the ratio of the two analyzer currents,

and the atomic mass of argon. Given knowledge of the loaded elements, and of elements used in previous runs which might have left some small contamination on the plasma chamber walls, it is usually possible to accurately identify ion peaks. A second approach is to observe the isotopic profiles of the ions that appear on the oscilloscope; for silicon, the percent abundance is 92%, 5%, 3% for Si^{28}, Si^{29}, and Si^{30}, respectively.

3.4.2 Practical considerations

The ion implantations performed for this thesis were all with the target oriented at an angle of 7°, which was the standard orientation chosen to avoid channelling of implanted ions through the lattice channels in silicon wafers (even though this was not a consideration for most of the cases). Implantations were performed under a vacuum of approximately (10^{-6} Torr), and the ion beam was continuously rastered in both the x- and y-directions, to produce a uniform doping.

The pieces of the target samples were bonded to a larger silicon (dummy) wafer, which had been "burned" (placed in front of an argon ion beam for a few minutes to produce a discoloration indicating the beam spot-size). The samples were then glued within 2 mm of the edge of the burn-mark using clear nail polish, which was cured at >90 °C. The wafer with the samples was placed into the target chamber. After implantation, the larger silicon wafer was again heated to >90 °C, and the samples were removed one-by-one and wiped with methanol to remove nail-polish residue.

3.4.3 Implanted ions, energies, and fluences

The implanted ions, implantation energies, and fluences for the samples discussed in this thesis are listed in Table 3.1. The results of the SRIM simulations for each implantation are shown in Appendix B.

Table 3.1: Sample substrates, ion implanted, implantation energies, and fluences used in this thesis.

Sample Substrate	Implanted Ion	Implantation Energy (keV)	Fluence (ions/cm^2)
Fused silica	Si^+	15	$1.35x10^{16}$, $1.80x10^{16}$, $1.95x10^{16}$, $2.10x10^{16}$, $2.25x10^{16}$, $2.40x10^{16}$, $2.55x10^{16}$, $2.70x10^{16}$, $2.85x10^{16}$, $3.00x10^{16}$, $3.04x10^{16}$, $3.21x10^{16}$, $3.38x10^{16}$, $3.54x10^{16}$
Silicon <1-0-0> p-doped	O_2^+	19	$5.50x10^{16}$, $5.65x10^{16}$
LPCVD Si_3N_4 (50 nm) on Silicon	Ce^+	25	$1.0x10^{15}$, $3.0x10^{15}$, $5.0x10^{15}$
LPCVD Si_3N_4 (50 nm) containing implanted cerium on Silicon	O_2^+	19	$5.0x10^{15}$, $2.00x10^{16}$, $3.50x10^{16}$, $5.00x10^{16}$
Fused silica	Ce^+	25	$3.0x10^{15}$
Fused silica with silicon implanted: $2.10x10^{16}$ $3.04x10^{16}$	Ce^+	25	$3.0x10^{15}$
Fused silica with Si-NCs formed through Si-implantation: $3.04x10^{16}$, $3.21x10^{16}$ $3.38x10^{16}$, $3.54x10^{16}$	Er^+	35	$2.75x10^{14}$

3.5 Rapid thermal annealing

After implantation and ultrasonic cleaning, the samples were heated to a high temperature to 1) remove lattice damage caused by ion implantation, and 2) induce Si-NC formation, and/or 3) electrically activate dopants in the host matrix. The Jipelec Jetfirst rapid thermal annealer (RTA) used halogen lamps to heat up the samples using electromagnetic radiation. Because the substrate holder is about 4 inches in diameter, a bank of lamps is needed to anneal uniformly. The advantage of rapid thermal annealing versus furnace annealing is discussed in [49]. The temperature in the chamber is sensed using a pyrometer for temperatures >400 °C. The pyrometer is calibrated using stored data that adjust the temperature depending on previous test results. Refer to Appendix C for a method of calibrating the RTA temperature using the growth of thermal oxide. A typical recipe is schematically shown in Figure 3.3 below for creating Si-NCs.

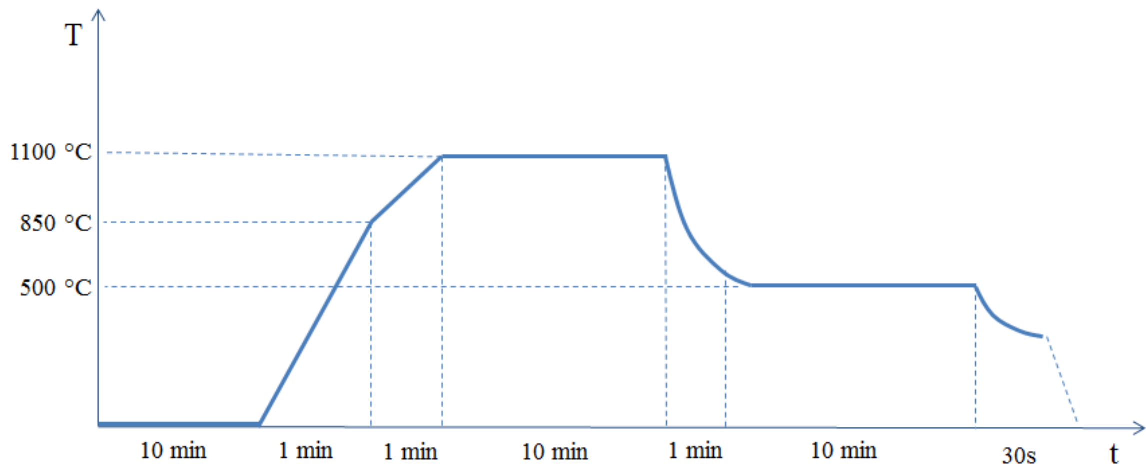

Figure 3.3: Typical RTA recipe for Si-NC formation after silicon or oxygen implantation. Nitrogen gas flowed through the RTA from the beginning of the recipe until the temperature dropped to 500 °C for 10 minutes; 5% H_2 : N_2 was flowing during the remainder of the run.

A typical recipe for annealing the cerium-doped samples is shown in Figure 3.4 below.

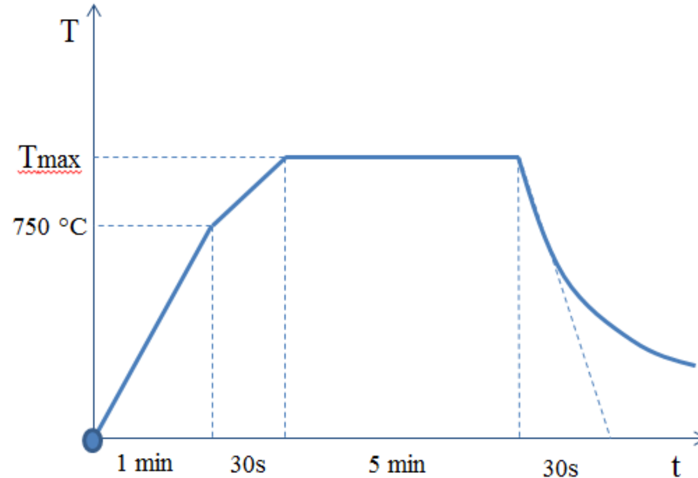

Figure 3.4: Typical RTA recipe for cerium-doped samples. T_{max} was typically 1000° C.

3.6 Implanting and annealing recipes for the fabrication of doped and undoped silicon nanocrystal and/or rare-earth-containing samples

i) Silicon nanocrystals

Si-NCs were fabricated using ion implantation of silicon (Si^+) at 15 keV into 0.5 mm thick UV fused silica Spectrosil® 2000 UV coverslips (CFS-2525) from UQG Optics as substrates. Fluences of 1.35 $x10^{16}$ Si^+/cm^2 to 3.54 $x10^{16}$ Si^+/cm^2 were implanted. An attempt was made to fabricate Si-NCs by implanting molecular oxygen (O_2^+) at 19 keV into a lightly doped p-type single-crystalline silicon wafer. (The corresponding SRIM simulation was run as a single oxygen – $^{16}O^+$ ion – implanted at half the energy, i.e. 9.5 keV). Fluences of $5.50x10^{16}$ O_2^+/cm^2 and $5.65x10^{16}$ O_2^+/cm^2 were implanted at 19 keV. Both types of samples were annealed in a rapid-thermal processor for 10 minutes at 1100°C in a nitrogen environment, and then passivated at 500°C in 5% $H_2:N_2$ for 10 minutes.

ii) Erbium

Erbium was implanted into four fused-silica samples, already containing Si-NCs. The erbium implantation energy was chosen so that the peak erbium concentration would coincide with the peak silicon implantation used to create the Si-NCs, and the erbium fluence was back-calculated after choosing the peak erbium concentration from a reference paper [54]. The samples were annealed at 900 °C after the erbium implantation for 10 minutes, followed by 10 minutes at 500 °C.

iii) Cerium

Silicon nitride (Si_3N_4) was deposited onto a p-type (100) silicon wafer to a thickness of 50 nm using LPCVD. Cerium ions were subsequently implanted at 25 keV into the Si_3N_4 to a peak concentration of 3.9 $\times 10^{21}$ Ce^+/cm^3, as calculated using SRIM simulation software. All but one of the Si_3N_4 cerium-doped samples were further implanted with oxygen. A range of O_2^+ fluences were used at the same energy of 25 keV. The samples were then annealed in a rapid thermal processor at 1000 °C for five minutes in a flowing nitrogen environment.

Cerium was also implanted into fused silica SiO_2 to a fluence of 3×10^{15} Ce^+/cm^2 at 25 keV, to compare the PL intensity with that obtained from the cerium-doped Si_3N_4 samples. The sample was annealed for 5 minutes in a flowing nitrogen environment.

3.7 Photoluminescence characterization

Samples that had been implanted, cleaned, and annealed were subsequently characterized to determine their performance as spectral engineering down-shifters and light emitters. The primary interest was the intensity and wavelength of the photoluminescence (PL). The PL was initially collected after pumping using a 405 nm solid state laser (~16 mW), and a collection lens placed normal to the sample surface. A standard operating procedure (SOP) was written for this set-up (Appendix D). Light was

coupled from the collector lens into an optical fibre, which connected to a USB 2000+ UV-VIS charge-coupled device (CCD) from Ocean Optics [55]. The CCD was connected to a computer, and the computer monitor displayed the real-time readings from the CCD using a software packaged called SpectraSuite (also from Ocean Optics). The PL intensity was displayed in "arbitrary counts" versus photon wavelength.

3.7.1 Calibration of the charge-coupled device

The CCD from Ocean Optics was calibrated to account for the variability in pixel response with photon wavelength – similar to the variation in external quantum efficiency (EQE) of a solar cell with wavelength. This calibration was performed using a broadband light source of known irradiance from Ocean Optics, the LS-1-CAL lamp [56]. The resulting absolute irradiance curve was displayed in μW/cm^2/nm. This absolute irradiance measurement resulted in a peak shift compared with the "counts" (see Figure 3.5). The graph below compares the Si-NC PL profile obtained with a calibrated and an uncalibrated CCD.

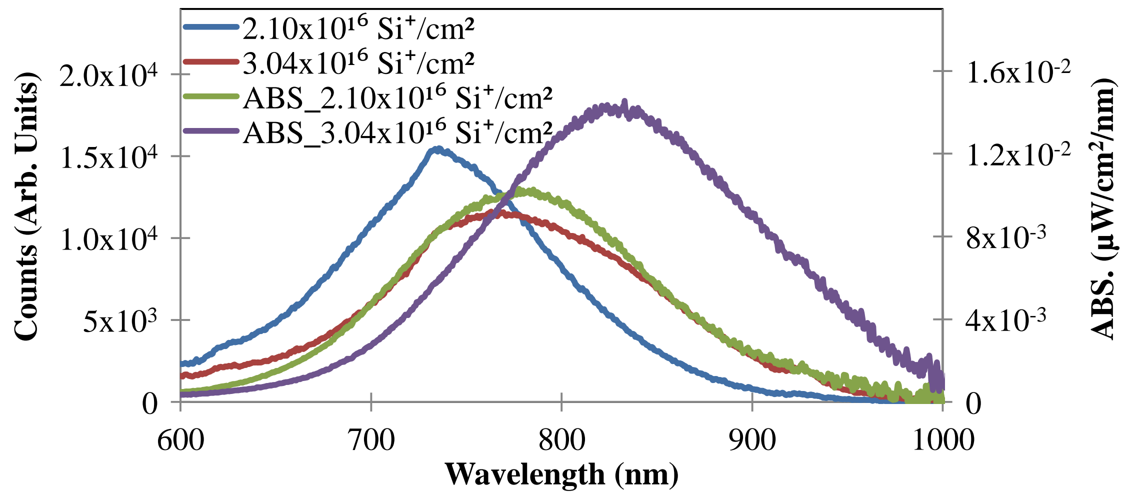

Figure 3.5: Comparison of PL obtained from two samples, measured with a calibrated (ABS, right vertical axis) and an uncalibrated CCD, and excited with a 405 nm laser line. There is some red-shifting of the peak wavelength, particularly at wavelengths that are close to the silicon bandgap of the detector.

Some of the early photoluminescence measurements taken for this project were taken using the uncalibrated CCD. Some of the samples were further processed before the LS-1 CAL lamp arrived to calibrate the CCD, so uncalibrated PL results are sometimes shown in Chapter 4.

The peak is clearly red-shifted once the CCD response is calibrated. This is likely due to the fact that the CCD contains a silicon detector, which would have a limited response as the bandgap is approached (the EQE of a silicon photovoltaic cell shown in Chapter 2 also drops off approaching the bandgap). Shining a lamp of known irradiance into the CCD enables the calibration of the response, which is then automatically corrected using SpectroSuite software.

Once the CCD response was calibrated, further work was required in order to obtain an absolute quantum efficiency measurement.

3.7.2 Quantum efficiency measurement

In order to quantify the Si-NC PL efficiency, an absolute quantum efficiency (QE) setup was implemented according to reference [57], which shows a schematic diagram of an equivalent system. Laser light is incident on a sample mounted in the centre of an integrating sphere. The diffuse irradiance from within the sphere is coupled into an optical fiber connected to a CCD array, which was calibrated as previously described. Refer to Figure 3.6 for a schematic of the set-up.

The sphere response, R_s, was calculated based on the fiber cross-sectional and sphere surficial areas, A_f and A_s, respectively, the wavelength-dependent reflectance of the sphere's interior coating, $\rho(\lambda)$, the port fraction, f, the facial reflectance, R, and solid angle of the fiber, Ω, [58]. This response is given by

$$R_s = \frac{\rho(\lambda) \cdot A_f (1-R) \cdot \Omega}{\pi A_s (1-\rho(\lambda) \cdot (1-f))} \ , \tag{3.1}$$

which allows the measured spectrum to be corrected for losses within the sphere, and for coupling inefficiencies from the sphere to the CCD.

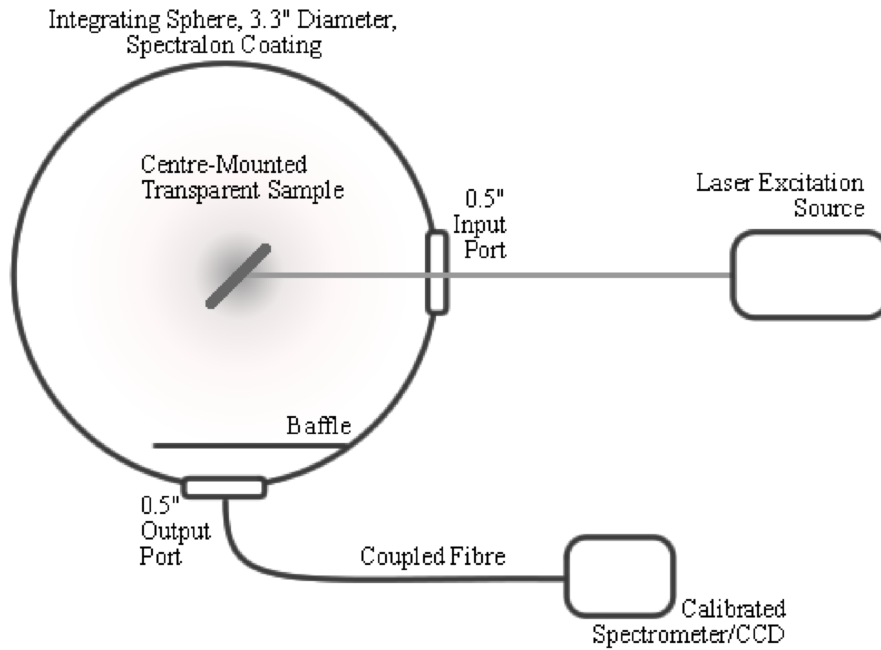

Figure 3.6: Schematic of the integrating sphere quantum efficiency photoluminescence set-up. (Figure credit: Justin Sacks).

It is important to distinguish between the optical-converter efficiency and the solar-cell efficiency. When referring to an optical-converter, EQE and IQE (internal quantum efficiency) are defined by

$$EQE = \frac{\phi_{emitted}(\lambda)}{\phi_{incident}(\lambda)} \tag{3.2}$$

and

$$IQE = \frac{\phi_{emitted}(\lambda)}{\phi_{absorbed}(\lambda)} \quad , \tag{3.3}$$

respectively, where $\Phi_{incident}$ is the photon flux incident on the converter, $\Phi_{absorbed}$ is the portion of $\Phi_{incident}$ absorbed by the converting material, and $\Phi_{emitted}$ is the converted spectral photon flux emitted by the converter, as shown in Figure 3.7. Since an absorbed photon will not necessarily result in an emitted photon, down-shifting will always give an IQE less than or equal to 100%.

In the PV research community, EQE and IQE refer to the number of charge carriers generated per incident or absorbed photon, respectively.

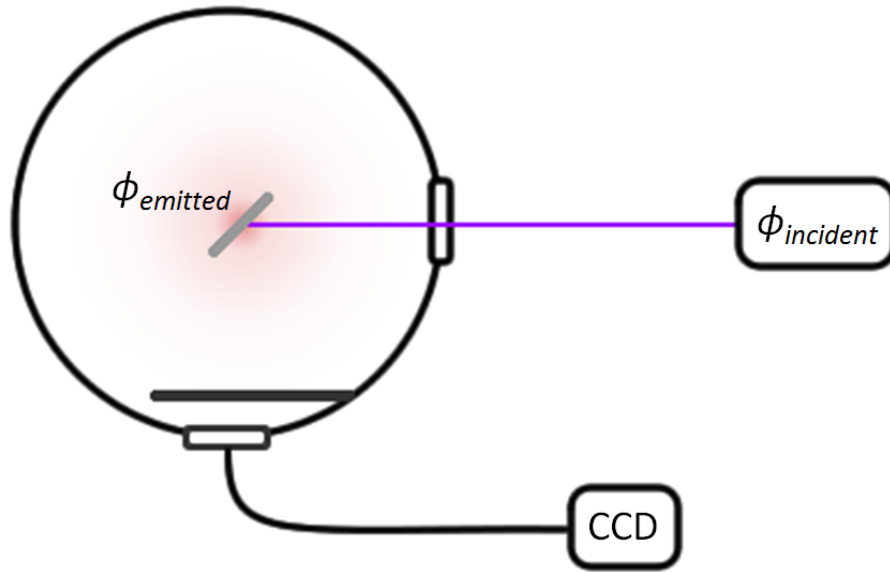

Figure 3.7: Photoluminescence shown as $\varphi_{emitted}$, and incident laser light shown as $\varphi_{incident}$. Taken from [59].

To calculate the efficiencies of a down-shifting material, it was necessary to know the precise spectral photon flux in and out of the integrating sphere. The calibrated CCD measured absolute irradiance [μW/cm^2/nm], which was converted into a photon flux [photons/s/cm^2/nm]. The full QE calculation is outlined in [57].

In order to calculate the IQE of the Si-NCs, the absorbed photon flux was calculated as

$$\phi_{absorbed_nc}(\lambda) = \phi_{fs}(\lambda) - \phi_{ds}(\lambda) \ , \tag{3.4}$$

using measurements obtained by directing the excitation source onto the sample mounted in the center of the integrating sphere.

In (3.4), Φ_{fs} is the photon flux observed when a blank piece of fused silica is placed in the excitation beam path within the sphere, and Φ_{ds} is the photon flux observed when a fused silica sample containing down-shifters, such as Si-NCs, was placed in the excitation beam path within the sphere. Their difference determines the down-shifter absorption rate, $\Phi_{absorbed_ds}$.

In order to calculate the IQE of the converter, the absorption of the fused silica host containing the down-shifters was calculated as

$$\phi_{absorbed_converter}(\lambda) = \phi_{incident}(\lambda) - \phi_{ds}(\lambda) \, . \tag{3.5}$$

3.7.3 Step-by-step directions for a quantum efficiency measurement

The following provides a useful guide to performing QE measurements on a Si-NC containing sample:

1) Set-up the integrating sphere so that the laser beam is directed into the sphere and onto the sample. Ensure that the laser beam is hitting the sample by placing a reflective sample in the sphere (even fused silica will work). Gently rotate the sample-holder clockwise and counter-clockwise in the beam path. If the laser is directed onto the sample, then the reflected beam should be observed exiting the sphere through the input port as the sample is rotated off-normal.

2) The output port of the sphere must be connected to the Ocean Optics Spectrometer CCD using the SMA-port adapter on the sphere, and the SMA-ended fibre-optic cable.

3) The CCD must also be connected to a computer via a USB cable. The computer must have the SpectraSuite software installed on it before the CCD is connected to the computer.

4) Open the SpectraSuite program. The default display is arbitrary units ("Counts") versus photon wavelength (nm). Set the desired integration time and averaging. For absorption measurements where the laser beam was not filtered, a short integration time was required (200 ms – 500 ms) – otherwise the detector would become saturated.

5) Start an absolute irradiance measurement by selecting the "I". When prompted, indicate that the active acquisition is to be used, and select the calibration file from a pre-defined location (if it looks like it is missing, be sure to display "all files"). Enter the appropriate optical fibre diameter. WAIT for the CCD to register a dark spectrum, and proceed only once the software indicates that you may do so.

6) Wait for the absolute irradiance display to appear.

7) For an IQE measurement of Si-NC in fused silica, first place a piece of fused silica in the sample holder and be sure that the reflected laser light is still contained in the sphere. Save the absolute irradiance spectrum as a Tab Delimited file. Then replace the fused silica with a Si-NC sample, and take a similar reading (the displayed spectra will look almost identical to the quartz spectra you just measured). Note that the magnitude of the laser line is dependent on the orientation (rotation) of the sample holder, and also on whether the laser beam is interacting with the sample-holder. Try to be consistent.

8) Exit the absolute irradiance display, and place a filter to prevent the laser line from exiting the sphere. Re-set the correct integration time for the PL acquisition. For Si-NC PL measurements, a long integration time was required (60 s). For cerium

quantum efficiency PL measurements, a medium-integration time was used (20 s). Start a new absolute irradiance acquisition (see steps 5 and 6).

9) Be sure that the sample holder is still oriented in the same direction as the previous two measurements. Wait for SpectraSuite to register one complete reading with the sample in a fixed orientation. Save the absolute irradiance spectrum as a Tab Delimited file.

10) Convert the three spectra (absorption of quartz, absorption of Si-NC, and PL of Si-NCs) to photons flux per wavelength. Integrate the two laser lines and subtract the Si-NC from the quartz to determine the absorption of the Si-NCs. Integrate the PL peak to determine the number of emitted photons (smooth this curve first if required). Calculate the IQE of the Si-NCs by dividing the number of emitted photons by the number of absorbed photons.

3.7.4 Data smoothing

The signal was "noisy" at wavelengths approaching the bandgap, which was the case for the emission of PL from Si-NCs obtained from the integrating sphere. The PL needed to be smoothed before integration; required by the quantum efficiency calculations. The signal was first averaged, and then edited to remove outlying points; this manual data manipulation considered the shape of the PL signal from the normal PL set-up. A typical result is shown in Figure 3.8.

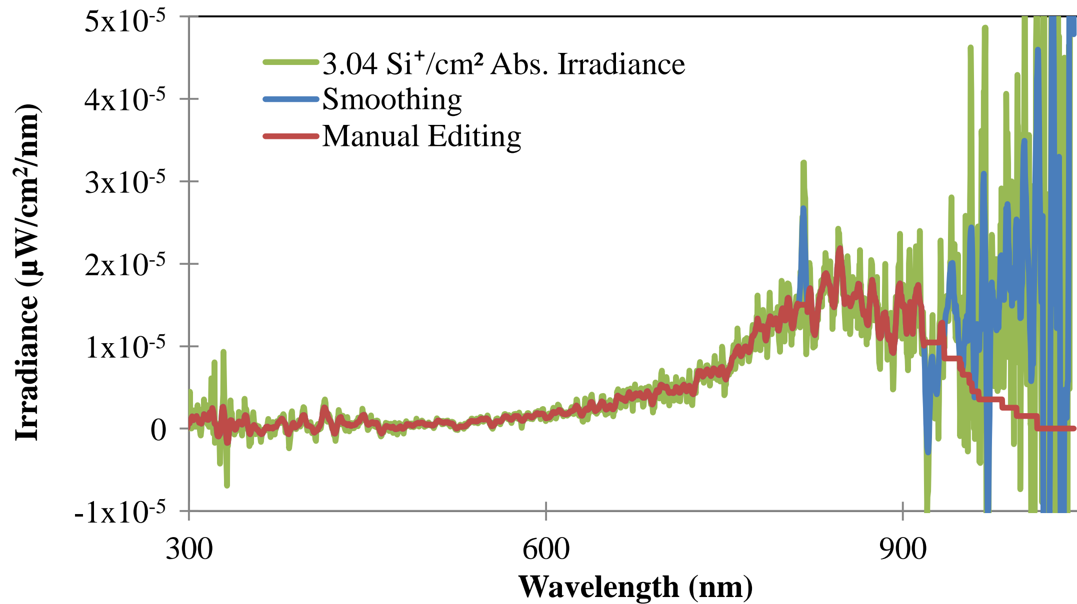

Figure 3.8: Data manipulation of the Si-NC PL obtained from the integrating sphere. The response (in green) was first averaged (blue), and then corrected by hand (red) to resemble the PL curve obtained from the normal PL measurement set-up.

3.7.5 Representative data collected for quantum efficiency measurements

The following sequence of figures shows the data collected to determine the quantum efficiency of a cerium-doped fused silica sample. The sample was implanted with $3x10^{15}$ Ce/cm^2 at 25 keV. Figure 3.9 shows the laser line in the sphere directed onto a piece of fused silica, and also shows the laser line in the sphere directed onto a piece of cerium-implanted fused silica. After correcting each data set for the sphere response, the number of photons contained in the integration of the latter was subtracted from the number of photons contained in the integration of the former to obtain the number of photons absorbed by the implanted cerium.

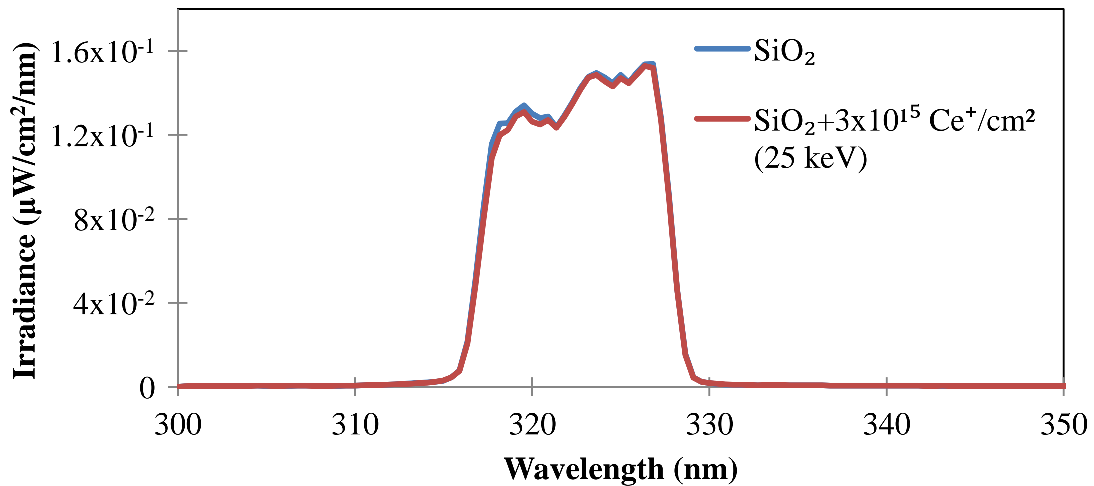

Figure 3.9: The 325 nm HeCd laser line measured through the sphere, with a piece of fused silica in the laser path, and then a piece of cerium-implanted fused silica in the laser path. The subtraction of the latter from the former gives the absorption of cerium.

Figure 3.10 shows how a typical cerium-PL spectrum is modified by the sphere response. Note that the response increases by approximately three orders of magnitude.

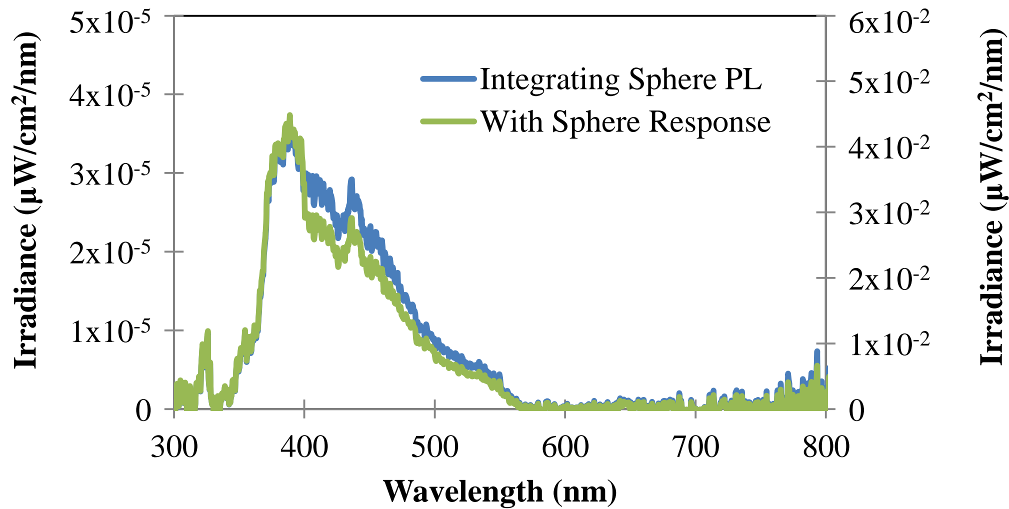

Figure 3.10: Comparison of the PL profile obtained from the sphere (blue) and corrected for the sphere response (green). Note that the magnitude of the response increases by three orders when the sphere response is taken into account.

3.8 Ellipsometry

A second technique used to characterize the fabricated Si-NC samples was variable angle spectroscopic ellipsometry (VASE). Ellipsometry measures the change in light polarization after the light passes through a material. The generated data of *Psi* and *Epsilon* can be used to model the real and imaginary components of the refractive index as a function of photon wavelength, which in turn can be used to determine the relative absorption and composition of a film. There are a number of good resources which explain the subject in some depth [60-61]. VASE is often used in the microelectronics industry to determine the thickness and quality of thin-film coatings, deposited, for example, as optical windows or even electrical contacts on semiconductors, both in the research and development phase, and in quality control.

VASE measurement uses broadband light, directed at the sample from multiple angles, to generate enough data to support an iterative modelling process which can be used to determine the real and imaginary components of the refractive index (n and k, respectively), and film thickness of thin films (including those modified by ion implantation). A challenge for the current study is that ion implanted "films" are not distinct; rather, they are graded profiles within the host material. This presents complexities during the modelling of these implanted samples [62-63]. However, it is possible to obtain a first approximation to the refractive index by simplifying the implanted profile as a single-layer film.

The equipment used to characterize the samples was a J.A. Woollam variable-angle spectroscopic ellipsometer. Modelling of Si-NC films on fused silica substrates was performed by first obtaining the parameters for unimplanted fused silica. These were held constant, while the silicon-implanted "film" was modelled. A screen-shot of the modelled fused silica is shown below in Figure 3.11. There is good agreement between the measured data and the model.

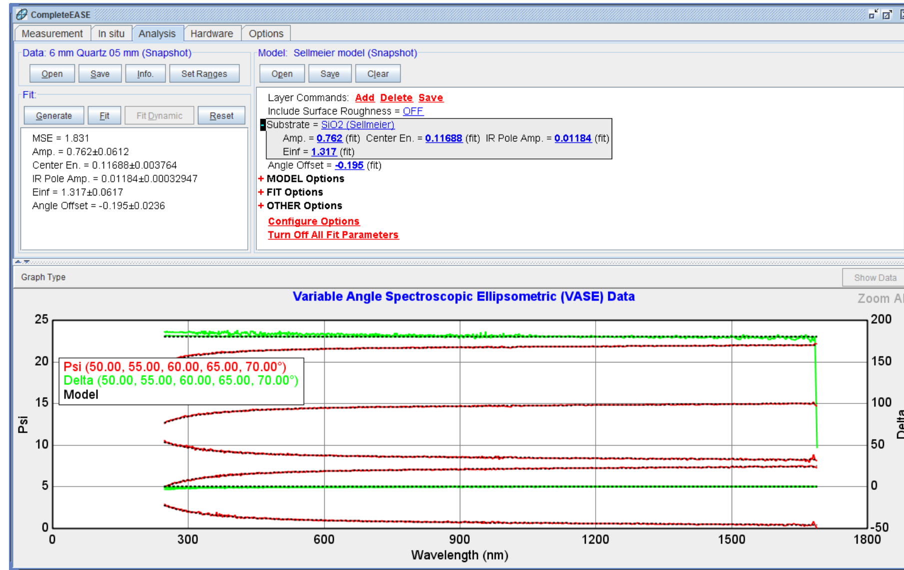

Figure 3.11: Screen-shot of fused silica modelled as SiO_2 to obtain the modelling parameters for the fused silica.

The Si-NC sample was then measured and modeled as a largely transparent (Cauchy) layer on fused silica. The results of the modelling are shown in Figure 3.12.

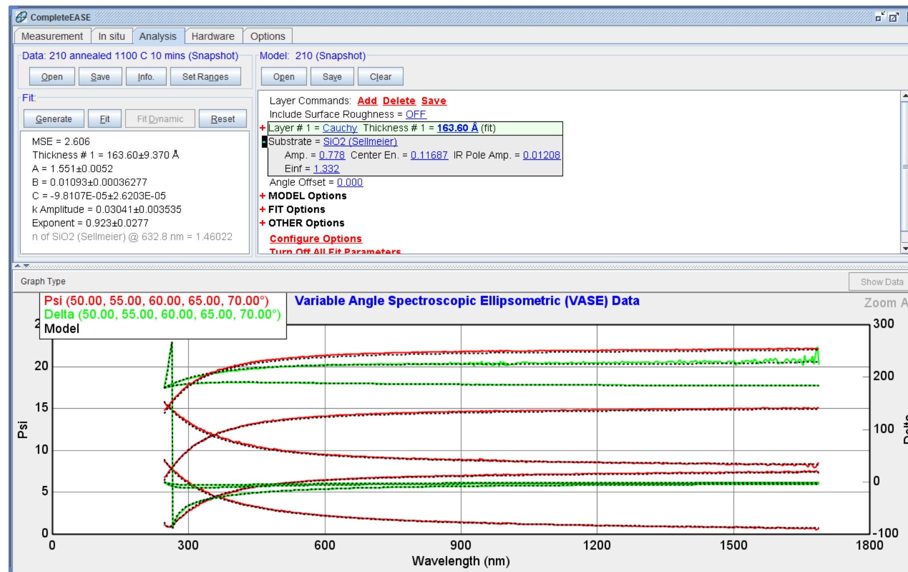

Figure 3.12: Si-NC sample modelled as a transparent layer on SiO_2. The mean squared error (MSE) value is 2.606, which is considered low, indicating good agreement between the data and the model.

3.9 Chapter summary

This chapter introduced the material considerations given to the fabrication of three different types of down-shifters. All samples were fabricated using ion implantation, and the operation of this piece of equipment was mentioned in some detail. High temperature rapid thermal processing, dicing, and sample cleaning procedures were also specified.

Silicon was implanted into fused silica to create Si-NCs, in anticipation of quantum efficiency measurements requiring transparent hosts. Oxygen was implanted into a single-crystal silicon wafer to try to create Si-NCs using a different approach.

Erbium was implanted into four Si-NC samples to study the effect of Si-NC size on energy transfer from Si-NCs to erbium.

Cerium and oxygen was added to LPCVD Si_3N_4 to study the effect of oxygen on cerium PL . A cerium-doped down-shifter in fused silica was also created to enable quantum efficiency measurements of cerium.

Two sample characterization techniques were listed. The main characterization technique was PL, and in particular, quantum efficiency measurements of PL. A second characterization technique was VASE. The sample characterization results can be found in Chapter 4.

Chapter 4

Results and Discussion

4.1 Silicon nanocrystals in fused silica

The photoluminescence (PL) from two representative silicon nanocrystal (Si-NC) samples was measured using the 405 nm laser and the calibrated PL measurement set-up and is plotted in Figure 4.1. One sample was implanted with a fluence of $2.10\text{x}10^{16}$ Si^+/cm^2 (blue curve) and it showed PL peaking at about 770 nm. The other sample was implanted with a fluence of $3.04\text{x}10^{16}$ Si^+/cm^2 (red curve) and it showed higher PL peaking at about 830 nm. This correspondence between red-shifting Si-NC PL and increasing implanted silicon fluence is in good agreement with reference [18].

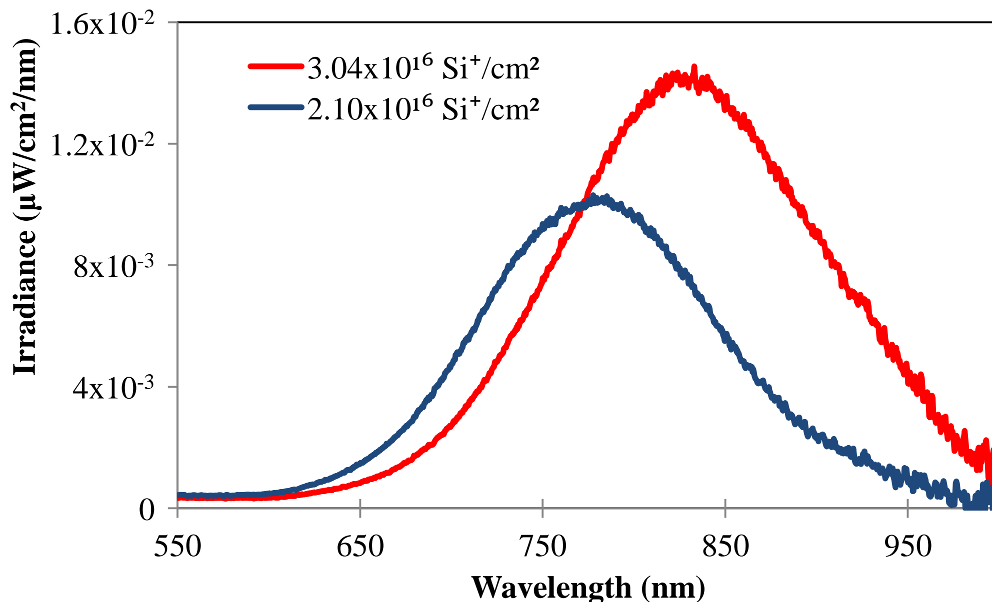

Figure 4.1: PL from two silicon-implanted Si-NC samples. The peak wavelength of the sample implanted with the higher-fluence ($3.04\text{x}10^{16}$ Si^+/cm^2) is red-shifted compared with the peak wavelength of the sample implanted with the higher silicon fluence.

Through comparison of the peak wavelength with the work of Timoshenko *et al.* [25] plotted in Figure 2.1, which correlates Si-NC size with peak PL photon energy (wavelength), an estimation of the size of the Si-NCs in the two samples is possible. The Si-NCs created from the lower silicon fluence have an estimated average size of 2.5 nm, and the Si-NC created from the higher silicon fluence have an estimated average size of 3 nm.

The two Si-NC samples were further analyzed using variable angle spectroscopic ellipsometry (VASE). The determined dispersion curves are shown in Figure 4.2. The results show that the real component of the refractive index falls between the refractive index for fused silica (1.46 at 632 nm) and for silicon (~3.7 at 632 nm). Furthermore, the refractive index is higher for the sample with the greater implanted silicon fluence. Likewise, the extinction coefficient (related to the imaginary component of the refractive index "*k*") also increases with increasing silicon fluence.

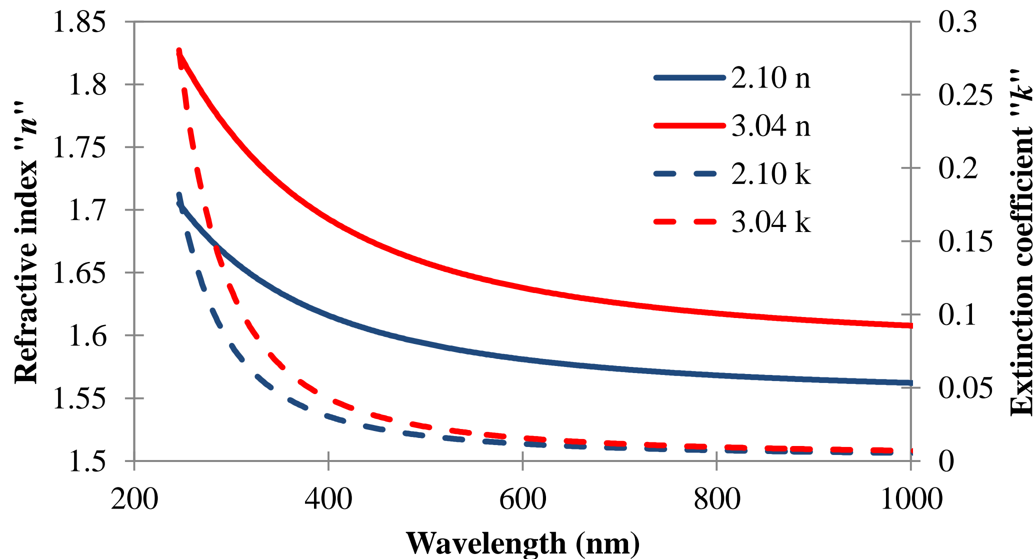

Figure 4.2: Real (*n*) and imaginary (*k*) components of the refractive index from Si-NC samples plotted versus photon wavelength, measured using VASE. The sample with higher silicon content (3.04×10^{16} Si/cm^2) has a higher real index of refraction, and a greater extinction coefficient (k) than the sample with lower silicon content (2.10×10^{16} Si$^+$/cm^2).

The results from VASE modeling indicated that the thickness of the Si-NC region was between 163 Å and 305 Å, for the lower and higher implanted silicon fluence, respectively (see figure Figure 3.12 which shows the 163 Å result). It is at first glance surprising that the VASE results indicate almost twice as thick a Si-NC layer for the higher implanted silicon fluence. However, as shown in section 4.2, too little additional silicon does not result in the formation of Si-NCs, and from SRIM simulations it is also known that the implanted silicon profile is Gaussian. As the implanted fluence increases, the region with enough silicon concentration to form Si-NCs increases in depth.

If this VASE modeled thickness is compared with the Si-implanted fluence predicted by SRIM, which indicates a peak penetration depth of about 236 Å, with 95 Å straggle, then it appears that the Si-NC depth is over-estimated, particularly for the lower fluence. However, previous research indicates that the location of Si-NC formation correlates with the location of the formation of ion implantation induced vacancies [64]. Most of the vacancies are located within the first 200 Å (Figure 4.3), so this interpretation better supports the results obtained at lower silicon implantation fluence.

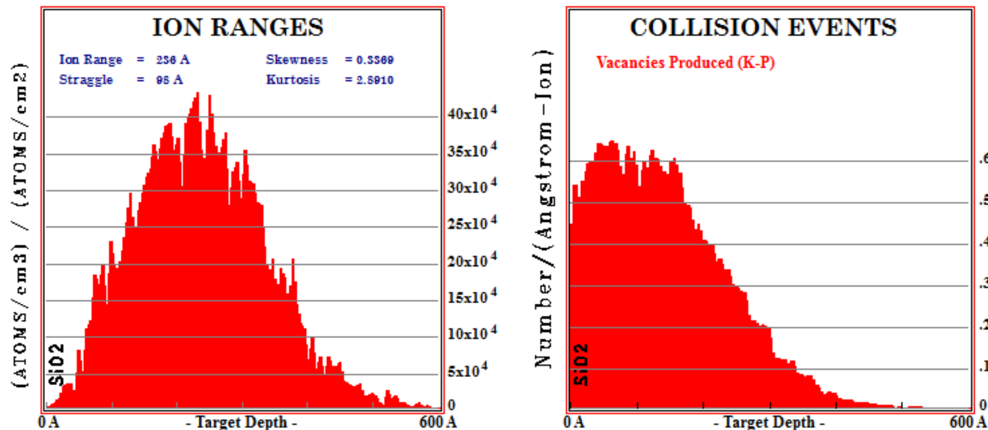

Figure 4.3: SRIM output from Si^+ (15 keV) implantated into SiO_2 at 7 degrees, showing the resulting distribution of silicon ions and vacancies.

Transmission measurements were performed as a confirmation of the wavelength-dependent light transmission through the samples; i.e. that such transmission inversely corresponded to the wavelength-dependent extinction coefficient. Figure 4.4 displays the results, which show significantly decreased transmission below 400 nm. This matches well with the extinction coefficient increase below 400 nm, shown in Figure 4.2. In addition, the transmission is lower for the sample with the higher implanted silicon fluence, which also corresponds to the increased extinction coefficient for that sample.

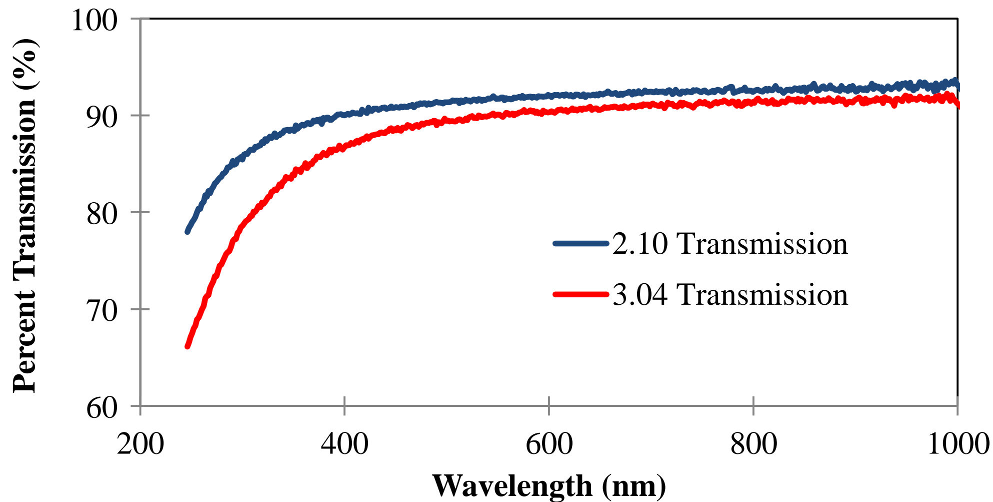

Figure 4.4: Light transmission through fused silica samples containing Si-NCs (implanted with 2.10×10^{16} Si^{+}/cm^{2} and with 3.04×10^{16} Si^{+}/cm^{2}). The sample with the higher implanted silicon fluence yields less light transmission.

4.2 Silicon fluence-dependent Si-NC creation

The range of fluence corresponding to Si-NC creation was investigated for an implantation energy of 15 keV. This work was completed early in the project, and the samples were analyzed using the uncalibrated PL set-up (before access to the LS-CAL lamp was obtained). The PL shape is therefore not typically Gaussian, and the peaks are slightly blue-shifted compared with the calibrated results shown in section 3.1; however the trend obtained from these results is valid and worth discussion.

The implanted fluences ranged from $1.35x10^{16}$ Si^{+}/cm^{2} to $3.54x10^{16}$ Si^{+}/cm^{2}. All samples were annealed at about the same temperature (1085 °C or 1090 °C). The lowest fluence did not yield any Si-NC PL. As the silicon fluence was increased, PL emerged and increased, gradually red-shifted, and then decreased (see Figure 4.5).

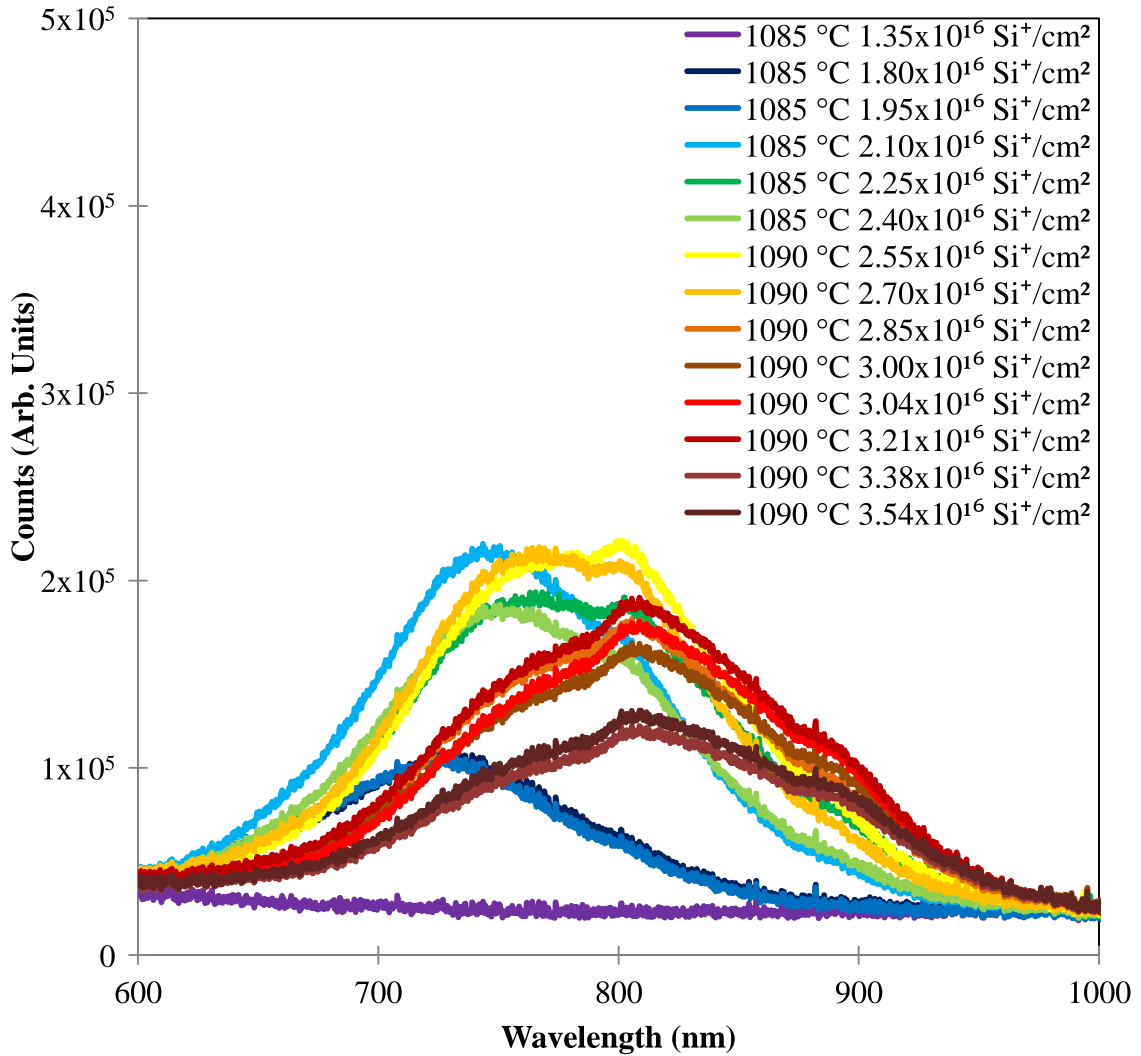

Figure 4.5: PL from a range of silicon fluences implanted into fused silica at 15 keV, annealed at approximately the same temperature, and excited with a 405 nm laser beam. Note the trend from no PL, to blue-shifted PL, to peak intensity PL, to red-shifted PL.

Some important conclusions can be drawn from these early measurements:

1) There is a clear relationship between the fluence of implanted silicon, and the peak of the photoluminescence from the nanocrystals, even for very slight changes in the silicon fluence;

2) The peak ranged from ~700 nm to ~ 850 nm, while the full-width-half-maximum (FWHM) of the nanocrystal PL was approximately 200 nm;

3) It is also important to note that there is a silicon fluence window for creating silicon nanocrystals; too little silicon will result in no silicon nanocrystal PL, and the intensity of the PL eventually drops off with increasing silicon fluence.

4.3 Photoluminescence from oxygen-implanted silicon

Very little literature was found on the fabrication of Si-NCs using the implantation of oxygen into silicon to create an oxygen-rich (silicon-poor) region in the silicon. One paper assumed that Si-NCs were created after a "separation by implantation of oxygen" (SIMOX) procedure, based on the similarities between the PL yield and PL obtained from silicon nanocrystals formed in quartz [65]. The oxygen in that paper (O_2^+) was implanted at 200 keV; no discussion of PL resulting from a low-energy oxygen implantation into silicon, such as the implantation described here, was found in the literature.

Using the SRIM simulation software, the fluence of oxygen required to achieve the same atomic concentration of silicon/oxygen for Si-NC formation was calculated, and the corresponding oxygen fluence was implanted into *p*-type <1-0-0> silicon. The sample was processed as if it were a silicon-implanted fused silica sample. The resulting photoluminescence was characteristic of Si-NCs (see Figure 4.6). Note that the photoluminescence for both samples was measured using the uncalibrated PL set-up, which is why the PL profile is, once again, not Gaussian.

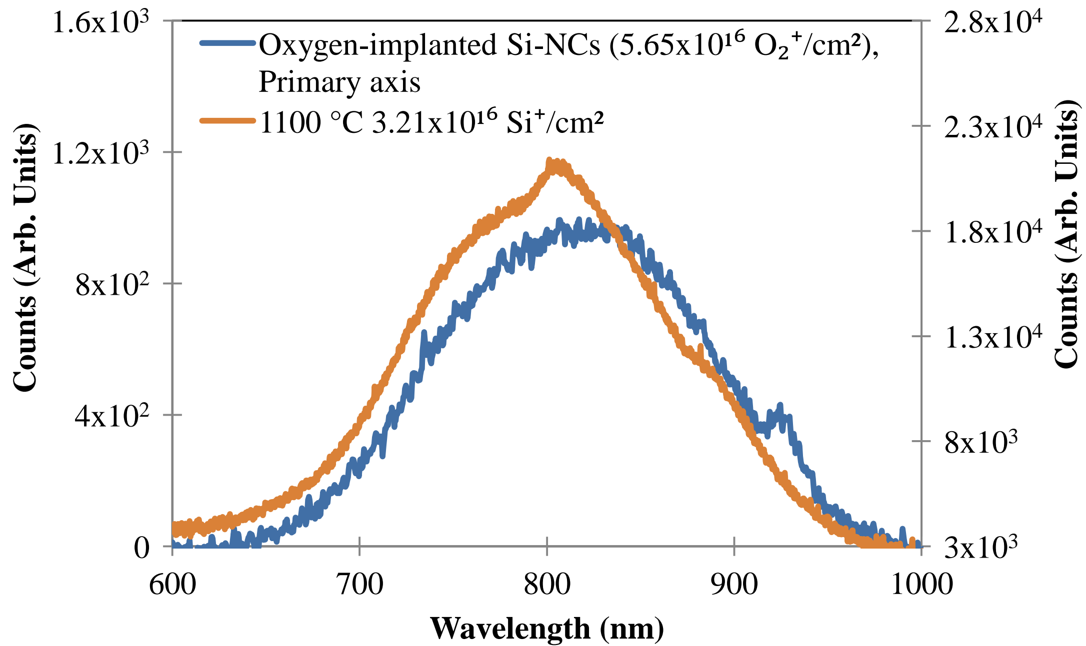

Figure 4.6: PL from oxygen-implanted into silicon (blue, primary axis), compared with typical silicon-implanted Si-NC PL in fused silica quartz (orange, secondary axis). Both samples were annealed at 1100 °C and both were excited by a 405 nm 16 mW laser.

The SRIM simulation indicated that silicon-rich regions were expected on either side of the Si-NC region (see Appendix Figure B-3). This was verified by iterative VASE modelling, and the model which produced the best results contained a thin layer of silicon at the surface (10 Å), followed by a largely transparent "Cauchy" region (with optical constants that were similar to the Si-NC fused silica optical constants: 513 Å), followed by a silicon substrate. The optical constants from the Cauchy region are shown Figure 4.7. This silicon/silicon-poor/silicon sandwich structure was further confirmed by submerging the oxygen-implanted sample in 10:1 hydrofluoric acid for 20 seconds, which would have removed a surface oxide, with the sample still producing PL.

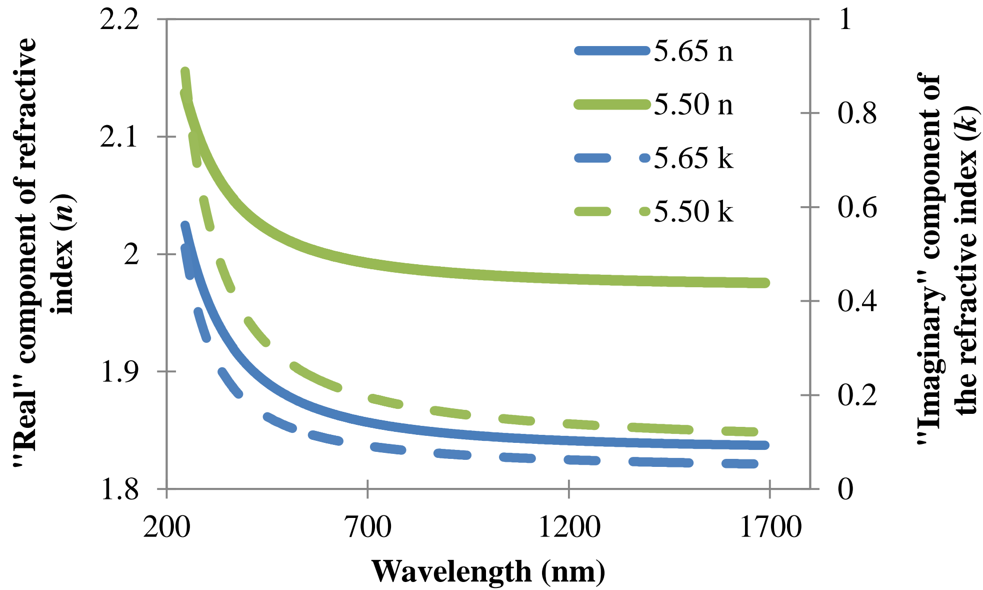

Figure 4.7: Refractive indices for two oxygen-implanted silicon samples. The samples were modeled as a three-layer with a thin (10 Å) silicon top-layer, followed by a larger (513 Å), transparent region (Cauchy layer) which could contain Si-NCs or amorphous SiO_2 particles, and a silicon substrate.

The refractive indices that were obtained by VASE modeling are convincing in their shape, and their magnitude, which falls in a similar region to refractive indices obtained for Si-NC in fused silica. The indices shown in Figure 4.7 are slightly higher than those shown in Figure 4.2, which indicated a more silicon-rich region than either of the two Si-NC in fused silica samples that were investigated. Furthermore, the oxygen-poor sample ($5.50x10^{16}$ O_2^+/cm^2) showed a higher refractive index than the marginally oxygen-rich sample ($5.65x10^{16}$ O_2^+/cm^2). This correlates with the relative peak wavelengths of the PL signal given by the two samples, shown in Figure 4.8, where the oxygen-rich sample yields slightly blue-shifted PL.

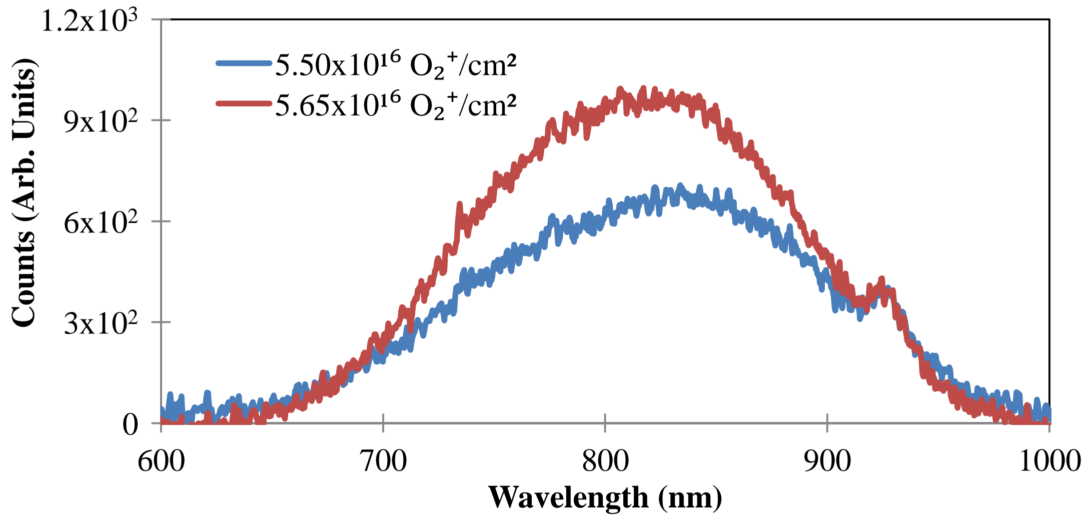

Figure 4.8: PL from oxygen implantation (405 nm excitation). Note that the slightly oxygen-rich sample has slightly blue-shifted PL.

Another interesting result from the VASE simulations is that the transparent (Cauchy) region was calculated to be 513 Å in depth. Comparing that number with the depth profile of the implanted oxygen in silicon (Appendix Figure B-3), it is clear that at least 90% of the implanted oxygen is indeed contained in that region. There is some transmission electron microscopy evidence which suggests that the implanted oxygen results in "the presence of small amorphous oxide precipitates which increase in size toward the buried (oxide) layer," and after high-temperature annealing (1320 °C), the oxygen has diffused to become a buried oxide region containing silicon islands which appear to be hundreds of nanometers in length [66]. It is not clear whether the samples created for this thesis were annealed at high-enough temperature to form the silicon islands in fused silica, or whether small oxide precipitates were in fact present in the sample, or perhaps both entities were present. Given the evidence of PL from SiO_2 particles presented in Chapter 2, as well as evidence of PL from Si-NC particles, further studies would be useful to determine the source of the PL from these samples.

Whatever the source of the photoluminescence, note that the intensity of the photoluminescence shown in Figure 4.6 is much lower than that corresponding to Si-NC in fused silica, probably due to a number of reasons:

1) the 405 nm exciting laser light is more likely to be absorbed by the silicon-rich region above the oxygen-rich region, reducing the incident intensity of the laser that reaches the oxygen-rich region;

2) the emitted photoluminescence is more likely to be absorbed by the silicon-rich region above the nanocrystal region, reducing the apparent emitted PL intensity; and

3) the oxygen fluence was not optimized for emission intensity, and from the study shown in section 4.2 it appears that the emission intensity does depend on the silicon/oxygen atomic percentage. The relative intensity of the PL signals shown in Figure 4.8, where the oxygen-rich sample (5.65×10^{16} O_2^+/cm^2) yields stronger PL, supports this hypothesis.

4.3.1 Electrical contacting of oxygen-implanted samples

The likelihood of silicon-rich regions on either side of a photoluminescent region provided the motivation for attempting to electrically-contact the photolumienscent region. Note that it is difficult to electrically contact Si-NCs when they are fabricated in silicon-implanted fused silica, due to the high bandgap of fused silica ~ 8.9 eV [67]. A preliminary investigation of the oxygen-implanted samples involving sputtered aluminum contacts on both front and rear surfaces of the sample showed that charge can indeed be passed through the oxide region (see Figure 4.9). The processing involved a 20 second dip in 10:1 HF to remove the native oxide, and it is noteworthy that the O-implanted surface still showed PL after the dip (indicating that it is not just an oxide region – which would have been washed away by the HF). Electroluminescence was not observed.

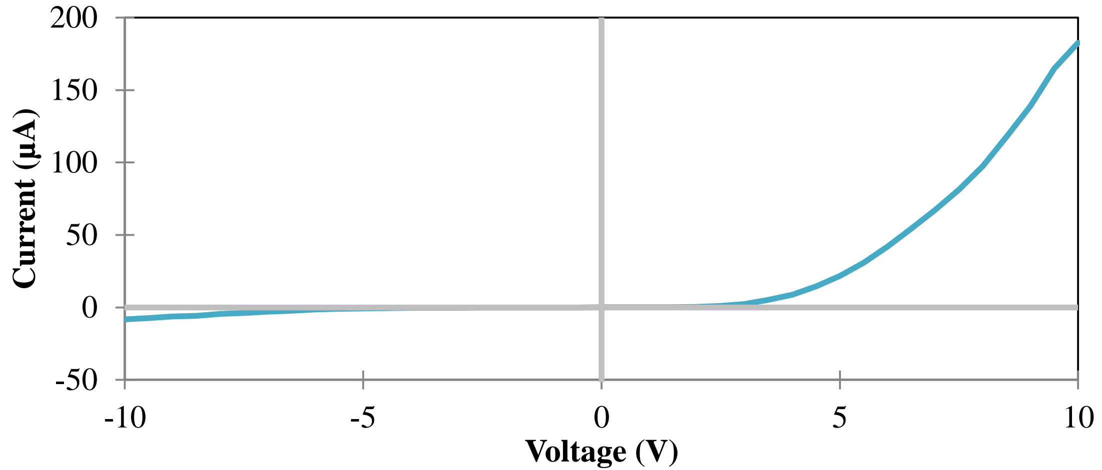

Figure 4.9. The electrical curve from Al-Al contacted O-implanted (5.50x10^{16} O_2^+/cm^2) silicon. It is clear that the device does pass current.

These results indicate that a down-shifting layer could be implanted directly into the surface of a photovoltaic cell, provided that a sufficiently high photon conversion efficiency of the PL layer was obtained.

4.4 Quantum efficiency measurement for photoluminescence from silicon nanocrystals in fused silica

The PL absolute quantum efficiency of the two Si-NC samples discussed in section 4.1 was measured using the integrating sphere PL set-up. The results are shown in Table 4.1.

Table 4.1: External and internal quantum efficiencies of the Si-NC samples [68].

Sample	EQE of converter (%)	IQE of converter (%)	IQE of Si-NC (%)
2.10x10^{16} Si$^+$/cm^2	0.014±0.010	0.81±0.60	1.66±0.60
3.04x10^{16} Si$^+$/cm^2	0.020±0.010	0.59±0.60	0.80±0.60

The optical conversion efficiencies obtained are lower than those required to improve SJSPVC performance (these modeled efficiencies were introduced in Chapter 1). However, it is interesting to note that the efficiencies of the two Si-NC samples are similar while there appears to be a positive correlation between EQE and silicon-fluence. Refer to Appendix E for the error calculations of the quantum efficiency measurements.

It is important to consider that Si-NCs emit light in all directions, and this will practically reduce the usable number of photons when the converter is placed on top of a cell. Methods of mitigating directional losses are discussed in [69].

4.5 Erbium-doped silicon nanocrystals in fused silica

Four of the silicon-implanted Si-NC samples were chosen to receive an additional erbium implantation, at a fluence of 2.75×10^{14} Er^+/cm^2 and 35 keV implantation energy. The result of the SRIM simulation of erbium implanted into fused silica at 35 keV and at a seven-degree angle is shown in Appendix Figure B-2. Note that the erbium peak matches that of the silicon-implanted peak for a silicon implantation energy of 15 keV.

The PL for wavelengths >900 nm from these samples was measured at the University of Manchester using 405 nm excitation selected by an excitation spectrometer from a 450 W xenon lamp (commercial Jobyn Yvon - fluorolog system. The PL signals were collected using an integrated emission spectrometer and detected with an N_2-cooled InGaAs array. All measurements were taken at room temperature with an integration time of 10 s. Figure 4.10 shows a typical erbium PL signature that peaks at 1534 nm.

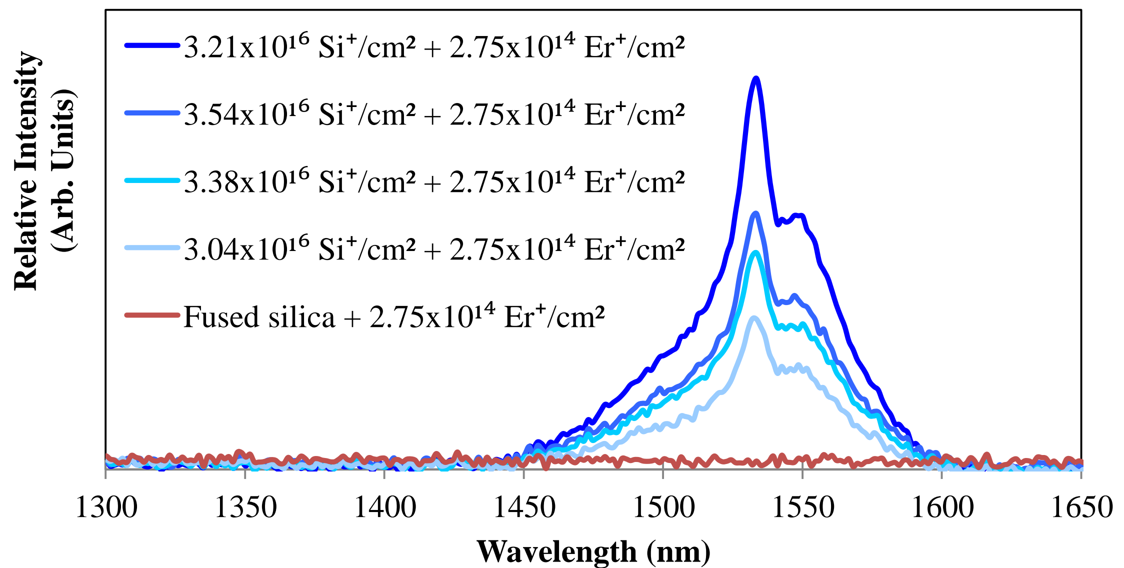

Figure 4.10: Erbium-implanted fused silica samples showed characteristic erbium PL, provided that Si-NCs were present in the sample. This indicated that energy transfer is occurring between the Si-NCs and the erbium ions.

The erbium is not excited directly by 405 nm light when silicon nanocrystals are not present, evident from the "No implanted silicon" sample, indicating that energy transfer is happening between the Si-NCs and the erbium ions. There is some variation in the intensity of the photoluminescence, which in this study does not appear to correspond to the fluence of the implanted silicon, which should have been the only variable.

The corresponding PL from the Si-NC samples before they were implanted with erbium is shown in Figure 4.11. Interestingly, the Si-NC PL was completely quenched after the erbium implantation and the 900 °C anneal.

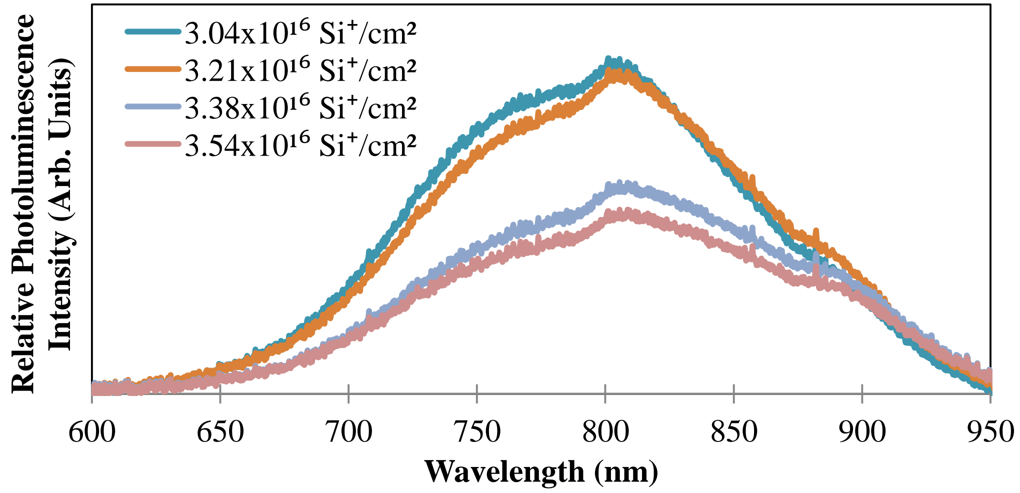

Figure 4.11: PL (405 nm excitation) obtained from Si-NC samples before they were implanted with erbium. Note that the intensities of the PL from the Si-NC appear to have no correlation to the intensity of the erbium emission shown in Figure 4.10.

There is good correlation in the transient lifetime measurements of the erbium PL and the implanted silicon fluence. These results were obtained from collaborators at University College London. A 476 nm diode-pumped solid state laser, modulated at 548 Hz using a *Pockels* cell (resolution ~15 ns), was used to excite the samples. The Er^{3+} PL transients (1534 nm) were collected using a single-grating spectrometer and an infrared-sensitive *Hamamatsu* photomultiplier tube. The time decay rate, $I(t)$, was fitted with a stretched exponential function:

$$I(t) = I_0 e^{(-t/\tau)^\beta}, \tag{4.1}$$

where I_0 is the initial intensity, τ is the carrier lifetime, and β is the non-exponential parameter. β is plotted along with the time decay rate, in Figure 4.12, and the fact that its value remains reasonably constant indicates that τ provides a good indication of the time decay.

With increasing implanted silicon fluence, and therefore presumably also increasing Si-NC size, the time-decay rate decreased. This result contrasts with the

results of Si-NC lifetimes obtained by [70]. However, more recent research [71] suggests that there are "three distinct populations of emitting nanocrystals, with any link between decay time and nanocrystal size being a secondary effect."

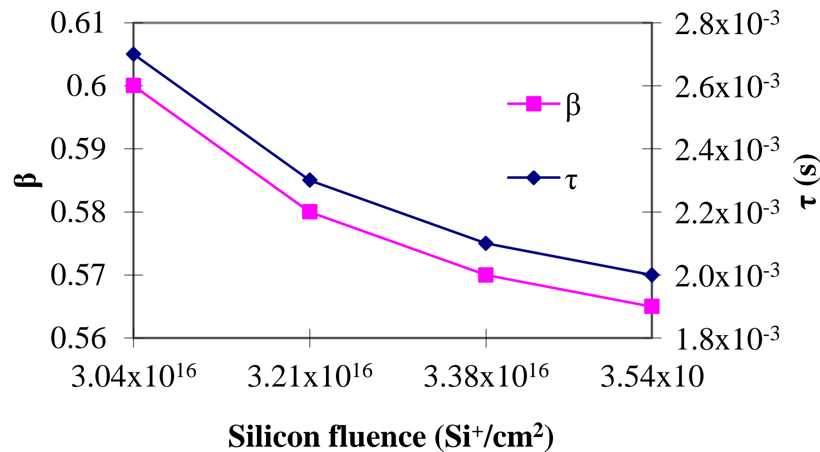

Figure 4.12: Transient PL measured for erbium-doped Si-NC samples. There appears to be a relationship between the implanted Si-fluence (i.e. Si-NC size) and the radiative lifetime of these ensembles.

This result is important for optimizing Si-NC samples for energy transfer and light emission from samples co-doped with rare-earths in particular. The measured lifetime of erbium, at 2 ms, is reasonable considering the findings of others [42], who found that Si-NC-sensitized erbium had a decay time of 3 ms. Another group [72] claim that the erbium lifetime of an Er–Si–O sample is 269 μs, and that the erbium lifetime of an Er-doped SiO_2 sample is 11 ms; the 2 ms lifetimes shown in Figure 4.12 fall somewhere between these extremes, as would perhaps be expected for a fused silica sample with maximum excess concentration of about 30% [53]. It is also important to note that erbium was implanted into silicon-rich fused silica, not SiO_2 as used in the SRIM simulation to determine the peak implantation depth, and the erbium may not have penetrated as far into the heavier (silicon-rich) material as suggested by the SRIM simulation results.

4.6 Cerium-oxygen co-doped dielectric films

This section of the thesis reports on the emission of light from cerium-implanted Si_3N_4 prepared via LPCVD. The presence of implanted oxygen in the films was found to have a governing effect on light emission from these cerium-doped dielectric thin films.

The photoluminescence (PL) from the samples was measured. The samples were excited with a 325 nm HeCd laser operating at a power of 2.5 mW. The PL peaked at ~482 nm, as shown in Figure 4.13.

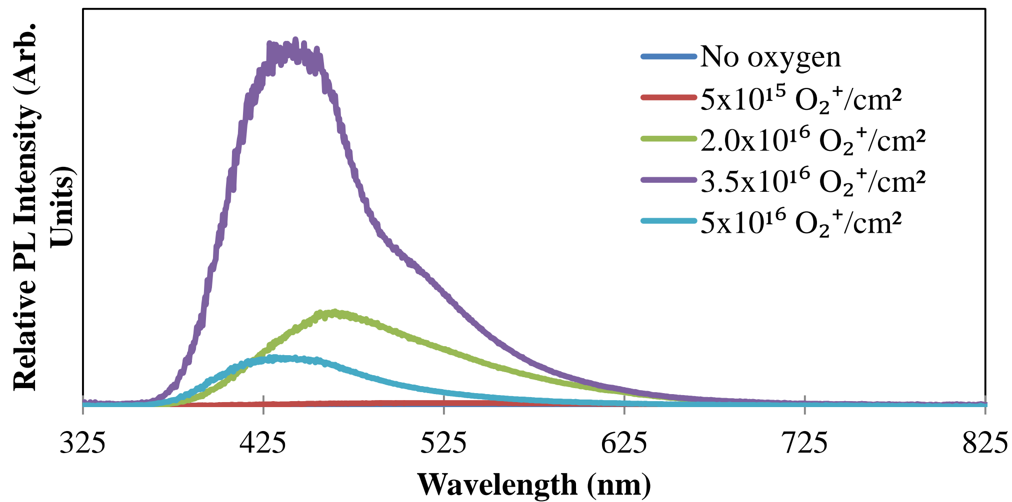

Figure 4.13: Representative PL from a series of thin films of LPCVD Si_3N_4 that were implanted with cerium ($5x10^{15}$ Ce^+/cm^2 at 25 keV) and oxygen (varying fluence).

There was no PL from the ^{140}Ce-only doped LPCVD Si_3N_4 sample, but there was PL from the samples which did receive an O_2^+ implantation. Analyzing the relative peak intensities shows that there is an exponential-type dependence of the PL with implanted oxygen fluence (Figure 4.14). These results support the proposal that cerium PL is dependent on its state of oxygen coordination, as has been suggested by others [73-74].

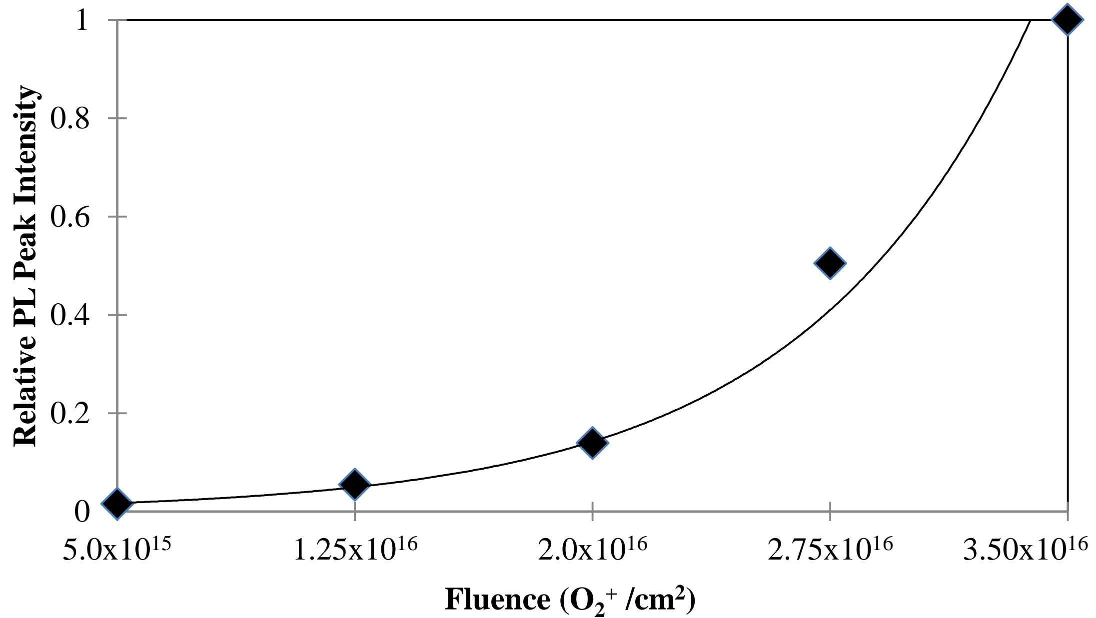

Figure 4.14: Exponential-type dependence of cerium peak PL intensity with varying oxygen content. The line is provided as a guide for the eye.

The effect of cerium fluence on the peak PL was also studied. The following series of figures (Figure 4.15 - 4.17) maintain a constant vertical axis, and show the relative effect of varying cerium fluence with three different oxygen fluences. When the oxygen fluence is low, changes in the cerium fluence do not result in large changes in PL intensity. When the oxygen fluence is optimal, changes in the cerium fluence do result in large changes in the PL intensity (i.e. the optimal oxygen fluence is dependent on the cerium doping). Finally, with an abundance of oxygen, changes in the cerium fluence once again do not result in a large change in the PL intensity – in fact, in this final case, increasing cerium fluence actually yields lower-intensity PL.

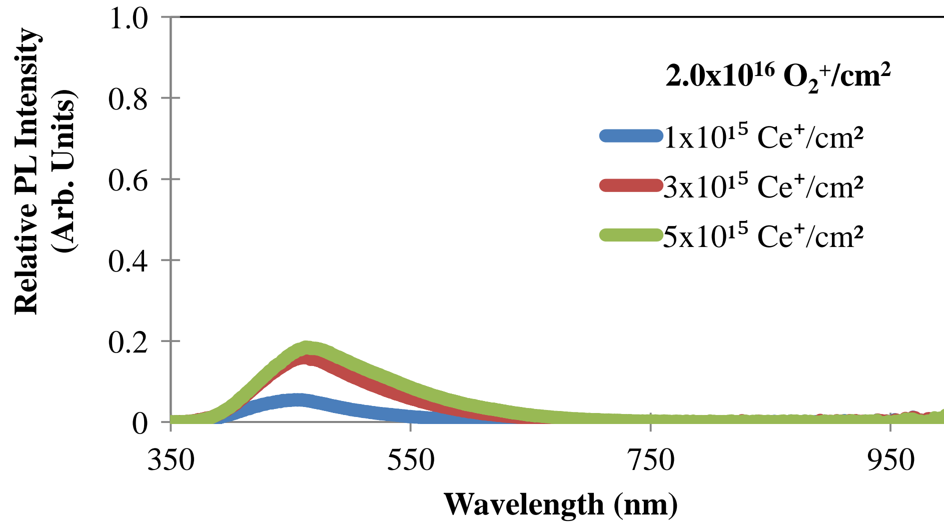

Figure 4.15: Constant oxygen fluence of $2x10^{16}$ O_2^+/cm^2. The PL varies minimally with cerium fluence at this oxygen fluence. Note that more cerium yields more PL.

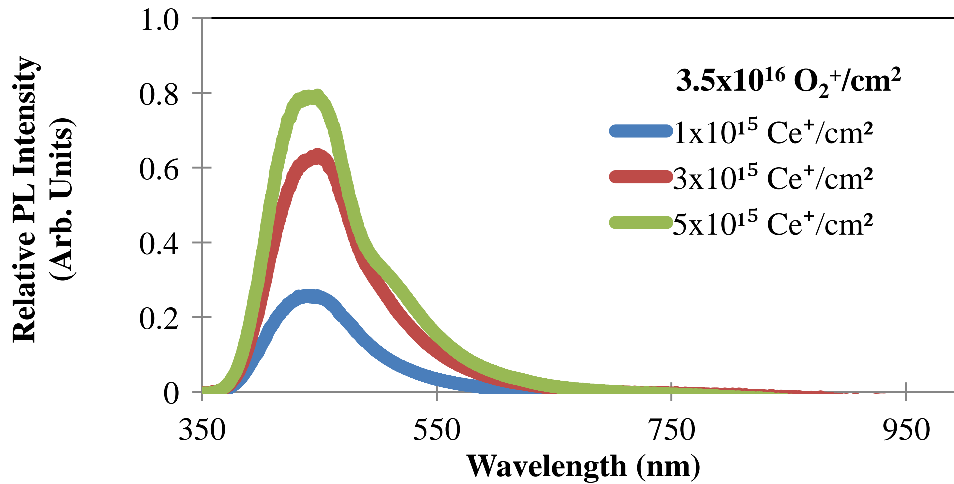

Figure 4.16: Constant oxygen fluence of $3.5x10^{16}$ O_2^+/cm^2. The PL varies significantly with cerium fluence at this oxygen fluence. Note that more cerium yields more PL.

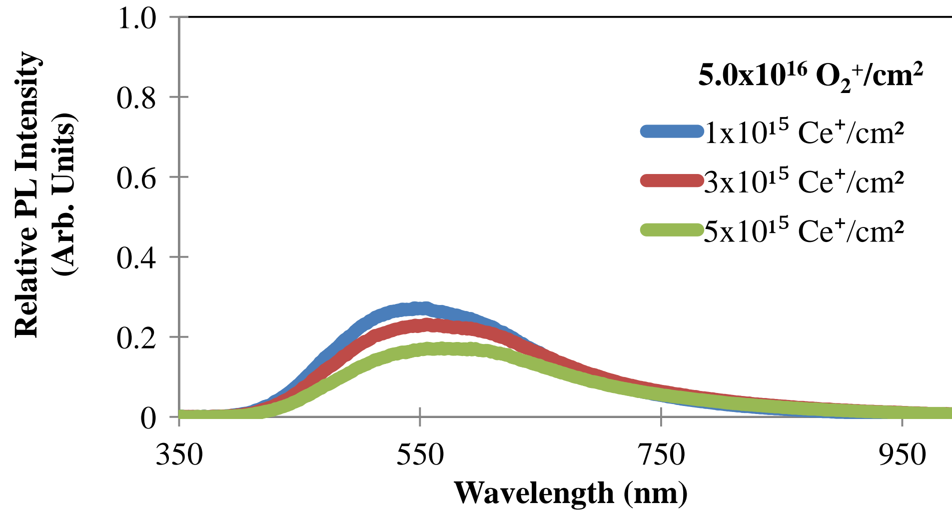

Figure 4.17: Constant oxygen fluence of $5.0x10^{16}$ O_2^+/cm^2. The PL varies minimally once again with cerium fluence. Note that less cerium yields more PL, contrary to the results obtained with lower oxygen fluence.

4.6.1 Rutherford backscattering

The cerium-doped samples were created by first implanting cerium into Si_3N_4 and then implanting oxygen fluences that varied in magnitude between about 10 and 100 times the cerium fluence. There was a possibility that so much oxygen implanted into the samples had sputtered away the previously-implanted cerium. Rutherford backscattering (RBS) was used to determine whether cerium remained in the samples.

RBS was performed at the University of Western Ontario. Helium-4 was directed at the sample at an energy of 2 MeV, and was collected at a 10 degree exit angle. Rutherford backscattering theory and modelling is described in [75] and references therein. The results from three samples are shown in Figure 4.18.

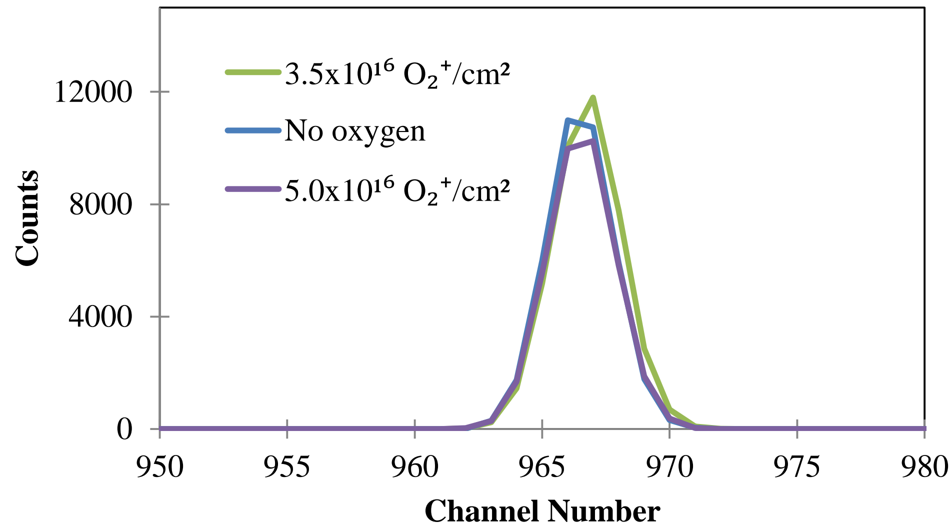

Figure 4.18: Rutherford backscattering results from three samples containing 3x10^{15} Ce^+ implanted into LPCVD Si_3N_4. The variation in the peak magnitude is within experimental error, indicating that the implanted cerium was not sputtered out of the material during the subsequent oxygen implantation.

The results indicate that qualitatively that there is minimal variation in the cerium concentration, suggesting that cerium was not significantly sputtered from the film during the implantation of oxygen.

4.6.2 Electrical conduction of the cerium-doped silicon nitride

A patch of aluminum approximately 0.5 cm^2 in area was sputtered onto the front and rear surface of the cerium/oxygen-doped Si_3N_4 samples, and was annealed for 30 seconds at 400 °C. The electrical conductivity through the 50 nm Si_3N_4 film was probed. The undoped Si_3N_4 sample did not conduct to any significant degree. Figure 4.19 shows the variation in conductivity with doping for all other samples. Those doped with cerium passed tens of microamperes of current, but as the oxygen content was increased, the conductivity decreased. These preliminary results could be useful if cerium was applied as a down-shifter directly to the front surface of a solar cell requiring electrical contacts.

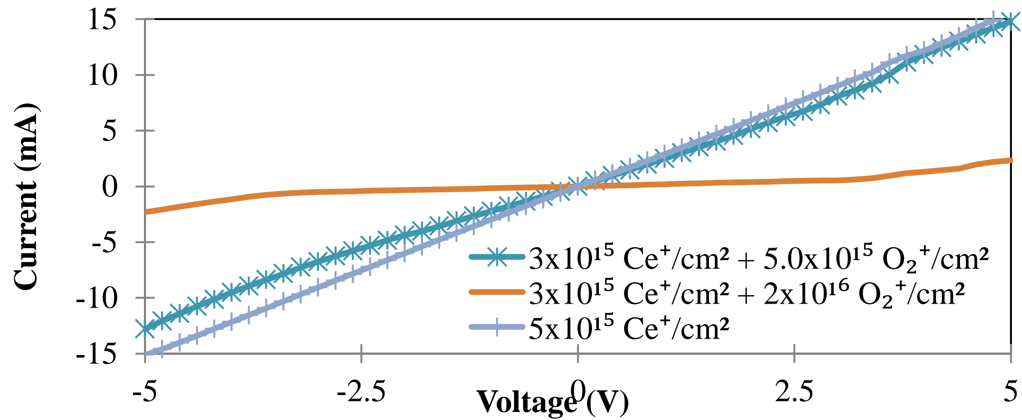

Figure 4.19: Conduction of electrical current through films that contain cerium and oxygen.

4.6.3 Cerium in fused silica

Cerium was also implanted into fused silica to determine how the same cerium fluence would perform in an oxygen-rich environment, compared with the Si_3N_4 environment. The resulting PL from the fused silica sample was considerably lower than Si_3N_4 with the optimal oxygen fluence (see Figure 4.20). Indeed, it is similar to the drop in cerium PL in Si_3N_4 when a surplus of oxygen was implanted.

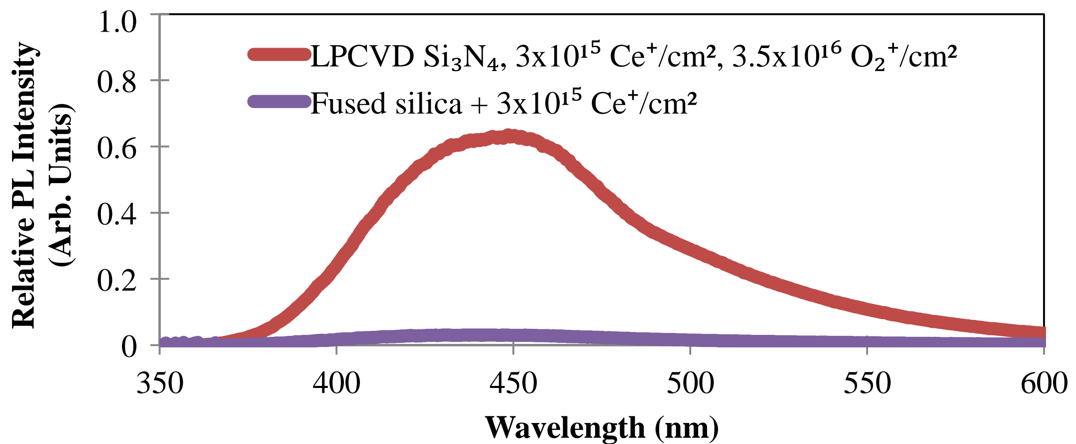

Figure 4.20: Comparison of the PL intensity from $3x10^{15}$ Ce^+/cm^2 implanted in Si_3N_4 with an optimal amount of oxygen also implanted, and cerium implanted in SiO_2. Note that the cerium-doped SiO_2 does not show strong PL, likely due to the high concentration of oxygen in SiO_2.

To further explore the effect of the silicon/oxygen ration on cerium PL, silicon was implanted into a fused silica sample containing implanted cerium. A comparison of the PL from these samples with those prior to silicon implantation showed that the silicon-rich cerium-doped fused silica gave a brighter response than the cerium-only-doped fused silica.

The reason for the low PL with too much oxygen requires further investigation. An alternative approach was to implant cerium into fused silica, and also into fused silica containing enough implanted silicon to form Si-NCs.

It is clear from the series of experiments presented in section 4.6 that cerium by itself does not photoluminesce to any significant degree in LPCVD Si_3N_4, and it was also ascertained that oxygen alone implanted into Si_3N_4 does not photoluminesce, so some interaction between the cerium and the oxygen must be responsible for the relatively strong emission. It could be that the emission is the result of energy captured by the cerium, and transferred to the oxygen, which is kept in an ionized state by its proximity to cerium. The blue emission would be similar to the blue electrical discharge from electrically-excited oxygen. Too much oxygen would decrease the ionization of individual oxygen atoms, and also increase the possibility of non-radiative pathways through further energy transfer amongst the oxygen atoms. Not enough oxygen would mean that cerium had too few opportunities to transfer energy to vacant oxygen atoms. Lifetime studies of the cerium photoluminescence would be useful.

4.6.4 Quantum efficiency measurement of photoluminescence from cerium-doped fused silica

The quantum efficiency of the fused silica sample implanted with cerium was measured using a similar integrating sphere set-up previously used to measure the Si-NCs, but with a 325 nm HeCd pump laser. The SMA-adapted optical fiber was attached to the output port of the sphere, and the input flux was measured with a piece of quartz in

the sphere, and a piece of cerium-implanted quartz in the sphere to determine the absorption of the cerium. The PL emission was measured with a 0.5 inch cyan filter (FD05C – Thorlabs) blocking the laser line in the output port before the optical fiber coupler. The measured PL is shown in Figure 4.21. This data was corrected for both the limited transmission of the cyan filter, and the sphere response.

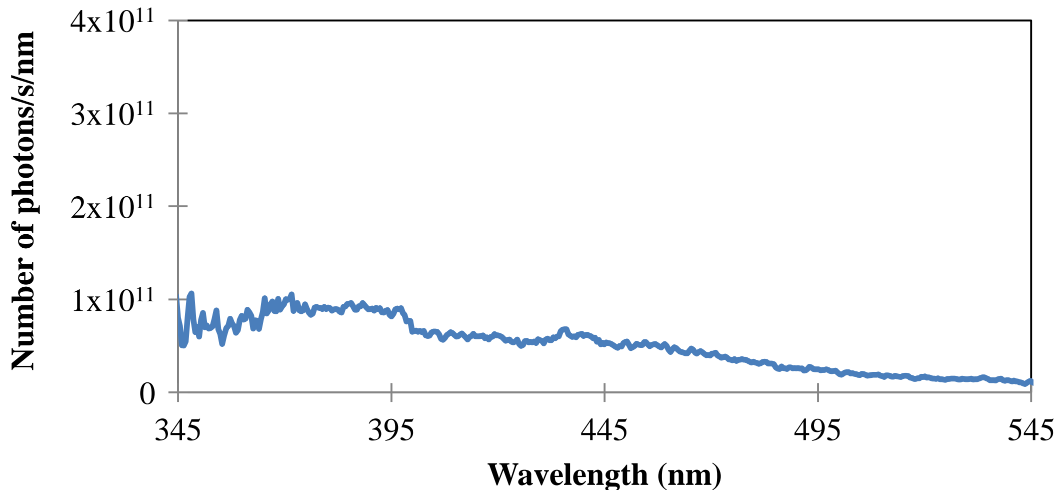

Figure 4.21: Number of photons in the PL from $3x10^{15}$ Ce^{+}/cm^{2} (25 keV) in SiO_2. Measured using the integrating sphere set-up, and corrected for the integrating sphere response and the cyan filter.

The response becomes noisy at wavelengths that are near the transmission edge of the cyan filter (shown in Figure 4.23). These wavelengths were omitted for the IQE calculation, and the PL integration was performed from 355 nm to 575 nm, yielding 20.6% ± 9.9%. However, the PL profile does not match up with the profile viewed using the normal PL set-up, so this efficiency is very much viewed as a first approximation (see Figure 4.22).

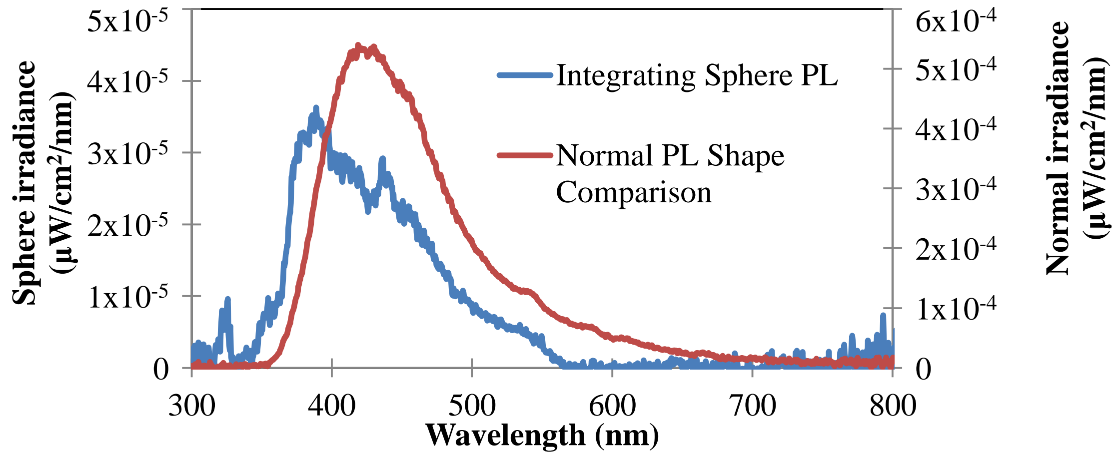

Figure 4.22: Comparison of the PL shape obtained from the cerium-implanted $3x10^{15}$ Ce^{+}/cm^2 (25 keV) fused silica sample in the sphere set-up, and in the normal set-up.

It is not clear why the PL shape obtained from the normal set-up and from the integrating sphere set-up are so different.

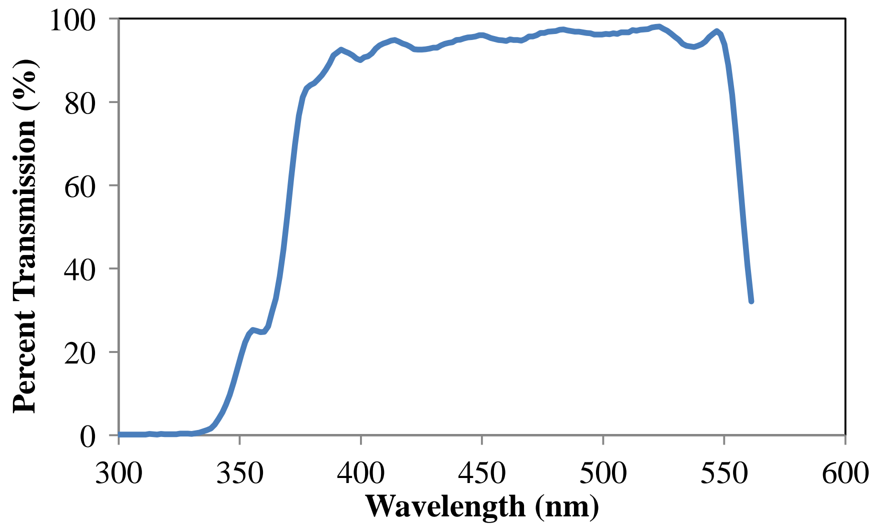

Figure 4.23: Transmission response of cyan filter.

A measurement of the integrating sphere response was performed through counting the number of photons measured in the sphere which was $6.72x10^{15}$, 325 nm

wavelength photons. The calculated laser power required to obtain this number of photons is ~ 3 mW, which is close to the value of 2.5 mW measured using an external power meter.

An interesting calculation is to consider the cerium fluence ($3x10^{15}$ cerium ions/cm^2) and the integrated PL photon flux ($2.24x10^{13}$ photons/cm^2/s) and calculate the photon flux per cerium ion: $7.47x10^{-3}$ photons/cerium ion/second. If the laser beam is approximated as a 2 mm by 2 mm cross-section, then the incoming photon flux per square centimeter is $1.68x10^{17}$, presumably more than enough to excite all the cerium. It is possible that all the cerium is actually being excited, and there are simply too many non-radiative pathways available, possibly due to a surplus of oxygen in the fused silica. It would be interesting to implant higher cerium fluences into fused silica to determine if and how the IQE of the cerium changes as the PL brightness increases.

This result is particularly interesting in light of research into down-shifting materials for application to CdTe PV cells, or other cells which have poor UV light absorption due to a window layer. Klampaftis *et al.* [76] suggest that an organic dye with similar properties to the cerium-doped fused silica sample shown here could improve the performance of CdTe cells (see Figure 4.24).

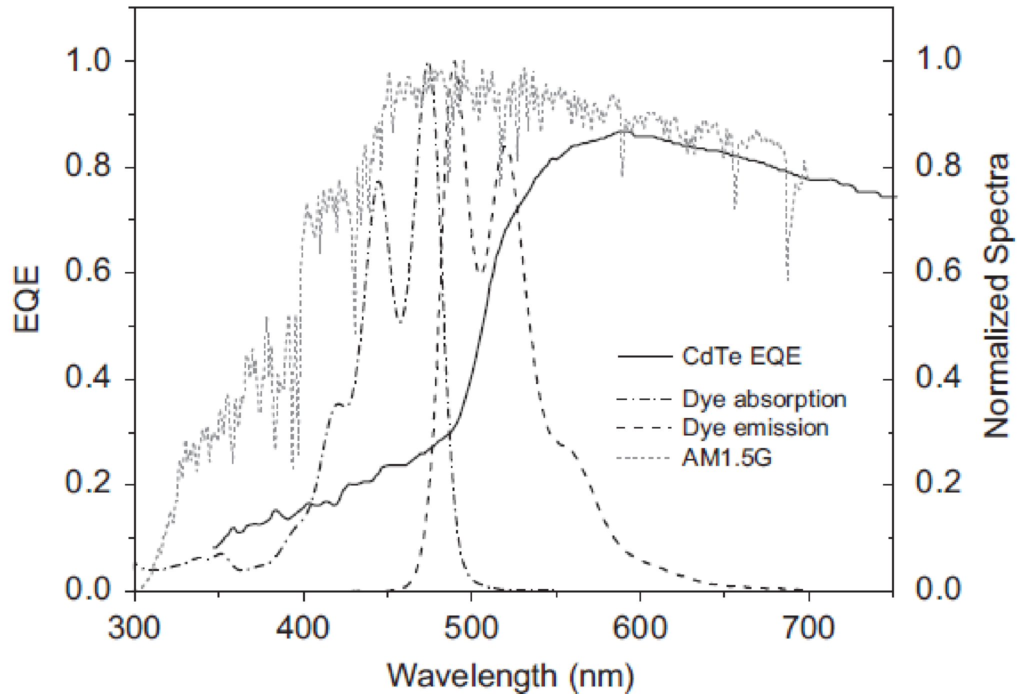

Figure 4.24: The AM1.5 G spectrum super-imposed on a plot showing the down-shifting performance of an organic dye, and the EQE of a CdTe cell. Note that the down-shifting of cerium-doped fused silica could have a similar application. Taken from [76].

4.7 Chapter summary

This chapter presents results obtained from a variety of samples. An IQE of 0.6 – 0.8 % ± 0.53% was obtained for the Si-NC in silicon samples. This result is too low to be useful as a down-shifter for silicon PV cells. In contrast, an IQE of 20.6% ± 2.9% was obtained for a cerium-implanted piece of fused silica. This result could potentially be useful for crossing the CdTe cell window layer to improve the performance of CdTe PV cells, however more research to optimize the cerium concentration in the fused silica, and the modeling of the material's performance as a down-shifter is needed. The oxygen-dependent nature of cerium PL was demonstrated. It is possible to pass electrical current through the cerium-doped Si_3N_4 films provided that the oxygen concentration is low-enough, and the cerium concentration is high-enough.

Energy transfer was demonstrated between Si-NC samples and erbium ions. There is some correlation between Si-NC size and the radiative lifetime of the samples.

It was demonstrated that PL, very similar to that obtained from Si-NCs, can also be created by implanting oxygen into silicon to create an oxygen-rich environment. This oxygen-rich region appears to be sandwiched between two silicon-rich layers. It is possible to pass electrical current through this region, which would be useful if a down-shifting layer is grown directly on a PV cell.

Chapter 5

Conclusions and Future Work

5.1 Summary of the thesis

The light-shifting properties of three types of materials fabricated by ion implantation were investigated, with the goal of engineering the solar spectrum to improve the performance of photovoltaic (PV) cells. The aim of this research was to move ultraviolet (UV) photons in the spectrum from a region of low PV cell external quantum efficiency (EQE) to a region of high EQE, with a "high-enough" conversion efficiency to result in improvement of the cell performance. The down-shifters investigated were silicon nanocrystals (Si-NCs) in fused silica, energy transfer between Si-NCs and erbium, and oxygen- and cerium-doped silicon nitride (Si_3N_4) films. The object was to create a mechanically robust down-shifting material that could also be used as the PV cell encapsulation.

Models of the PL from Si-NC-type down-shifting materials placed above a single-junction silicon photovoltaic cell (SJSPVC) showed theoretical gains in SJSPVC performance when the down-shifting materials conversion efficiency was sufficiently high. The fabricated samples of Si-NCs in fused silica did not yield conversion efficiencies high enough to be useful to SJSPVCs. However, recent findings suggest that a more productive relationship might result from investigations with other PV cells, such as CdTe [77].

The higher conversion efficiency performance of cerium-doped fused silica could yield better down-shifting results. More experimental research and modeling is needed to explore this possibility.

Quantum efficiency characterization of the samples was performed using an integrating sphere measurement set-up and UV-visible electromagnetic radiation. Other photoluminescence (PL) characterization work was carried out with a single-wavelength laser and a collection lens normal to the sample. Variable angle spectroscopic ellipsometry (VASE) was used to measure the optical constants of the implanted films. In additional work, Rutherford backscattering spectrometry, time-dependent PL, infrared-PL measurements, and electrical conductivity measurements were used to characterize select samples.

5.2 Review of results and conclusions

i) Silicon nanocrystals

Silicon nanocrystals fabricated by the implantation of silicon into fused silica were found to have a conversion EQE of about 0.02% ± 0.010%. This is not high enough to perform effectively when used in conjunction with a SJSPVC. It was shown that the peak PL wavelength from Si-NCs shifts with very small changes in the implanted silicon fluence.

It was found that Si-NC-like PL can also be produced by implanting oxygen into silicon. This process has not yet been optimized to obtain strong PL intensity. This method of fabricating a PL layer raises the possibility of creating an internal down-shifting layer just below the surface of a SJSPVC. Electrical current was shown to pass through this oxygen-implanted region.

ii) Energy transfer between Si-NCs and erbium

The transfer of energy between Si-NCs and a rare earth (erbium) was explored with the goal of using the Si-NCs to capture the broad UV solar spectrum, transferring the captured energy to the rare earth, and then releasing the energy at a wavelength fixed by the rare earth. It was shown that, under 405 nm irradiation, erbium does not emit 1534

nm photons, however once Si-NCs are incorporated into the erbium-doped film there is strong 1534 nm emission. The lifetime of the excited states depends on the Si-NC size.

iii) Cerium-dependency on Oxygen for PL

Unlike erbium, cerium has a broad cross-sectional absorption for UV photons. The strong radiative transition peaked between 400 nm and 500 nm, depending on the host material. Cerium- and oxygen-doped Si_3N_4 films were explored using PL. The PL intensity of these films appears to be largely dependent on the level of oxygen in the films. Cerium concentration alone is not an indicator of the strength of the PL, which had previously been suggested by [47]. Select samples were electrically characterized and it was found that cerium-doped Si_3N_4 does pass microamperes of current, but this conductivity appears to decrease with increasing oxygen concentration.

The internal quantum conversion efficiency of one sample of cerium ($3x10^{15}$ Ce^+/cm^2 at 25 keV) implanted into fused silica was found to be close to 20%±9.9%. The implanted cerium fluence was not optimized, and other findings suggest that stronger PL would occur if a higher peak cerium concentration was implanted.

This work with cerium also highlights the advantages of ion implantation as a research tool. The ability to precisely control which ions (and how many) enter the film means that it is possible to better understand how qualitative phenomena are related to the physical composition of the film.

5.3 Suggestions for future work

5.3.1 Material fabrication and characterization

i) Silicon nanocrystals

The observed result of about 0.81% ± 0.60% internal quantum efficiency for Si-NCs in fused silica suggests that some creativity and further work is required before they

will be useful as down-shifters. However, high quantum efficiencies (~60 %) have been reportedly obtained from Si-NCs when they are terminated in organic ligands [29]. The challenge is to incorporate oxygen-free Si-NCs into a mechanically-robust down-shifting material compatible with the natural environment where a typical PV cell is used.

Further work is needed to ascertain whether Si-NCs were created through oxygen implantation. Transmission electron microscopy of these samples might be able to investigate whether Si-NCs or small SiO_2 particles are present, and their average size. If Si-NCs are present, it raises many possible future avenues of research. Firstly, a study of the range of Si-NC emission wavelength and intensity, as they vary with oxygen fluence, would be useful. An investigation of the relationship between Si-NC location and the simulated oxygen-implanted vacancies could determine whether a similar relationship exists to the one found by Mokry *et al.* for silicon-implanted Si-NCs [64]. Heavily p-type or n-type doped silicon could be implanted with oxygen to also potentially form Si-NCs, and then the electrical conductivity of the samples could be compared with lightly-doped samples.

Furthermore, if these are oxygen-implanted Si-NCs, they present the opportunity for electrical activation of Si-NCs, by increasing the likelihood of carrier transport from contacts on the rear of the silicon substrate, through an increasingly silicon-poor region to the Si-NCs, and then continuing through an increasingly silicon-rich region to the metal contacts at the surface. Carrier transport has been cited as one of the main challenges to extracting electroluminescence from Si-NCs [78], and these oxygen implanted samples could present a unique opportunity for further study.

If the transmission electron microscopy images do not show the presence of Si-NCs, but rather SiO_2 particles, this could clarify the source of the PL from samples created through silicon or oxygen implantation.

ii) Energy transfer between Si-NCs and erbium

It was shown that Si-NCs transferred energy to erbium; however, the quantum efficiency of that process was not investigated due to lack of infrared equipment at McMaster University. If the Si-NC-erbium concentrations were optimized to obtain a strong erbium signal, then it should be possible to measure the conversion efficiency of implanted fused silica samples.

It would also be useful to investigate the same process for Si-NC fused silica samples doped with other lanthanide rare-earths, including via time resolved spectroscopy.

iii) Cerium photoluminescence

The cerium- and oxygen-doped Si_3N_4 films showed that there was an optimal ratio of cerium/oxygen, which was not obtained for the cerium-doped fused silica sample. The cerium-doping of fused silica should be optimized to obtain intense PL, and the quantum efficiency of the PL from optimally doped fused silica should be compared with sub-optimally cerium-doped fused silica.

In future work, X-ray synchrotron spectroscopy would be useful to verify the state of oxygen coordination of the cerium. Time resolved PL could be used to determine if the preliminary calculation of cerium lifetime based on the QE PL measurements and the implanted cerium fluence is correct.

This work showing the dependence of cerium PL on oxygen concentration also raises the possibility that other rare-earths might have the same dependency. For example, Gourbilleau *et al.* looked at trivalent neodymium ions (Nd^{3+}) in silicon dioxide films containing Si-NCs [45]. They observed that the Nd^{3+} PL signal decreased when the atomic concentration of Nd^{3+} surpassed 0.08 %, while the concentration of excess silicon was fixed. It is possible that in films with lower excess silicon concentration (higher

oxygen concentration) the peak PL form Nd^{3+} would occur at a higher atomic concentration.

iv) Cerium energy transfer to other rare-earths

Co-doping a substrate, such as fused silica or Si_3N_4, with both cerium and another lanthanide rare-earth, should be done to investigate the energy transfer between cerium and another rare-earth. The performance of cerium energy capture and transfer could be compared with the performance of Si-NC energy capture and transfer to other rare-earths.

v) Laser-annealed fused silica chalcogenated rare-earths

Numerous research groups have found that lanthanide rare-earth radiative performance is enhanced if the host material is a low-phonon energy material. However, these materials tend to have very small crystalline structures, which would be challenging to incorporate as down-shifting materials. In order to take advantage of the mechanical robustness of quartz, and the improved radiative performance of lanthanide-doped chalcogenated materials, for example, it would be useful to investigate an emerging class of materials. Laser-pulsed annealing has been used to “freeze” chalcogen dopants in the silicon surface [38], and it is possible that silicon (or fused silica) doped with rare-earths would also have improved radiative performance, and still retain the mechanical robustness of the substrate.

vi) Characterization of ion implanted Films

Ion implantation led to challenges during the modeling of the optical constants of the films using VASE and Rutherford backscattering. This was often overcome by approximating the implanted profile as a single-layer thin-film. Future work could focus on obtaining more precise optical constants, or atomic compositions, of these implanted films.

5.3.2 Improvements to experimental design

In order to perform some of the suggestions listed above, a few pieces of equipment would be required in addition to those in place at McMaster University. These include the acquisition of a high-power light source of variable wavelength – such as a xenon arc lamp and monochromator. An Ocean-Optics infrared charge-coupled device (CCD) would make infrared measurements easier, and would be particularly useful when used in conjunction with the UV-Visible CCD and a bifuricated optical cable.

There is some experimental error in the ion flux provided by the ion implanter, which would be useful to quantify. This would perhaps be possible using cerium-doped samples, which show such fine variation in PL that incomplete rastering was detected after one of the cerium implantations. Recently, the ion implanter has undergone an upgrade to magnetically focus the beam earlier in the beamline to increase the ion current and speed up the implantation process.

The integrating sphere QE set-up would be improved if the sample holder was attached to a rotating stage, which would make it possible to return the sample to the same orientation in the sphere and improve the consistency of the integrating sphere measurements.

Many of the investigated materials involved high doping levels via ion implantation. The Stopping and Range of Ions in Matter (SRIM) [51] provides some indication of the peak location of ions based in part on the composition of the original material. It would be interesting to investigate how well SRIM deals with complete changes in material composition given large implantation fluences. Once that is determined, then it would be easier to optimally dope Si-NCs with a rare-earth like erbium.

5.4 Final remarks

The intrinsic limitations of SJSPVCs, and indeed any single-junction PV cell, present a challenge to effectively converting all the energy in the broad solar spectrum into electricity. This thesis contains information showing that it is indeed possible to transform high energy photons into lower energy photons, with quantum efficiencies and peak absorption and wavelengths that depend on the dopant. However, more work is needed before this technology improves the performance of most PV cells.

The variation in conversion efficiency and peak emitted wavelength that were obtained indicate that there are many possible down-shifting material compositions; indeed, a down-shifter could eventually be optimized for each type of PV cell on the market. In particular, one that it appears would benefit from a down-shifter is the Cd-Te cell, which has poor EQE through the UV region. Another research group has explored the use of organic down-shifters to move those UV photons to longer wavelengths, but it is possible that a high efficiency cerium down-shifter could have good results.

While this project did not produce a down-shifter that improves the performance of SJSPVCs, advances have been made in the characterization of luminescent materials. It is worth noting that spectral engineering technology could have other applications in imaging systems, optical communications, and the luminescent technology could even transfer over into electrically-pumped light-emitting devices. Cerium-doped fused silicon could be marketed as a sensor for UV light, incorporated into a standard measurement calibration system for scientific research, or used as an architectural material to generate blue skylight even on cloudy days.

Appendix A Dicing Saw Standard Operating Procedure

Read this entire operating procedure before using the Dicing Saw. If you have any questions or concerns, contact your supervisor before operating the machine.

START-UP

Turn on the air valve behind the saw and check that the pressure is ~ 80 psi.

Turn on the water valve behind the saw and check that the pressure is ~45 psi.

Unlock the cabinet below the saw and take out equipment (i.e. door switch, chuck, spacers, etc.).

MOUNTING THE BLADE

Raise splash guard (safety window).

Remove spindle cover by unscrewing the two knob screws.

Slide on the larger spacer with the widest diameter facing outward.

Carefully slide on the blade, with the sharp edge facing in. **Don't touch the edge of the blade** or bash it against the screws around the spindle.

Slide on the smaller spacer, with the widest diameter facing inward.

Screw on the outer piece using the special tool provided, and use approximately 10 lb of torque.

START-UP

Mount safety switch on door and turn on.

Blow dust off the two chuck pieces and chuck holder using air gun, and mount the chuck with the smaller piece underneath.

Power on machine by pressing big red knob.

Select program to move chuck/sample stage.

MOUNTING SAMPLE

Before you mount the sample, note that you will need to know the dimensions of the sample when programming the machine, including the sample thickness.

Make sure table surface work-area is clean.

Separate the plastic rings, and place the small ring with the sharp edge down. Cut a rectangular piece of blue tape larger than the surface area of the smaller ring, and place blue tape over the small ring with the sticky side up. Press the larger ring down over the tape and the smaller ring. Cut off excess tape.

Place sample cutting side down on the table and carefully press the sticky side of the tape over the exposed backside of the sample, making sure the sample is centered in the ring, and removing air bubbles from between the sample and the tape.

Mount the sample & ring on the chuck so that the sticky side is facing up and the outer ring is below the edge of the chuck. Press "Vac" to initiate the vacuum.

Line up the edge of the sample with the microscope/monitor, and press 'display reset' to zero

the display.

Press ‘Water’ and check that the water is spraying directly on the entire exposed blade.

Put the spindle cover back on, and tighten the screws back in place.

Lower splash guard.

Start/check the spindle by pressing the “Spindle” button.

Check the height by pressing ‘height sense’.

DICING THE SAMPLE

Select ‘Program’.

Choose reasonable parameters for spindle speed, feed rate, etc. based on training.

Preferably on a scrap area of the sample, check the sample height. Set the cut depth to 0.001mm (1 μm) and set the sample height to the measured sample thickness + the tape thickness. (Tape thickness is

~50 μm or 0.050mm). By changing the height in small steps and performing single cuts, find the height at which the blade barely touches the sample surface, and leave this as the programmed sample height.

Perform a deeper cut to align the crosshairs on the monitor to the width of the blade. Move the crosshair Y1 to the location of the cut by manual adjustment.

Select appropriate cutting parameters for the program, saving them each time, and double-checking each.

Dice the sample.

CLEANING SAW AND SHUTTING DOWN

Wear safety goggles while cleaning the machine due to the possibility of getting water with

silicon/quartz shards in the eyes.

Remove sample holder and sample.

Rinse away all water on chuck and saw with DI water bottle and dry with air hose.

Rinse all metal plates and chuck.

Let vacuum help drain DI water (press vacuum, and squirt water into holes)

TURN OFF SPINDLE, and then open spindle cover and take out blade. Watch out for the posts, don't ding the blade.

Grab wipe with tweezers, rinse with DI, and scrub out the blade holder and splash guard.

Replace splash guard.

Rinse and wipe the lid.

Press the red shut-down button.

Turn off and remove the power switch key on the cabinet door.

Put everything that you took out of the cabinet back in the cabinet.

Lock the cabinet.

Turn off the water and air valves.

References

1. Dicing Saw SOP (14/07/2004) by J. Bradley and P. Foster. Updated by Rachel Savidge Dec. 2010

Appendix B SRIM Simulations

The following SRIM simulation results indicate the peak implantation depth and the concentration per fluence, which was used to determine the implantation fluence of each ion. 4000 atoms were run for each simulation. The most common isotope of the element was always simulated.

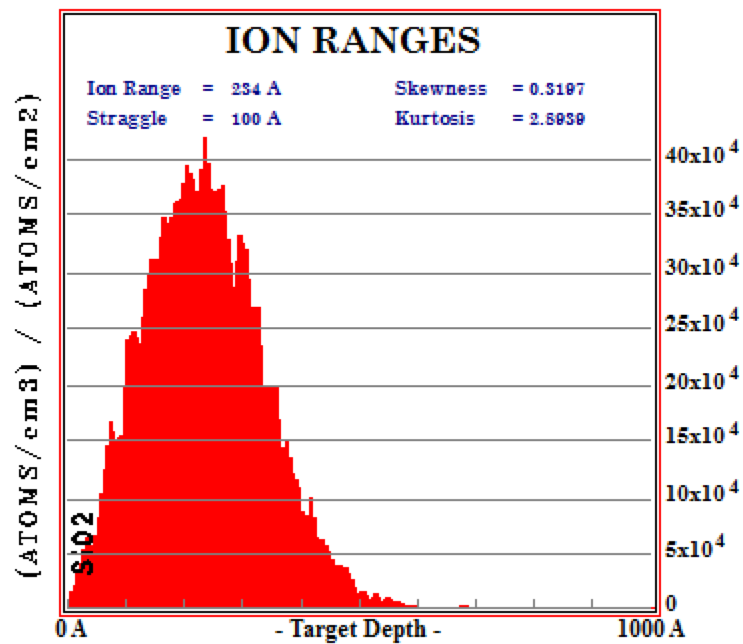

Appendix Figure B-1: Si^{+} (15 keV) implanted into SiO_2 at a seven-degree angle for creating Si-NCs.

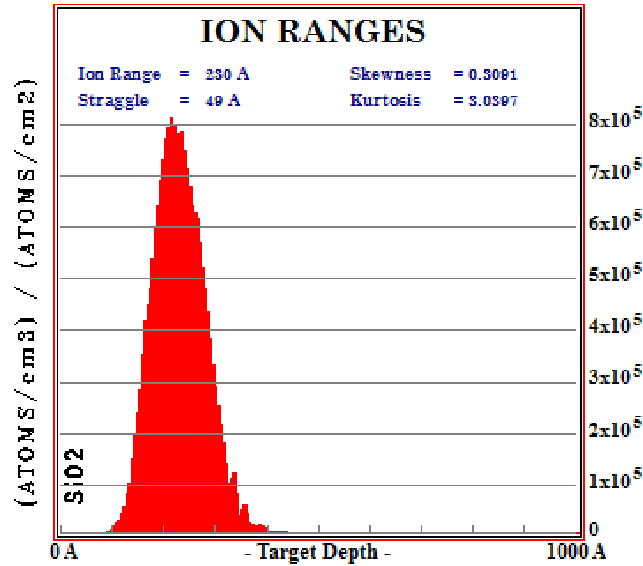

Appendix Figure B-2: Er^{3+} (35 keV) implanted into SiO_2 at a seven-degree angle in addition to Si-NCs in fused silica.

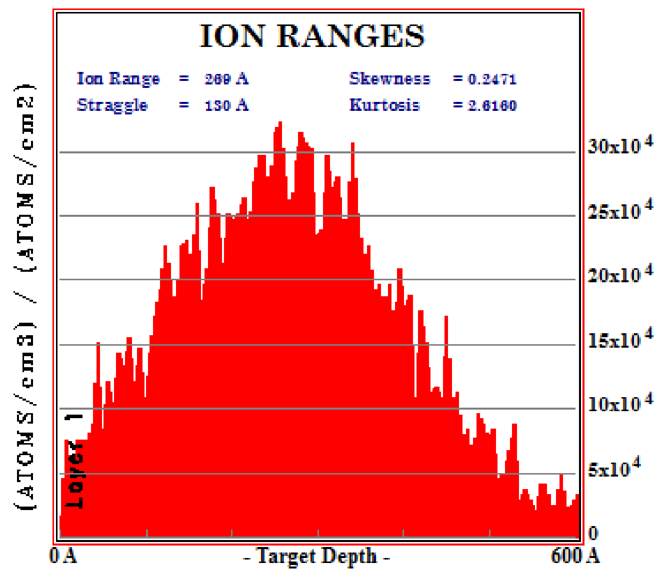

Appendix Figure B-3: O^+ (9.5 keV) == O_2^+ (19 keV) implanted into silicon at a seven-degree angle.

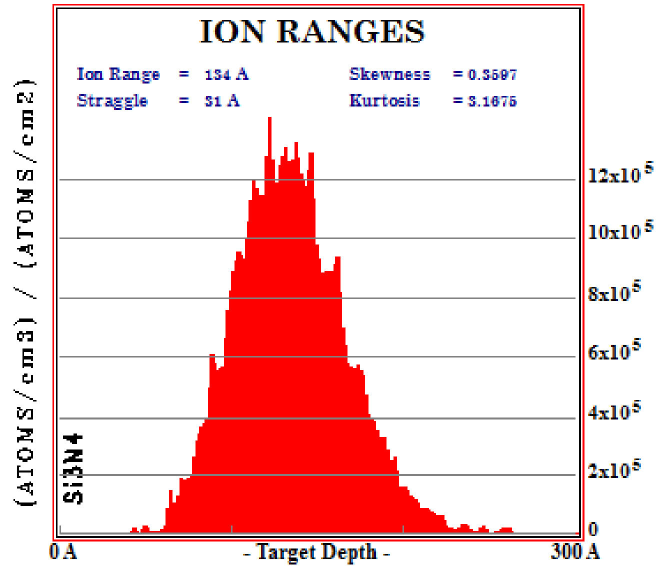

Appendix Figure B-4: Ce^{+} (25 keV) implanted into Si_3N_4 at a seven-degree angle.

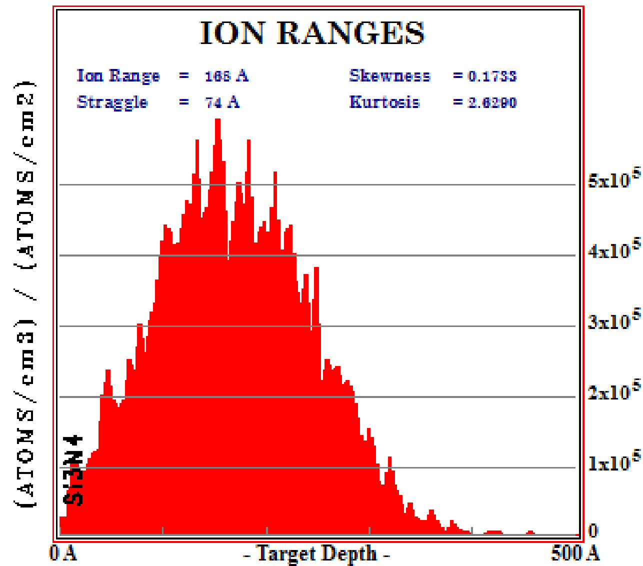

Appendix Figure B-5: O^{+} (9.5 keV) == O_2^{+} (19 keV) implanted into Si_3N_4 at a seven-degree angle. The implantation energy was chosen to match the peak of the cerium implantation shown in Appendix Figure B-4.

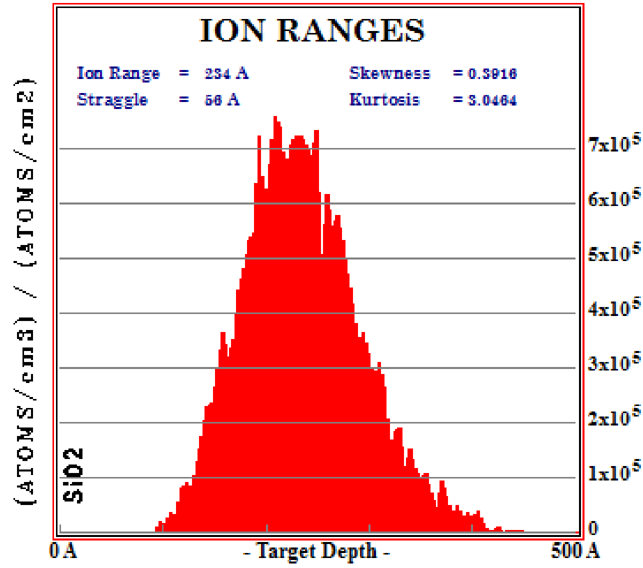

Appendix Figure B-6: Ce^{+} (32.5 keV) implanted into SiO_2 at a seven-degree angle.

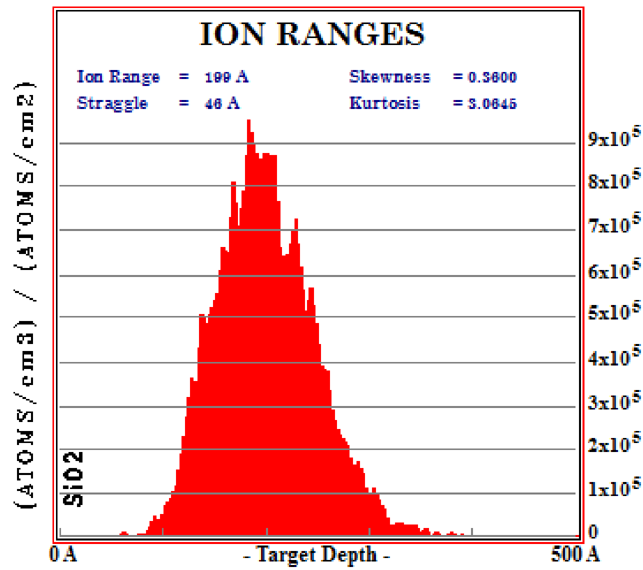

Appendix Figure B-7: Ce^{+} (25 keV) implanted into SiO_2 at a seven-degree angle.

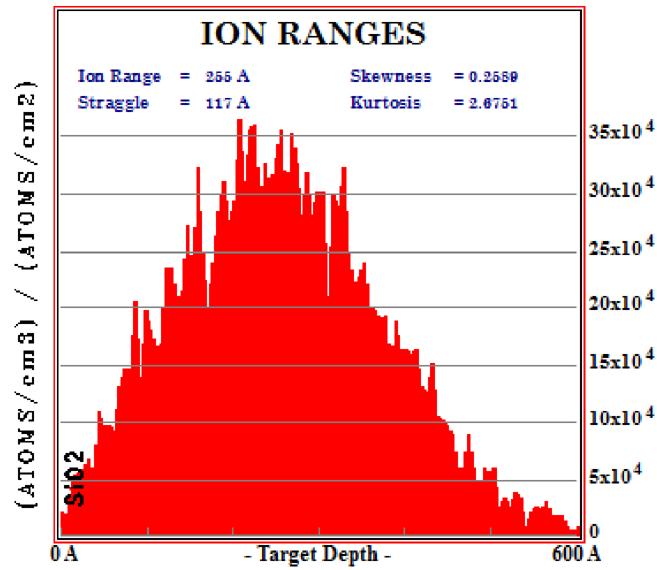

Appendix Figure B-8: O^+ (9.5 keV) == O_2^+ (19 keV) implanted into SiO_2 at a seven-degree angle.

Appendix C Calibration of the Rapid Thermal Annealer

A test was performed to determine the accuracy of the pyrometer used in the RTA. Silicon di-oxide was grown on a <1-0-0> silicon wafer at higher temperature in an oxygen-rich environment. Growth of thermal oxide is a well-documented process, and there are two equations used to determine the resulting oxide-thickness: one for the short-growth region and one for the long-growth region.

The initial oxide thickness on the unannealed silicon wafer was measured using single-beam ellipsometry (632.8 nm). Three samples were placed at the 12 o'clock, 4 o'clock and 8 o'clock positions in the platform centre, with about 2 cm spacing between each. The RTP was set to a temperature for 30 minutes, and the resultant silicon dioxide growth thickness was measured. This was done for a number of temperatures, displayed in the chart below.

AppendixTable C.1: Rapid thermal annealer raw data for calibration

RTP Calibration, June 6, 2011					
Temperature	**Temperature**	**Control Unannealed**	**Sample 1**	**Sample 2**	**Sample 3**
(°C)	(°K)	Thickness (Å) - single point measurement, avg. of 5 scans			
20	293	0.0078			
950	1223		219.18	197.43	178.39
980	1253		245.79	256.98	232.78
1010	1283		459.23	315.75	388.24
1040	1313		494.44	464.97	537.69
RTP Calibration, June 7, 2011					
20	293	0.0094			
1070	1343		659.52	621.04	583.05
1100	1373		800.18	799.77	776.73

The initial oxide thickness was used to calculate the adjustment time, τ, in hours. That number was added to the anneal time (0.5 hours) to give the total effective anneal time for the final oxide thickness.

AppendixTable C.2: Rapid thermal annealer calibration constants from charts

Temperature	Control Unannealed	B (from charts)	B/A (from charts)	τ =X_0^2/B+X_0/(B/A)	T= 0.5 + τ
(°K)	Thickness (Å) - single point measurement, avg. of 5 scans	(μm^2/hr)	(μm/hr)	(hr)	(hr)
293	0.0078				
1223		0.006	0.019	0.414	0.914
1253		0.008	0.031	0.261	0.761
1283		0.010	0.049	0.164	0.664
1313		0.014	0.079	0.104	0.604
293	0.0094				
1343		0.018	0.126	0.080	0.580
1373		0.024	0.200	0.051	0.551

B = Parabolic Constant
B/A = Linear Constant

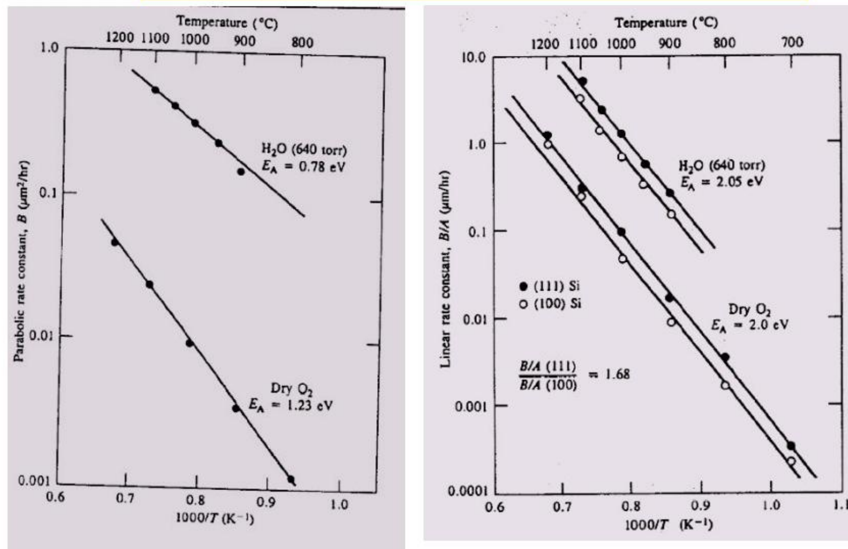

Appendix Figure C-1: Calibration charts for thermal oxidation constants. Taken from [79].

Based on the oxide thickness and the growth equations, the actual temperature of the RTP was calculated and is shown in

AppendixTable C.3: Calculated rapid thermal annealer temperature based on the measured oxide thickness.

Programmed Temperature (°K)	Sample 1 Calculated Temperature	Sample 2 Calculated Temperature	Sample 3 Calculated Temperature
1223	1247	1236	1225
1253	1258	1262	1253
1283	1311	1281	1298
1313	1317	1312	1323
1343	1338	1334	1329
1373	1352	1352	1350

Observations: Significant temperature variation (up to +24 °K), especially at lower temperatures. The 1343 +24 °K and 1373 +24 °K measurements start to fit with the thick-oxide growth region (see the following slide).

Conclusions:

- Temperature variation (typically +10 °C, max variation of +24 °C) over centre are of RTP platform, particularly at low temperatures (<1070 °C).
- RTP appears to be reasonably well-calibrated.

Appendix D Photoluminescence Set-up Standard Operating Procedure

STARTUP

Ensure black safety cap is covering laser opening.

Turn on grey interlock box.

Turn on oscilloscope and make sure it is not offset.

Power supply: min 0.46 V ; max 0.90 V.

Turn ignition key on Laser Diode Control unit (LDCU)

Let laser heat up for 15 – 30 mins.

Power up PC. Password "lab"

Open Spectrasuite or SP System Start-up program

Wearing safety glasses, remove black safety cap from front of laser.

Perform measurements.

SHUTDOWN

Close computer programs and power-off PC.

Cover laser with safety cap, turn off laser power supply. Turn off ignition key and interlock box and power-off oscilloscope.

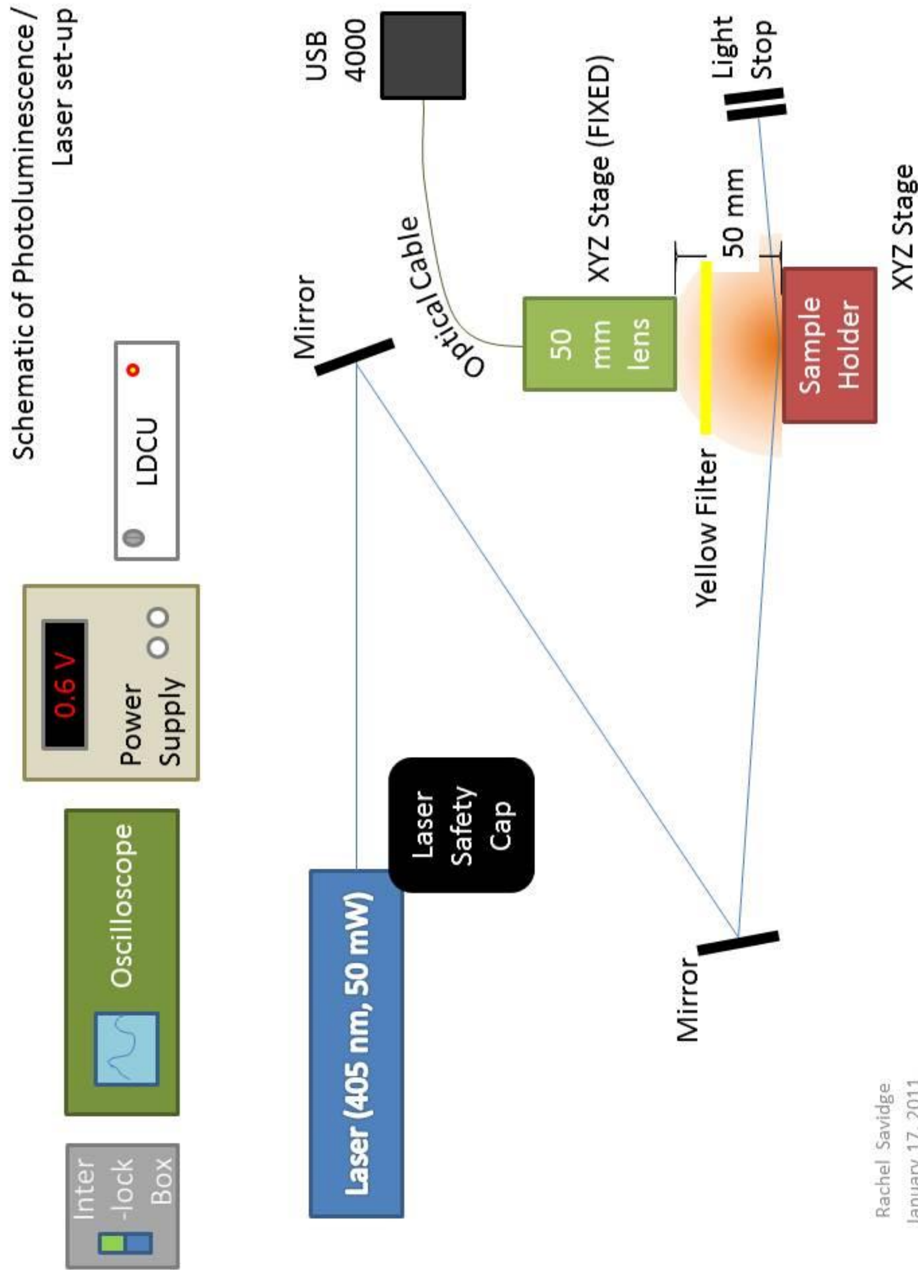

Schematic of Photoluminescence / Laser set-up
LDCU
0.6 V
Power Supply
Oscilloscope
Inter -lock Box
Laser (405 nm, 50 mW)
Laser Safety Cap
Mirror
Optical Cable
USB 4000
50 mm lens
XYZ Stage (FIXED)
Light Stop
50 mm
Yellow Filter
Sample Holder
XYZ Stage
Mirror
Rachel Savidge
January 17, 2011

Appendix E Quantum Efficiency Error Calculations

The following calculations were performed in order to calculate the error associated with the internal and external quantum efficiency measurements, according to the propagation of errors.

Silicon Nanocrystal Quantum Efficiency Error Calculations

The diameter of the integrating sphere input port is given as: 0.500” ± 0.0005”. The area of the port A_i is given by:

$A_i = 2\pi r^2 = 0.1963$ sq in

where r is the radius of the input port (0.250” ±0.00025”). The input port area error, by the propagation of errors, is:

$$\frac{\Delta A_i}{A_i} = 2\frac{\Delta r}{r},$$

so $\Delta A_i = 0.0393$ sq in.

The diameter of the sphere interior is given as: 3.3” ±0.05”. The internal surficial sphere area A_s is given by:

$A_s = 4\pi r^2 = 34.2119$ sq in

where r is the radius of the sphere interior (1.65” ±0.025”). The internal surficial sphere area error, by the propagation of errors, is:

$$\frac{\Delta A_s}{A_s} = 2\frac{\Delta r}{r}$$

so ΔA_s = 0.52 sq in.

The output port size, A_o, for the optical fiber was assumed to be a constant based on an assumed constant 200 μm diameter for the fibre.

The port fraction, f, is calculated as

$$f = \frac{A_o + A_i}{A_s}$$, so f = 0.0057

The port fraction error, by the propagation of errors is:

$$\frac{\Delta f}{f} = \frac{\Delta A_i}{A_i} + \frac{\Delta A_s}{A_s}$$

so Δf = 0.0012 sq in.

The sphere response, R_s, is also based on the port fraction, and it is wavelength-dependent:

$$R_s = \frac{\rho \cdot A_f (1 - R) \cdot \Omega}{\pi A_s (1 - \rho(\lambda) \cdot (1 - f))}$$

which is based on the fiber cross-sectional and sphere surficial areas, A_f and A_s, respectively, the wavelength-dependent reflectance of the sphere's interior coating, $\rho(\lambda)$, the port fraction, f, the facial reflectance, R, and solid angle of the fiber, Ω. The two variables with known error are A_s and f, so the error associated with the sphere response is determined by taking R_{s_400nm} = 0.00100 at a representative wavelength of 400 nm:

$$\frac{\Delta R_s}{R_s} = \frac{\Delta f}{f} + \frac{\Delta A_s}{A_s}$$

$\Delta R_{s_400nm} = 0.00023$

and likewise, $R_{s_800nm} = 0.00105$, so $\Delta R_{s_800nm} = 0.00024$.

$\Phi_{incident} = \phi_f / R_s$

ϕ_f = number of photons measured at detector

The number of photons measured at the detector varied depending on the rotational orientation of the sample holder. The measurement error was estimated by taking repeat measurements of the 405 nm laser line in the sphere and trying to return the sample holder to the same orientation. Here, $\phi_{f_incident} = 1.90\text{x}10^{14}$ photons/s/cm^2/nm, and

$\Delta\phi_{f_incident} = 1.758\text{x}10^{12}$ photons/s/cm^2/nm

$\Phi_{incident} = \phi_f / R_s = 2.06\text{x}10^{17}$ photons/s/cm^2/nm

$$\frac{\Delta\phi_{incident}}{\phi_{incident}} = \frac{\Delta\phi_{f_incident}}{\phi_{f_incident}} + \frac{\Delta R_s}{R_s}$$

$\Delta\ \Phi_{incident} = 4.82\text{x}10^{16}$ photons/s/cm^2/nm

Likewise for $\Phi_{emitted}$ for the Si-NCs

The number of photons measured at the detector varied depending on the rotational orientation of the sample holder. The measurement error was estimated by taking repeat measurements of the Si-NC emission in the sphere and trying to return the sample holder to the same orientation. Here, $\phi_{f_emitted} = 4.97\text{x}10^{13}$ photons/s/cm^2/nm, and the sphere response at 800 nm was considered.

$R_{s_800nm} = 0.001051086$

$\Delta R_{s_800nm} = 0.00024$

$\Delta\phi_{f_emitted} = \sim 2.468\text{x}10^{12}$ photons/s/cm^2/nm

$\Phi_{emitted} = \phi_f / R_s = 4.72844\text{x}10^{16}$ photons/s/cm^2/nm

$$\frac{\Delta\phi_{emitted}}{\phi_{emitted}} = \frac{\Delta\phi_{f_emitted}}{\phi_{f_emitted}} + \frac{\Delta R_s}{R_s}$$

$\Delta\,\Phi_{emitted} = 1.3\text{x}10^{16}$ photons/s/cm^2/nm

$$EQE = \frac{\phi_{emitted}(\lambda)}{\phi_{incident}(\lambda)}$$

$EQE = 0.020\%$

$$\frac{\Delta EQE}{EQE} = \frac{\Delta\phi_{emitted}(\lambda)}{\phi_{emitted}(\lambda)} + \frac{\Delta\phi_{incident}(\lambda)}{\phi_{incident}(\lambda)}$$

$\Delta EQE = 0.0103\%$

Likewise, IQE error calculation: $\Phi_{absorbed}$ by the Si-NCs is as follows:

$$\phi_{absorbed_nc}(\lambda) = \phi_{fs}(\lambda) - \phi_{ds}(\lambda)$$

From above (incident = fs=fused silica):

$\Delta\ \Phi_{fs} = 4.82\text{x}10^{16}$ photons/s/cm^2/nm

$\Phi_{fs} = \phi_f / R_s = 2.06\text{x}10^{17}$ photons/s/cm^2/nm

The number of photons measured at the detector varied depending on the rotational orientation of the sample holder. This was assumed to be the same error as the laser line in the sphere: 23%.

$\Delta\phi_{f\ _ds} = \sim 2.48\text{x}10^{12}$ photons/s/cm^2/nm (measured)

$\Phi_{absorbed_nc} = \phi_f / R_{s_400nm} = 9.860\text{x}10^{15}$ photons/s/cm^2/nm

$$\frac{\Delta\phi_{absorbed_nc}}{\phi_{absorbed_nc}} = \frac{\Delta\phi_{fs}}{\phi_{fs}} + \frac{\Delta\phi_{ds}}{\phi_{ds}}$$

$\Delta\Phi_{absorbed_nc} = 4.57\text{x}10^{15}$ photons/s/cm^2/nm

Laser only in sphere: $\Delta\phi_f = 2.5\text{x}10^{12}$ photons/s/cm^2/nm

$\Delta\phi_{f\ _Si\text{-}nc\ absorption} \sim 2.8\text{x}10^{15}$ photons/s/cm^2/nm

$\Delta\ \Phi_{emitted} = 1.3\text{x}10^{16}$ photons/s/cm^2/nm

$\Phi_{emitted} = \phi_f / R_s = 4.728\text{x}10^{16}$ photons/s/cm^2/nm

$$IQE = \frac{\phi_{emitted}(\lambda)}{\phi_{absorbed}(\lambda)}$$

$$IQE = 0.81\%$$

$$\frac{\Delta IQE}{IQE} = \frac{\Delta\phi_{emitted}(\lambda)}{\phi_{emitted}(\lambda)} + \frac{\Delta\phi_{absorbed}(\lambda)}{\phi_{absorbed}(\lambda)}$$

$$\Delta IQE = 0.60\%$$

Cerium Internal Quantum Efficiency Error Calculation

The diameter of the integrating sphere input port is given as: 0.500” ± 0.0005”. The area of the port A_i is given by:

$A_i = 2\pi r^2 = 0.1963$ sq in
where r is the radius of the input port (0.250” ±0.00025”). The input port area error, by the propagation of errors, is:

$$\frac{\Delta A_i}{A_i} = 2\frac{\Delta r}{r},$$

so $\Delta A_i = 0.0393$ sq in.

The diameter of the sphere interior is given as: 3.3” ±0.05”. The internal surficial sphere area A_s is given by:

$A_s = 4\pi r^2 = 34.2119$ sq in

where r is the radius of the sphere interior (1.65” ±0.025”). The internal surficial sphere area error, by the propagation of errors, is:

$$\frac{\Delta A_s}{A_s} = 2\frac{\Delta r}{r}$$

so $\Delta A_s = 0.52$ sq in.

The output port size, A_o, for the optical fiber was assumed to be a constant based on an assumed constant 200 μm diameter for the fibre.

The port fraction, f, is calculated as

$$f = \frac{A_o + A_i}{A_s}$$, so f = 0.0057

The port fraction error, by the propagation of errors is:

$$\frac{\Delta f}{f} = \frac{\Delta A_i}{A_i} + \frac{\Delta A_s}{A_s}$$

so $\Delta f = 0.0012$ sq in.

The sphere response, R_s, is also based on the port fraction, and it is wavelength-dependent:

$$R_s = \frac{\rho \cdot A_f (1-R) \cdot \Omega}{\pi A_s (1-\rho(\lambda) \cdot (1-f))}$$

which is based on the fiber cross-sectional and sphere surficial areas, A_f and A_s, respectively, the wavelength-dependent reflectance of the sphere’s interior coating, $\rho(\lambda)$, the port fraction, f, the facial reflectance, R, and solid angle of the fiber, Ω. The two

variables with known error are A_s and f, so the error associated with the sphere response is determined by taking R_{s_325nm} = 0.000809174 at a wavelength of 325 nm:

$$\frac{\Delta R_s}{R_s} = \frac{\Delta f}{f} + \frac{\Delta A_s}{A_s}$$

ΔR_{s_325nm}= 0.00018, and we already know that ΔR_{s_400nm}= 0.00023.

Likewise $\Phi_{absorbed}$ by the cerium

$\Phi_{absorbed} = \phi_f / R_{s_400nm}$

ϕ_f = number of photons measured at detector

The number of photons measured at the detector varied depending on the rotational orientation of the sample holder. The measurement error was estimated by taking repeat measurements of the Si-NC emission in the sphere and trying to return the sample holder to the same orientation. Here, ϕ_f = 8.80x10^{10} photons/s/cm^2/nm, and the sphere response at 400 nm was considered for the cerium photoluminescence.

$\Delta\ \phi_{f\ _Ce\ absorption}$= 1.3% *8.80x10^{10} photons/s/cm^2/nm photons/s/cm^2/nm (1.3% assumed from Si-NC measurements since only one measurement of cerium sample was taken)

$\Delta\ \phi_{f\ _Ce\ absorption}$= 1.14x10^9 photons/s/cm^2/nm

$\Phi_{Ce_absorption}$= 1.09x10^{14} photons/s/cm^2/nm

$$\frac{\Delta\phi_{Ce_absorption}}{\phi_{Ce_absorption}} = \frac{\Delta\phi_f}{\phi_f} + \frac{\Delta R_s}{R_s}$$

ΔR_{s_325nm}= 0.00018

$R_{s_325nm} = 0.000809174$

$\Delta\Phi_{Ce_absorption} = 2.57\text{x}10^{13}$ photons/s/cm^2/nm

$$\frac{\Delta\phi_{emitted}}{\phi_{emitted}} = \frac{\Delta\phi_f}{\phi_f} + \frac{\Delta R_s}{R_s}$$

$\Phi_{emitted} = \phi_f/R_s = 2.24\text{x}10^{13}$ photons/s/cm^2/nm

$\phi_{f\ _Ce_abemission} = 1.71\text{x}10^{10}$ photons/s/cm^2/nm

$\Delta\ \phi_{f\ _Ce\ emission}$ = not observed, again assumed to be 1.3%

$\Delta R_{s\ _400nm} = 0.00023$

$R_{s_400nm} = 0.00100$

$\Delta\ \Phi_{emitted} = 5.44\text{x}10^{12}$ photons/s/cm^2/nm

$$IQE = \frac{\phi_{emitted}(\lambda)}{\phi_{absorbed}(\lambda)}$$

$IQE = 20.6\%$

$$\frac{\Delta IQE}{IQE} = \frac{\Delta\phi_{emitted}(\lambda)}{\phi_{emitted}(\lambda)} + \frac{\Delta\phi_{absorbed}(\lambda)}{\phi_{absorbed}(\lambda)}$$

$\Delta IQE = 9.9\%$

Works Cited

[1] M. Mendonca, D. Jacobs, and B. Sovacool, *Powering the Green Economy : The Feed-in Tariff Handbook*. London: Earthscan, 2009.

[2] G. Barbose, N. Darghouth, R. Wiser, and J. Seel, "Tracking the Sun IV: A Historical Summary of the Installed Cost of Photovoltaics in the United States from 1998 to 2010," Lawrence Berkeley National Laboratory, 2011.

[3] K. Ardani and R. Margolis, "2010 Solar Technologies Market Report," U.S. Department of Energy, 2011.

[4] M.A. Green and M. Keevers. (2012, July) "Optical properties of intrinsic silicon at 300 K". [Online]. http://www.pveducation.org/pvcdrom/appendicies/optical-properties-of-silicon

[5] M. A. Green, K. Emery, Y. Hishikawa, and W. Warta, "Solar cell efficiency tables (version 37)," *Prog. Photovolt. Res. Appl.*, no. 19, pp. 84-92, 2011.

[6] J. Sacks et al., Quantum Efficiency Measurements of Down-Shifting Using Silicon Nanocyrstals for Photovoltaic Applications, 2012, Poster presented at the Photovoltaics Specialist Conference.

[7] A. Shalav, B. S. Richards, and M. A. Green, "Luminescent layers for enhanced silicon solar cell performance: Up-conversion," *Sol. Energ. Mat. Sol. C.*, vol. 91, no. 9, pp. 829-842, 2007.

[8] B. S. Richards, "Luminescent layers for enhanced silicon solar cell performance: down-conversion," *Sol. Energ. Mat. Sol. C.*, vol. 90, no. 9, pp. 1189-1207, 2006.

[9] T. Trupke, M.A. Green, and P. Wurfel, "Improving solar cell efficiencies by down-conversion of high energy photons," *J. Appl. Phys.*, vol. 92, no. 3, pp. 1668-1674, 2002.

[10] A.M Gabr, J.F. Wheeldon, R.M. Beal, A. Walker, J. Sacks, R.M. Savidge, T.J. Hall, R.N. Kleiman, and K. Hinzer, "Modeling Down-Conversion and Down-Shifting for Photovoltaic Applications," in *Photovoltaic Specialists Conference*, Austin, 2012.

[11] T. Trupke, M.A. Green, and P. Wurfel, "Improving solar cell efficiencies by up-conversion of sub-bandgap light," *J. Appl. Phys.*, vol. 92, no. 7, pp. 4117-4122, 2002.

[12] J. de Mello, H.F. Wittmann, and R.H. Friend, "An Improved Experimental Determination of External Photoluminescence Quantum Efficiency," *Adv. Mater.*, vol. 9, no. 3, 1997.

[13] J. Valenta, R. Juhasz, and J. Linnros, "Photoluminescence from single silicon quantum dots at room temperature," *J. Lumin.*, vol. 98, pp. 15-22, 2002.

[14] A.R. Johnson, S.-J. Lee, J. Klein, and J. Kanicki, "Absolute photoluminescence quantum efficiency measurement of light-emitting thin films," *Rev. Sci. Instrum.*, vol. 78, p. 096101, 2007.

[15] K. Emery, "Characterizing thermophotovoltaic cells," *Semicond. Sci. Technol.*, vol. 18, pp. S228–S231, 2003.

[16] C. Honsberg and S. Bowden. (2012, July) PVCDROM. [Online]. http://www.pveducation.org/pvcdrom/

[17] S.J. Fonash, *Solar Cell Device Physics*, 2nd ed. Burlington, MA: Elsevier, 2010.

[18] A. Hryciw, A. Meldrum, K.S. Buchanan, and C.W. White, "Effects of particle size and excitation spectrum on the photoluminescence of silicon nanocrystals formed by ion implantation," *Nucl. Instrum. Methods Phys. Res., Sect. B*, vol. 222, pp. 469-476, 2004.

[19] T.H. Gfroerer, "Photoluminescence in Analysis of Surfaces and Interfaces," in *Encyclopedia of Analytical Chemistry*, R.A. Meyers, Ed. Chichester: John Wiley & Sons Ltd, 2000, pp. 9209-9231.

[20] L.T. Canham, "Silicon wire array fabrication by electrochemical and chemical dissolution of wafers," *Appl. Phys. Lett.*, vol. 57, no. 10, pp. 1046-1048, 1990.

[21] S.J. Fonash, *Solar Cell Device Physics*, 2nd ed. Burlington, MA, USA: Elsevier, 2010.

[22] D.C. Hannah, J. Yang, P. Podsiadlo, M.K.Y. Chan, A. Demortiere, D.J. Gosztola, P.B. Prakapenka, G.C. Schatz, U.R. Kortshagen, and R.D. Schaller, "On the Origin of Photoluminescence in Silicon Nanocrystals: Pressure-Dependent Structural and Optical Studies," *Nano Lett.*, July 2012, Just Accepted Manuscript.

[23] D. Riabinina, C. Durand, M. Chaker, and F. Rosei, "Photoluminescent silicon nanocrystals synthesized by reactive laser ablation," *Appl. Phys. Lett.*, vol. 88, no. 073105, 2006.

[24] I. Vasiliev, J.R. Chelikowsky, and R.M. Martin, "Surface oxidation effects on the optical properties of silicon nanocrystals," *Phys. Rev. B,* vol. 65, no. 12, p. 121302, 2002.

[25] V.Yu. Timoshenko, M.G. Lisachenko, O.A. Shalygina, and B.V. Kamene, "Comparative study of photoluminescence of undoped and erbium-doped size-

controlled nanocrystalline Si/SiO2 multilayered structures," *J. Appl. Phys.*, vol. 94, no. 4, pp. 2254-2260, 2004.

[26] S. Godefroo, M. Hayne, M. Jivanescu, A. Stesmans, M. Zacharias, O.I. Lebedev, G. Van Tendeloo, and V.V. Moshchalkov, "Classification and control of the origin of photoluminescence from Si nanocrystals," *Nat. Nano.*, vol. 3, p. 174, 2008.

[27] A.M. Chizhik, A.I. Chizhik, R. Gutbrod, A.J. Meixner, T. Schmidt, J. Sommerfeld, and F.Huisken, "Imaging and Spectroscopy of Defect Luminescence and Electron-Phonon Coupling in Single SiO_2 Nanoparticles," *Nano Lett.*, vol. 9, no. 9, pp. 3239-3244, 2009.

[28] M.V. Wolkin, J. Jorne, P.M. Fauchet, G. Allan, and C. Delerue, "Electronic States and Luminescence in Porous Silicon Quantum Dots: The Role of Oxygen," *Phys. Rev. Lett.*, vol. 82, no. 1, pp. 197-200, 1999.

[29] D. Jurbergs, E. Rogojina, L. Mangolini, and U. Kortshagen, "Silicon nanocrystals with ensemble quantum yields exceeding 60%," *Appl. Phys. Lett.*, vol. 88, no. 23, p. 233116, 2006.

[30] U.S. Sias, L. Amaral, M. Behar, H. Boudinov, and E.C. Moreira, "The excitation power density effect on the Si nanocrystals photoluminescence," *Nucl. Instr. and Meth. in Phys. Res. B*, vol. 250, pp. 178–182, 2006.

[31] J. Warga, R. Li, S.N. Basu, and L. Dal Negro, "Electroluminescence from silicon-rich nitride/silicon superlattice structures," *Appl. Phys. Lett.*, vol. 93, p. 151116, 2008.

[32] I.E. Anderson, R.A. Shircliff, B. Simonds, P. Stradins, P.C. Taylor, and R.T. Collins, "Synthesis and Characterization of PECVD-Grown, Silane-Terminated Silicon

Quantum Dots," in *PVSC*, Austin, 2012.

[33] M.J.F. Digonnet, *Rare-Earth-Doped Fibre Lasers and Amplifiers*, 2nd, Ed. New York: Marcel Dekker, Inc., 2001.

[34] I. Etchart and A. Cheetham, "Metal Oxides for Efficient Infrared to Visible Upconversion," University of Cambridge, Cambridge, PhD Thesis 2010.

[35] D. Schriver and P. Atkins, *Inorganic Chemistry*, 3rd ed. New York: W. H. Freeman and Company, 1999.

[36] B. Ahrens, P. Loper, J.C. Goldschmidt, S. Glunz, B. Henke, P.-T. Miclea, and S. Schweizer, "Neodymium-doped fluorochloro-zirconate glasses as an upconversion model system for high efficiency solar cells," *Phys. Stat. Sol.*, vol. 204, no. 12, pp. 2822–2830, 2008.

[37] S.H. Pan, D. Recht, S. Charnvanichborikarn, J.S. Williams, and M.J. Aziz, "Enhanced visible and near-infrared optical absorption in silicon supersaturated with chalcogens," *Appl. Phys. Lett.*, vol. 98, no. 121913, 2011.

[38] B.P. Bob, A. Kohno, S. Charnvanichborikarn, J.M. Warrender, I. Umezu, M. Tabbal, J.S. Williams, and M.J. Aziz, "Fabrication and subband gap optical properties of silicon supersaturated with chalcogens by ion implantation and pulsed laser melting," *J. Appl. Phys.*, vol. 107, no. 123506, 2010.

[39] J.-M. Meijer, L. Aarts, B.M. van der Ende, T.J.H. Vlugt, and A. Meijerink, "Downconversion for solar cells in YF_3:Nd^{3+}, Yb^{3+}," *Phys. Rev. B*, vol. 81, no. 035107, 2010.

[40] H. Jayatilleka, D. Diamare, M. Wojdak, A.J. Kenyon, C.R. Mokry, P.J. Simpson,

A.P. Knights, I. Crowe, and M.P. Halsall, "Probing energy transfer in an ensemble of silicon nanocrystals," *J. Appl. Phys.*, vol. 110, no. 033522, 2011.

[41] D. Pacifici, G. Franzò, F. Priolo, F. Iacona, and L. Dal Negro, "Modeling and perspectives of the Si nanocrystals–Er interaction for optical amplification," *Phys. Rev. B*, vol. 67, no. 245301, 2003.

[42] M. Wojdak, M. Klik, M. Forcales, O.B. Gusev, T. Gregorkiewicz, D. Pacifici, G. Franzò, F. Priolo, and F. Iacona, "Sensitization of Er luminescence by Si nanoclusters," *Phys. Rev. B*, vol. 69, no. 233315, 2004.

[43] F. Gourbilleau, R. Rizk, C. Dufour, and R. Madelon, "Effects of the Si-nanocluster size on the sensitizing role towards Er ions," *Eur. Phys. J. B*, vol. 51, pp. 341–344, 2006.

[44] G. Franzo, V. Vinciguerra, and F. Priolo, "The excitationmechanism of rare-earth ions in silicon nanocrystals," *Appl. Phys. A*, vol. 69, pp. 3-12, 1999.

[45] F. Gourbilleau, D. Breard, C. Dufour, and R. Rizk, "Rare earth emitters coupled to Si nanoclusters in thin films," *Opt. Mater.*, vol. 31, pp. 479-483, 2009.

[46] B. Dierre, R.J. Xie, N. Hirosaki, and T. Sekiguchi, "Blue emission of Ce^{3+} in lanthanide silicon oxynitride phosphors," *J. Mater. Res.*, vol. 22, no. 7, pp. 1933-1941, 2007.

[47] J. Li, O. Zalloum, T. Roschuk, C. Heng, J. Wojcik, and P. Mascher, P. "The formation of light emitting cerium silicates in cerium-doped silicon oxides," *Appl. Phys. Lett.*, vol. 94, no. 011112, 2009.

[48] UQG Optics. (2012, July) Data Sheet: UV Fused Silica– Spectrosil. [Online].

http://www.uqgoptics.com/pdf/Fused%20Silica%20-%20Spectrosil.pdf

[49] J.D. Plummer, M.D. Deal, and P.B. Griffin, *Silicon VLSI Technology: Fundamentals, Practice and Modeling*. Upper Saddle River, NJ: Prentice Hall, 2000.

[50] M. Quirk and J. Serda, *Semiconductor Manufacturing Technology*, S. Helba, Ed. Upper Saddle River, New Jersey: Presntice Hall, 2001.

[51] J.F. Ziegler. (2012, August) Particle Interactions with Matter. [Online]. http://www.srim.org/

[52] J.F. Ziegler, *Ion implantation: Science and Technology*. Orlando: Academic Press, 1984.

[53] D. Barba, D. Koshel, F. Martin, G.G. Ross, M. Chicoine, F. Schiettekatte, M. Yedji, J. Demarche, and G. Terwagne, "Silicon nanocrystal synthesis by implantation of natural Si isotopes," *J. Lumin.*, vol. 130, pp. 669-673, 2010.

[54] A. Kanjilal, L. Rebohle, M. Voelskow, W. Skorupa, and M. Helm, "Influence of annealing on the Er luminescence in Si-rich SiO_2 layers coimplanted with Er ions," *J. Appl. Phys.*, vol. 104, p. 103522, 2008.

[55] Ocean Optics. (2012, July) [Online]. http://www.oceanoptics.com/products/usb2000+precon.asp

[56] Ocean Optics. (2012, July) [Online]. http://www.oceanoptics.com/products/ls1cal.asp

[57] A. Johnson, S. Lee, J. Klein, and J. Kanicki, "Absolute photoluminescence quantum efficiency measurement of light-emitting thin films," *Rev. Sci. Instrum.*, vol. 78, no.

9, p. 096101, 2007.

[58] Labsphere, "A Guide to Integrating Sphere Theory and Applications," 2011.

[59] J. Sacks, R.M. Savidge, A. Gabr, A. Walker, R. Beal, J. Wheeldon, A.P. Knights, P. Mascher, K. Hinzer, and R.N. Kleiman, "Quantum Efficiency Measurements of Down-Shifting Using Silicon Nanocrystals for Photovoltaic Applications," 2012, Conference Poster.

[60] J.A. Woollam, B. Johs, C.M. Herzinger, J. Hilfiker, R. Synowicki, and C.L. Bungay, "Overview of Variable Angle Spectroscopic Ellipsometry (VASE), Part I: Basic Theory and Typical Applications," *Critical Reviews of Optical Science and Technology*, vol. CR72, pp. 3-28, July 1999.

[61] J.A. Woollam Company Inc., "Measuring Multilayer Thin Film Structures with Spectroscopic Ellipsometry," *Vacuum Technology & Coating*, December 2001.

[62] A. En Naciri, M. Mansour, L. Johann, J.J. Grob, and C. Eckert, "Optical study of Si nanocrystals in Si/SiO2 layers by spectroscopic ellipsometry," *Nucl. Instrum. Methods Phys. Res., Sect. B*, vol. 216, pp. 167-172, 2004.

[63] A. En Naciri, M. Mansour, L. Johann, J.J. Grob, and C. Eckert, "Correlation between silicon nanocrystalline size effect and spectroscopic ellipsometry responses," *Thin Solid Films*, vol. 455–456, pp. 486–490, 2004.

[64] C.R. Mokry, P.J. Simpson, and A.P. Knights, "Role of vacancy-type defects in the formation of silicon nanocrystals," *J. Appl. Phys.*, vol. 105, no. 114301, 2009.

[65] H. Nishikawa, R.E. Stahlbush, and J.H. Stathis, "Oxygen-deficient centers and excess Si in buried oxide using photoluminescence spectroscopy," *Phys. Rev. B*, vol.

60, no. 23, 1999.

[66] Y. Li, J.A. Kilner, P.L.F. Hemment, A.K. Robinson, J.P. Zhang, K.J. Reeson, C.D. Marsh, and G.R. Booker, "SIMS, RBS, ion channelling, and TEM studies of the low energy SIMOX structures," *Nucl. Instrum. Methods Phys. Res., Sect. B*, pp. 750-755, 1992.

[67] R.B. Laughlin, "Optical absorption edge of SiO_2," *Phys. Rev. B*, vol. 22, no. 6, pp. 3021-3029, 1980.

[68] J. Sacks, R.M. Savidge, A. Gabr, A. Walker, R. Beal, J. Wheeldon, A.P. Knights, P. Mascher, K. Hinzer, and R.N. Kleiman, "Quantum Efficiency Measurements of Down-Shifting Using Silicon Nanocrystals for Photovoltaic Applications," in *Photovoltaic Specialists Conference*, Austin, 2012.

[69] T. Trupke, M. A. Green, and P. Wurfel, "Improving solar cell efficiencies by down-conversion of high-energy photons," *J. Appl. Phys.*, vol. 92, no. 3, p. 1668, 2002.

[70] C. Garcia, B. Garrido, P. Pellegrino, R. Ferre, J.A. Moreno, and J.R. Morante, "Size dependence of lifetime and absorption cross section of Si nanocrystals embedded in SiO2," *Appl. Phys. Lett.*, vol. 82, no. 10, pp. 1595-1597, 2003.

[71] H. Jayatilleka, D. Diamare, M. Wojdak, A.J. Kenyon, C.R. Mokry, P.J. Simpson, A.P. Knights, I. Crowe, and M.P. Halsall, "Probing energy transfer in an ensemble of silicon nanocrystals," *J. Appl. Phys.*, vol. 110, no. 033522, 2011.

[72] M. Miritello, R. Lo Savio, F. Iacona, G. Franzò, A. Irrera, A.M. Piro, C. Bongiorno, and F. Priolo, "Efficient Luminescence and Energy Transfer in Erbium Silicate Thin Films," *Adv. Mater.*, vol. 19, pp. 1582–1588, 2007.

[73] J.W.H. van Krevel, H.T. Hintzen, R. Metselaar, and A. Meijerink, "Long wavelength Ce^{3+} emission in Y-Si-0-N materials," *J. Alloys Compd.*, vol. 268, pp. 272-277, 1998.

[74] J. Li, O.H.Y. Zalloum, T. Roschuk, C.L. Heng, J. Wojcik, and P. Mascher, "Light Emission from Rare-Earth Doped Silicon Nanostructures," *Adv. Opt. Technol.*, no. 295601, 2008.

[75] M. Mayer, "SIMNRA User's Guide," Max-Planck-Institut fur Plasmaphysik, Garching, 2002.

[76] E. Klampaftis, D. Ross, K.R. McIntosh, and B.S. Richards, "Enhancing the performance of solar cells via luminescent down-shifting of the incident spectrum: A review," *Sol. Energy Mater. Sol. Cells*, vol. 93, pp. 1182–1194, 2009.

[77] D. Alonso-Álvarez, D. Ross, K.R. McIntosh, and B.S. Richards, "Performance of luminescence down shifting for CdTe solar cells as a function of the incident solar spectrum," in *Photovoltaic Specialist Conference*, Austin, 2012.

[78] D. Li, Y.-B. Chen, Y. Ren, Y.-Y. Zhau, and M. Lu, "A multilayered approach of Si/SiO to promote carrier transport in electroluminescence of Si nanocrystals," *Nanoscale Res. Lett.*, vol. 7, no. 200, 2012.

[79] N. Cheung. (2011, June) Thermal Oxidation of Silicon. [Online]. http://www.eng.tau.ac.il/~yosish/courses/vlsi1/I-4-1-Oxidation.pdf